NASA/TM–2010–215856

Advances in Measuring the Apparent Optical Properties (AOPs) of Optically Complex Waters

John H. Morrow, Stanford B. Hooker, Charles R. Booth, Germar Bernhard, Randall N. Lind, and James W. Brown

December 2010

The NASA STI Program Office … in Profile

Since its founding, NASA has been dedicated to the advancement of aeronautics and space science. The NASA Scientific and Technical Information (STI) Program Office plays a key part in helping NASA maintain this important role.

The NASA STI Program Office is operated by Langley Research Center, the lead center for NASA's scientific and technical information. The NASA STI Program Office provides access to the NASA STI Database, the largest collection of aeronautical and space science STI in the world. The Program Office is also NASA's institutional mechanism for disseminating the results of its research and development activities. These results are published by NASA in the NASA STI Report Series, which includes the following report types:

- TECHNICAL PUBLICATION. Reports of completed research or a major significant phase of research that present the results of NASA programs and include extensive data or theoretical analysis. Includes compilations of significant scientific and technical data and information deemed to be of continuing reference value. NASA's counterpart of peer-reviewed formal professional papers but has less stringent limitations on manuscript length and extent of graphic presentations.
- TECHNICAL MEMORANDUM. Scientific and technical findings that are preliminary or of specialized interest, e.g., quick release reports, working papers, and bibliographies that contain minimal annotation. Does not contain extensive analysis.
- CONTRACTOR REPORT. Scientific and technical findings by NASA-sponsored contractors and grantees.
- CONFERENCE PUBLICATION. Collected papers from scientific and technical conferences, symposia, seminars, or other meetings sponsored or cosponsored by NASA.
- SPECIAL PUBLICATION. Scientific, technical, or historical information from NASA programs, projects, and mission, often concerned with subjects having substantial public interest.
- TECHNICAL TRANSLATION. English-language translations of foreign scientific and technical material pertinent to NASA's mission.

Specialized services that complement the STI Program Office's diverse offerings include creating custom thesauri, building customized databases, organizing and publishing research results . . . even providing videos.

For more information about the NASA STI Program Office, see the following:

- Access the NASA STI Program Home Page at http://www.sti.nasa.gov/STI-homepage.html
- E-mail your question via the Internet to help@sti.nasa.gov
- Fax your question to the NASA Access Help Desk at (443) 757-5803
- Telephone the NASA Access Help Desk at (443) 757-5802
- Write to:
  NASA Access Help Desk
  NASA Center for AeroSpace Information
  7115 Standard Drive
  Hanover, MD 21076

NASA/TM–2010–215856

Advances in Measuring the Apparent Optical Properties (AOPs) of Optically Complex Waters

John H. Morrow
Biospherical Instruments Inc., San Diego, California

Stanford B. Hooker
NASA Goddard Space Flight Center, Greenbelt, Maryland

Charles R. Booth, Germar Bernhard, and Randall N. Lind
Biospherical Instruments Inc., San Diego, California

James W. Brown
CSTARS University of Miami, Miami, Florida

National Aeronautics and
Space Administration

Goddard Space Flight Center
Greenbelt, Maryland 20771

December 2010

Available from:

NASA Center for AeroSpace Information
7115 Standard Drive
Hanover, MD 21076-1320

National Technical Information Service
5285 Port Royal Road
Springfield, VA 22161

Table of Contents

Table of Contents (*cont.*)

J.H. Morrow, S.B. Hooker, C.R. Booth, G. Bernhard, R.N. Lind, and J.W. Brown

ABSTRACT

This report documents the scientific advances associated with new instruments built to measure the apparent optical properties (AOPs) of optically complex waters. The principal objective is to be prepared for the launch of the next-generation ocean color satellites with the most capable commercial off-the-shelf (COTS) instrumentation in the shortest time possible. The first step in the development of the new technology was to enhance a COTS radiometer as the starting point for designing the new sensors and testing the modified sensor(s) in the field. The follow-on steps were to apply the lessons learned towards a new in-water profiler which used a new deployment system or *backplane* for mounting the light sensors (Chap. 2). Following an incremental approach to manage risk, the next level of sophistication involved evaluating new radiometers that were emerging from a separate development activity based on so-called *microradiometers* (Chap. 3). The exploitation of microradiometers for in-water sensors resulted in a state-of-the-art profiling system (Chap. 4), which includes a sensor networking capability to control ancillary sensors like a shadowband or global positioning system (GPS) device (Chap. 5). In terms of next-generation problem sets, one of the principal advantages of microradiometers is their flexibility in producing, interconnecting, and maintaining state-of-the-art instruments for light limited environments (Chap. 6), i.e., shallow and optically complex waters. The full problem set for collecting sea-truth data—whether in coastal waters or the open ocean—involves other aspects of data collection that need to be improved if the uncertainty budget is to be minimized. New capabilities associated with deploying solar references were developed (Chap. 7). Ancillary measurements, particularly observations of the inherent optical properties (IOPs) of seawater are an important part of AOP measurements, but are frequently difficult to make in small boats, because of the current size of IOP instruments. A compact solution for recovering in-water instrument systems from small boats was also developed (Chap. 8).

Prologue

A number of international ocean color sensors have been designed and launched in the last decade and a half to support oceanographic studies and applications including the following: the Ocean Color and Temperature Scanner (OCTS), the Polarization and Directionality of the Earth's Reflectance (POLDER) sensor, the Sea-viewing Wide Field-of-view Sensor (SeaWiFS), two Moderate Resolution Imaging Spectroradiometer (MODIS) instruments launched on the Earth Observing System (EOS) Terra and Aqua satellites (denoted MODIS-T and MODIS-A, respectively), and the Medium Resolution Imaging Spectrometer (MERIS). All of these sensors have contributed significantly to the general problem of inverting optical measurements to derive concentration estimates of biogeochemical parameters, and several continue to provide regular coverage of the global biosphere.

The spaceborne sensors of particular interest here are the SeaWiFS and the two MODIS instruments, and the principal data product of interest is the so-called *water-leaving radiance*, $L_W(\lambda)$, where λ denotes wavelength. For the purposes of ground truth—more correctly *sea-truth*—observations, the $L_W(\lambda)$ values can be derived by extrapolating in-water measurements taken close to the sea surface or obtained directly from above-water measurements. For meaningful applications, an extremely high radiometric accuracy is required. The SeaWiFS Project, for example, established a radiometric accuracy to within 5% absolute and 1% relative, and chlorophyll a (Chl a) concentration† to within 35% over a range of 0.05–50.0 $\mathrm{mg\,m^{-3}}$ (Hooker and Esaias 1993).

The SeaWiFS and MODIS missions are of particular importance here, because their calibration and validation capabilities were developed in parallel and leveraged a number of joint developments which established many of the requirements for ocean color research, e.g., the atmospheric correction scheme. A particularly important joint accomplishment was the establishment of a separate site for vicarious calibration data, which involved a rotating deployment of specially built Marine Optical Buoy (MOBY) units in a clear-water site off the coast of Lanai, Hawaii (Clark et al. 1997).

The worldwide deployments of commercial off-the-shelf (COTS) radiometers have typically been the primary source of validation data for ocean color data products, because they are one of the few mechanisms to sample the dynamic range involved, and have been archived in the SeaWiFS Bio-Optical Archive and Storage System (SeaBASS) for use by the worldwide scientific community. Observations from COTS instruments have also been used for vicarious calibration at a similar level of efficacy to custom hardware like MOBY (Bailey et al. 2008).

---

† In fact, field-to-satellite comparisons (or matchups) are made with respect to the total chlorophyll a (TChl a) concentration, denoted [TChl a].

The ability to use COTS hardware for vicarious calibration was also confirmed by the *Bouée pour l'acquisition de Séries Optiques à Long Terme*† (BOUSSOLE) project in the Ligurian Sea (Antoine et al. 2008). The primary difficulties with buoy solutions for AOP measurements are the wave-induced motions, biofouling of the sensor apertures, and vandalism from commercial and recreational boaters. Both MOBY and BOUSSOLE rely on unique structural choices for wave mitigation (spar and transparent-to-swell designs, respectively), divers to keep the sensor apertures clean, and remote locations to deal with boat traffic.

Despite the potential of increased contamination of the optical data from superstructure perturbations, oceanographic towers offer the unique opportunity of a very stable measurement platform enabling easy and complete control of the deployment geometry (Zibordi et al. 1999). The latter feature permits the deployment of above- and in-water optical instruments with no vertical tilt, and the exact identification of the solar illumination geometry needed for an accurate avoidance or correction of superstructure perturbations (Hooker and Zibordi 2005, and Zibordi et al. 1999, respectively). In-water sensors are easily accessed during periodic (monthly) short maintenance visits to minimize biofouling effects, and above-water sensors experience almost no biofouling, but are also easily serviced.

Ensuring the calibration and validation field data sets are of uniform quality and have an uncertainty less than 5% requires a continuing commitment to quantifying the uncertainties associated with the spaceborne and *in situ* instrumentation. Assuming the uncertainties combine in quadrature, the allowed uncertainty in the remote and *in situ* optical data is approximately 3.5% for each ($\sqrt{5^2/2}$). This means the individual sources of uncertainty for the acquisition of sea-truth data must be on the order of 1–2%, or what is referred to more generally as simply *1% radiometry*.

The uncertainties for the *in situ* part of the total uncertainty budget have a variety of sources:

1. The measurement protocols used in the field,
2. The environmental conditions encountered during data collection,
3. The absolute calibration of the field radiometers,
4. The conversion of the light signals to geophysical units in a data processing scheme, and
5. The stability of the radiometers in the harsh environment they are subjected to during transport and use.

Of these, only items 2 and 5 (above) are outside the control of the individual investigator. The negative aspects of environmental conditions can be largely eliminated by restricting data collection to ideal conditions (clear sky, calm sea, little or no marine haze, and a small solar zenith angle), and the potential for shipping damage can be minimized by using double-packed (box within a box), properly designed, shipping containers.

For the SeaWiFS Project, the first step in the process of controlling uncertainties in field data was establishing—through consensus at a community workshop—and then publishing, the *SeaWiFS Ocean Optics Protocols* (Mueller and Austin 1992), hereafter referred to as the Protocols. The Protocols are considered a *work in progress* and were revised (Mueller and Austin 1995) and significantly expanded (Mueller 2000, 2002, and 2003) by having the scientific community decide which scientific areas would be updated. The Project continuously used the Protocols as the requirements for all sea-truth observations, and although the Protocols were initially established for the SeaWiFS Project alone, all ocean color missions advocate adherence to the Protocols to minimize uncertainties.

The uncertainty in calibrations is the most fundamental, because all the others are only quantifiable if the radiometers are properly calibrated. To maintain internal consistency between calibrations of the *in situ* sensors (and the SeaWiFS instrument itself), the SeaWiFS Project required calibration traceability to the National Institute of Standards and Technology (NIST) and implemented an ongoing series of SeaWiFS Intercalibration Round-Robin Experiments (SIRREXs) to investigate and minimize calibration uncertainties.

In the progression from the first to the third SIRREX (Mueller 1993, Mueller et al. 1994, and Mueller et al. 1996, respectively), uncertainties in the traceability to NIST for intercomparisons of spectral lamp irradiance and sphere radiance improved from 7–8% to 1–2%. The fourth through sixth SIRREX activities further investigated laboratory and field protocols (Johnson et al. 1996, Johnson et al. 1999, and Riley and Bailey 1998, respectively), and showed calibrations at an uncertainty level of approximately 2% were routinely achievable if the Protocols were carefully implemented. This culminated in a detailed experiment to quantify many sources of uncertainties not thoroughly investigated during previous activities at a single calibration facility (Hooker et al. 2002a).

The uncertainties associated with data processing are tied to the Protocols, but there are subjective aspects, like the choice of the in-water extrapolation interval, which are not completely resolved by a single protocol. The first SeaWiFS Data Analysis Round Robin (DARR-94) investigated data processing uncertainties. In addition, it showed differences in commonly used data processing methods for determining primary optical parameters from *in situ* light data, which were about 3–4% of the aggregate mean estimate (Siegel et al. 1995). The focus of the second DARR (DARR-00) was to determine if these results could be improved (Hooker et al. 2001). In terms of overall spectral averages, many of the DARR-00 intercomparisons were to

---

† Literally translated from French as the "buoy for the acquisition of a long-term optical series." "*Boussole*" is the French word for "compass."

within 2.5%, and if the processing options were made as similar as possible, agreement to within less than 1% was possible.

Uncertainties associated with sensor stability have elements both within and beyond the control of an individual researcher. Instrumental drift due to filter deterioration and physical stresses, which can cause shifts in the optical alignment and electrical characteristics of a device, must be tracked even if a concerted effort is made to minimize these problems. The most accessible technology for monitoring the temporal characteristics of instrument response is a portable source (Hooker 2002). All of the devices currently available are derived from the SeaWiFS Quality Monitor (SQM) which was jointly developed by NASA and NIST (Johnson et al. 1998). The SQM is capable of monitoring the stability of light sensors to within 1% in the field (Hooker and Maritorena 2000) and was sufficiently successful to be commercialized by two different companies. More recently, the Portable Universal Radiometer Light Source (PURLS), which is based on tunable, light emitting diodes (LEDs), is being developed by Hydro-Optics, Biology & Instrumentation Laboratories (Bellevue, WA) to replace the SQM.

Prior to the field commissioning of the original SQM, many aspects of sensor performance were maintained by the instrument manufacturer and were not routinely investigated by the individual investigator. The first operational deployment of the SQM demonstrated the importance of independent evaluations of commercial equipment, however, wherein large changes in the responsivity of some of the radiometers—as much as approximately 25% over a one month period—were detected (Hooker and Aiken 1998). More recently, SIRREX-8 showed that the immersion factors supplied by a commercial manufacturer were more than 10% in error at some wavelengths (Zibordi et al. 2002), and there are other examples of the need for independent confirmation of performance specifications in the literature (e.g., Mueller 1995, and Hooker and Maritorena 2000).

The optical parameters do not account for all of the validation requirements for many satellite data products. The determination of chlorophyll *a* concentration, for example, is central to the SeaWiFS Project pigment objective of agreement to within 35%, which is based on inverting the optical measurements to derive pigment concentrations using a bio-optical algorithm. The *in situ* pigment observations will always be one of two axes to derive or validate the pigment relationships, so it seems appropriate to reserve approximately half of the uncertainty budget for the *in situ* pigment measurements. Assuming the sources of uncertainty combine independently (i.e., in quadrature), an upper accuracy range of 20–25% is probably acceptable, although 15% would allow for significant improvement in algorithm refinement (Hooker et al. 2005).

The inquiry into the validation requirements for parameters other than the optical variables began with an intercomparison of four laboratories using different high performance liquid chromatography (HPLC) methods for determining $[\mathrm{TChl}\,a]$ and showed the overall accuracy of the four methods was 7.9% (Hooker et al. 2000a). One method did not separate mono- and divinyl Chl *a*, and if the samples containing significant divinyl Chl *a* concentrations were ignored, the four methods had an average accuracy of 6.7%. More recent results in very different oceanic water types confirm $[\mathrm{TChl}\,a]$ can be estimated with an accuracy to within approximately 7% for a quality-assured laboratory† (Hooker et al. 2005, 2009, and 2010).

Careful implementation of the Protocols can reduce many uncertainties, but it cannot remove them all—many can only be designed out of the instrumentation. To accomplish the latter and to incrementally improve the capabilities of the currently available field equipment, the SeaWiFS Project undertook a long-term development activity for above- and in-water optical sampling systems. Aspects of the design effort were refined based on the lessons learned from the aforementioned round robins associated with understanding the sources of uncertainties in field instruments.

As part of SeaWiFS calibration and validation field campaigns, the SeaWiFS Project combined data acquisition exercises with specific experiments to investigate data acquisition and data processing uncertainties. The experiments were designed to compare a variety of deployment techniques used to measure the *in situ* light field and to incrementally improve the methods and instrumentation employed. Both above- and in-water sensors and methods were evaluated, although the latter predominated. The culmination of the experiments was a demonstration that the *in situ* part of the SeaWiFS uncertainty budget (3.5%) could be satisfied with a dedicated effort of recurring calibrations, stability monitoring, and strict adherence to the Protocols for both the in-water (Hooker and Maritorena 2000) and above-water (Hooker et al. 2004) approach.

Calibration and validation activities require match-up data, that is, contemporaneous observations by the satellite and an *in situ* instrument. Variables that explicitly account for the global solar irradiance, $E_d(0^+,\lambda)$, at the time of data collection—so-called apparent optical properties (AOPs)—are used for match-up analysis, because derivations of $L_W(\lambda)$ in identical waters—but different illumination conditions—will differ. The variability can be removed, in part, by normalizing $L_W(\lambda)$ by the solar irradiance to compute the remote sensing reflectance, $R_{\mathrm{rs}}(\lambda)$. An additional refinement is made by adjusting $R_{\mathrm{rs}}(\lambda)$ by the time dependent mean extraterrestrial solar irradiance to produce the so-called normalized water-leaving radiance (Gordon and Clark 1981), $[L_W(\lambda)]_{\mathrm{N}}$.

---

† A quality-assured laboratory satisfies the so-called *quantitative* level of performance metrics as proposed by Hooker et al. (2005), refined by Hooker et al. (2009), and adopted by the SeaHARRE community.

Accounting for the illumination conditions makes normalized variables the primary input parameters for inverting Chl *a* concentration from *in situ* optical measurements (O'Reilley et al. 1998), which means they are central variables for validation exercises. For vicarious calibration, a final—more exact—computation includes correcting the observations for the angular (bidirectional) dependence of L_W (Mueller and Morel 2003), which are also used for validation and routine data processing.

The central theme in the discussion presented here is the incremental pursuit of more accurate field observations, either in the data collection part of the problem set or in the data processing. The current challenge in ocean color remote sensing is to extend the accomplishments achieved in the open ocean and coastal zone into much shallower waters, e.g., estuaries and rivers. This requirement is driven by the current focus of satellite observations, which are inexorably tied to launching new missions based on novel research topics and assuring the quality of the ensuing satellite data.

The long-term NASA programmatic requirements for ocean color remote sensing are articulated in an Advanced Science Plan, *On the Shores of a Living Ocean: The Unseen World*†. The designated mission themes from this plan, along with the corresponding high-priority research questions, highlight the science and mission concepts the calibration and validation activity must help enable.

The mission themes span a range of scales and applications: a) global separation of pigments and ecosystem components, b) high spatial and temporal resolution of near-shore waters, c) active assessment of plant physiology and composition, and d) determination of mixed layer depths. The corresponding research questions span equally large scales:

- How are oceanic ecosystems and their attendant biodiversity influenced by climate or environmental changes, and how will these evolve over time?
- How do carbon and other elements transition between oceanic pools and pass through the Earth system; and how do biogeochemical fluxes impact the ocean and planetary climate over time?
- How (and why) are the diversity and geographical distribution of coastal marine habitats changing, and what are the implications for human health?
- How do hazards and pollutants impact the hydrography and biology of the coastal zone and human activities, and can the effects be mitigated?

These questions require more interdisciplinary science and a greater amount of observations in the land–sea boundary than any other ocean color mission in the past. More importantly, a higher accuracy in field observations is needed, because the types and diversity of data products will involve significantly more optically complex water masses than usual.

The purpose of this report is to document some of the activities initiated by the OBB Calibration and Validation Office (CVO) to reduce uncertainties in the measurement of AOPs with COTS radiometers—both from a data acquisition and data processing perspective. The principal objective is to be prepared for the launch of the next-generation of ocean color satellites with the most capable COTS instrumentation in the shortest time possible. The latter is required to ensure that the scientists involved can start collecting the baseline observations needed to begin formulating and testing the myriad details associated with hypotheses, algorithms, and databases for the new missions.

To fulfill the need for new sensors, a next-generation capability called Optical Sensors for Planetary Radiant Energy (OSPREy) is being developed (Hooker et al. 2010). The primary objective of the OSPREy activity is to establish an above-water radiometer system, composed of multiple sensors mounted on an offshore-platform, as a lower-cost alternative to existing in-water buoys for the collection of sea-truth observations. The OSPREy sensor suite is being developed by Biospherical Instruments, Inc. (BSI) in partnership with NASA.

The OSPREy concept requires next-generation designs for both above- and in-water AOP sampling systems. The first step in the development of OSPREy was to enhance a COTS radiometer as the starting point for designing the new sensors and testing the modified sensor(s) in the field. The Biospherical Surface Ocean Reflectance System (BioSORS), an above-water radiometric system manufactured by BSI (San Diego, California), was the very first step (Chap. 1). The follow-on steps were to apply the lessons learned from the BioSORS work towards a new in-water profiler called the Submersible Biospherical Optical Profiling System (SuBOPS). SuBOPS combined the incremental changes in radiometry with a new deployment system or *backplane* for mounting the light sensors. The capabilities of the new profiler were intercompared with legacy instruments—the Biospherical Profiler (BioPRO) being the most similar to SuBOPS in terms of spectral and performance capabilities (Chap. 2).

Following an incremental approach to manage risk, the next level of sophistication involved evaluating new radiometers that were emerging from a separate Small Business Innovation Research (SBIR) development activity—based on so-called *microradiometers* (Chap. 3)—to determine if the currently available profiling reflectance radiometer (PRR) series of sensors, or the recently developed microradiometers, should be the foundation for the OSPREy sensor suite. In the end, enhanced microradiometers were selected, because of their unprecedented capabilities across

---

† The Advanced Science Plan, which was drafted by a subset of the science community led by the Ocean Biology and Biogeochemistry (OBB) Program Manager, is available from the following Web site: `http://oceancolor.gsfc.nasa.gov/DOCS`.

a wide dynamic range in measurement requirements. The exploitation of microradiometers for in-water sensors was realized with the state-of-the-art Compact-Optical Profiling System (C-OPS), which was intercompared with the SuBOPS instrumentation (Chap. 4). Part of the attraction of sensor systems built from microradiometers includes their adaptability to sensor networking, for example, controlling ancillary sensors like a shadowband or global positioning system (GPS) device (Chap. 5).

In terms of next-generation problem sets, one of the principal advantages of microradiometers is their flexibility in providing a multitude of system configurations and upgrade paths for shallow and optically complex waters (Chap. 6). The full problem set for collecting sea-truth data—whether in coastal waters or the open ocean—involves other aspects of data collection that need to be improved if the uncertainty budget is to be minimized. New capabilities associated with deploying solar references were developed (Chap. 7). Ancillary measurements, particularly observations of the inherent optical properties (IOPs) of seawater are an important part of AOP measurements, but are frequently difficult to make in small boats, because of the current size of IOP instruments. A compact solution for recovering in-water instrument systems from small boats was also developed (Chap. 8).

A summary of the material presented in each chapter is given below.

1. *The Biospherical Surface Ocean Reflectance System (BioSORS)*

As part of a long-term perspective of supporting both current and next-generation calibration and validation activities for ocean color satellites, incremental modifications to existing COTS sensors were undertaken to reduce the uncertainties in AOP measurements. A principal concern was improving observations made in shallow, optically complex waters, wherein above-water methods have an advantage because they are not subjected to self-shading effects. The primary objective of the BioSORS development was to fit the capabilities of the state-of-the-art COTS PRR series of sensors into a smaller form factor that is more compatible with existing deployment capabilities, and to characterize the new sensors more fully than is the usual practice. The results of these two activities are presented.

2. *The Submersible Biospherical Optical Profiling System (SuBOPS)*

A recurring difficulty with in-water AOP measurements in optically complex waters is adequately resolving the presence of one or more near-surface layers. In some cases, for example close to rivers or sources of melting ice, the layers can have significantly different water properties. The SuBOPS profiler tested the new idea of using a kite-shaped profiler to obtain slower and more stable profiles over traditional rocket-shaped devices, which must fall more rapidly to maintain vertical stability. The performance of the new profiler is presented and includes intercomparisons with legacy instruments, in particular the BioPRO system, which was the most similar to SuBOPS in terms of spectral and performance capabilities. The results show the much slower descent speed and higher data rate for SuBOPS yields a vertical sampling resolution of less than 1 cm in near-surface waters.

3. *Development of the Microradiometer*

A microradiometer consists of a photodetector, preamplifier with controllable gain, high resolution (24 bit) analog-to-digital converter (ADC), microprocessor, and an addressable digital port. In other words, it is a fully functional networkable sensor, all of which resides on one small, thin, circuit-board assembly that is sleeved inside a metal cylinder. With the addition of the front-end optics (collector, window, and filter stack), the basic form factor resembles a shortened pencil. The microradiometer design was developed in response to a need for smaller, faster, and potentially less expensive radiometers, which could be easily scaled to either more or fewer channels and more easily deployed in coastal waters. Because each microradiometer channel has an individual ADC, no multiplexer is required, and no cabling is needed, thereby eliminating a source of electronic leakage and improving reliability. The metal cylinder provides additional isolation from electromagnetic interference sources (e.g., radio frequencies). The photodiode current is converted to voltage with an electrometer amplifier with originally two, but subsequently three gain settings, and the resulting voltage is directly fed to the ADC. The entire assembly, including the photodetector, is located on a single circuit board measuring $0.35 \times 3.0\,\mathrm{in}^2$. Each microradiometer is also equipped with a temperature sensor located close to the photodetector. Clusters of microradiometers can be matched with front-end optics to form small, fast, less expensive, multiwavelength radiometers for a variety of measurements. Each cluster is managed by an aggregator that allows the array of individual radiometers, plus any ancillary sensors, to function as a solitary device.

4. *The Compact-Optical Profiling System (C-OPS)*

The C-OPS instrument successfully integrates a number of new technologies, each focused on different aspects of the practical problem of resolving the optical complexity of the near-shore water column. Although C-OPS represents a significant improvement over BioPRO and other legacy profilers, C-OPS was designed from inception specifically to operate in shallow coastal waters and from a wide variety of deployment platforms. In terms of the mechanics of operating the instrumentation and its behavior during descent, the most significant improvement was to change the basic design for mounting the light sensors from a rocket-shaped deployment system, used in legacy profilers, to the kite-shaped backplane developed for SuBOPS

(Chap. 2). This change allowed the flotation to be distributed as a primary hydrobaric buoyancy chamber along the top of the profiler, plus an adjustable secondary set of one or more movable floats immediately below. The primary set provides the upward buoyant thrust to keep the profiler vertically oriented. The secondary set, coupled with an adjustment mechanism perpendicular to the flotation adjustment axis is used to ensure the two light sensors are level. The hydrobaric buoyancy chamber can contain one to three air-filled bladders, which compress slowly and allow the profiler to loiter close to the sea surface, thereby significantly improving the vertical sampling resolution in near-surface waters. Electronically, the system is self-organizing; when initially powered, the aggregator queries each sensor to determine optimal power required for operation over the existing length of the cables and the population of detectors available to the configuration. Typically, each sensor geometry (E_d, E_u, and L_u) is composed of 19 microradiometer detectors, clustered using the MMS hierarchical architecture coordinated through a master aggregator (Chap. 3). Although the use of microradiometers provides improvements in a variety of operational specifications compared to SuBOPS (e.g., reduced electronic noise and slightly faster data acquisition rates), most notable is the reduction in instrument diameter: C-OPS light sensors use a 2.75 in (7 cm) outside diameter housing, which is 27% smaller in diameter than SuBOPS.

5. *Biospherical Shadowband Accessory for Diffuse Irradiance (BioSHADE)*

BioSHADE is an accessory for shipboard radiometers that is used to measure the optical properties of the atmosphere while providing the usual global irradiance measurement of a solar reference. It meets the need for improving the self-shading correction applied to in-water AOP measurements, wherein atmospheric complexity makes it more difficult to properly model the diffuse irradiance. It also provides for the capability of several atmospheric data products that are useful to the atmospheric correction part of calibration and validation activities. BioSHADE integrates seamlessly into instrument systems based on the microradiometer architecture, although it can be configured for use with the PRR-800 series of solar references or other irradiance sensors with the same form factor. It is composed of the following components: a) the stepping motor and controller unit housing an Mdrive 17 from IMS Systems, b) a data aggregator derived from the microradiometer product line, c) a power regulation subsystem, d) the housing for the electromechanical components, e) the shadowband subassembly, and f) the radiometer mounting components. The Biospherical GPS (BioGPS) is a 12-satellite GPS receiver designed to be operated simultaneously with radiometric instruments. The system can be fully integrated with instrumentation based on the microradiometer architecture, wherein the GPS is operated over a single cable, linking radiometers, BioGPS, and the BioSHADE accessory. The latter ensures the accessory components and the radiometric sensors can be operated using standard cabling and deck box configurations.

6. *Scalable Hydro-optical Applications for Light-Limited Oceanography (SHALLO)*

Based on microradiometer detectors, a suite of instruments has been produced that are specifically designed to improve near-surface, near-shore, and above-water AOP measurements, particularly in light-limited environments. The hierarchical organization inherent in the use of clusters of microradiometers affords an unprecedented ease in interconnecting, modifying, or upgrading the instruments as scientific objectives or financial resources evolve. Purpose-built instruments have the potential to reduce instrument size, complexity, and costs while retaining the optimal field configuration for optical and ancillary sensors. This philosophy is made more powerful by establishing an outline of modular capabilities and a step-wise upgrade pathway for the instrument classes. Unlike legacy sensors, changing, replacing, or repairing a filter or filter-photodetector combination for a microradiometer sensor does not require disassembly of the entire electro-optics section of the instrument. The modularity of the design means it is not a significantly time-consuming and tedious procedure to upgrade a sensor. In addition, the added risk of unintended damage to associated components is minimized, as is the time required to test the subassemblies and recalibrate the sensor. The purpose of this chapter is to introduce a framework for the evolution and expansion of AOP microradiometer instruments into novel deployment opportunities, particularly in light-limited environments, while providing upgrade scenarios to match evolutions in resource allocations and science objectives.

7. *The Telescoping Mount for Advanced Solar Technologies (T-MAST)*

The solar reference data collected with an *in situ* AOP observation must be at the highest point possible on the measurement platform and free from obstructions and reflection sources. Although this is easy to state, it is not always a straightforward operation to implement. On many research vessels, the highest spaces are usually already occupied with the ship's equipment and such spaces are frequently inaccessible at sea (because of safety concerns). Consequently, AOP observations are frequently made with the solar reference located in a less than ideal location. A quantification of the consequences of improperly siting the solar reference are presented along with field evaluations of a new Telescoping Mount for Advanced Solar Technologies (T-MAST). Field trials show T-MAST is an excellent solution for this problem while providing access to the sensor(s) for cleaning, servicing, and dark current measurements.

8. *The Cable Hauler for Optical In Situ Technologies (C-HOIST)*

Because of their large size and weight, IOP instruments are usually mounted inside a large metallic frame and require significant resources to deploy over the side of a ship, e.g., a hydraulic winch and an A-frame. In comparison, modern free-fall AOP profilers, like C-OPS, are sufficiently small in size and weight to be deployed by hand. For small boat operations, AOP instruments are easily accommodated, but IOP sensors usually are not. Most small boats are equipped with a davit for deploying small packages into the water, which, when combined with a COTS system used by the commercial fishing industry, provides a solution to the IOP instrument frame problem. The capabilities of this new deployment system, called the Cable Hauler for Optical *In Situ* Technologies (C-HOIST), is presented along with results from the field commissioning of the prototype. The significant advantages of C-HOIST are as follows: a) the power head uses 12 VDC power, which is available on most small boats; b) there is no need for hydraulics; c) the payload can be raised or lowered very slowly; and d) it can be used with standard synthetic line of any length—there is no need for an integral drum of cable.

Chapter 1

The Biospherical Surface Ocean Reflectance System (BioSORS)

Stanford B. Hooker
NASA Goddard Space Flight Center
Greenbelt, Maryland

John H. Morrow
Biospherical Instruments, Inc.
San Diego, California

James W. Brown
CSTARS University of Miami
Miami, Florida

Abstract

As part of a long-term perspective of supporting both current and next-generation calibration and validation activities for ocean color satellites, incremental modifications to existing COTS sensors were undertaken to reduce the uncertainties in AOP measurements. A principal concern was improving observations made in shallow, optically complex waters, wherein above-water methods have an advantage because they are not subjected to self-shading effects. The primary objective of the BioSORS development was to fit the capabilities of the state-of-the-art COTS PRR series of sensors into a smaller form factor that is more compatible with existing deployment capabilities, and to characterize the new sensors more fully than is the usual practice. The results of these two activities are presented.

1.1 Introduction

The largely successful application of in-water techniques in Case-1 waters (Hooker and Maritorena 2000) has not been exploited to the same degree with above-water methods (approximately 76% of the SeaBASS data is in-water data), although there are specific examples of accomplished above-water field campaigns (Hooker et al. 2004). The above-water approach for calibration and validation activities remains attractive, however, because a) the data can presumably be collected more rapidly and from a ship underway, and b) the frequently turbid, optically complex (both vertically and horizontally), and strongly absorbing waters in shallow Case-2 (optically complex) environments impose significant limitations on in-water measurements.

From a measurement perspective, the above-water problem is more restrictive, because presently there is no reliable mechanism for floating an above-water system away from a research vessel, which is easily and effectively accomplished for an in-water system. Although Hooker et al. (2003) used an extensible deployment system to permit surface viewing farther away from an offshore platform, almost all above-water measurements are made in close proximity to the sampling platform. Careful attention to the metrology of the required geometry and strict adherence to the protocol being used can virtually eliminate the degradations from platform perturbations (Hooker and Zibordi 2005).

The above-water technique described here is an extension of the so-called Modified Fresnel Reflectance Glint Correction method in the Protocols (Mueller and Austin 1995) and includes a more accurate representation of the sea surface reflectance and bidirectional effects (Hooker et al. 2004) and is called the Q02 method. The Q02 approach is based on three measurements: the spectral global irradiance from the sky and Sun, $E_d(0^+,\lambda)$; the spectral indirect (or sky) radiance reaching the sea surface, $L_i(0^+,\lambda)$; and the (total) radiance above the sea surface, $L_T(0^+,\lambda)$. The latter is composed of the radiance leaving the sea surface from below (L_W), the direct sunlight reflecting off the surface (the sun glint), and the indirect skylight reflecting off the surface (the sky glint).

1.1.1 Legacy Instruments

One of the significant differences between above- and in-water methods is the need for maintaining the metrology with the former, that is, the pointing angles associated with the solar geometry must be accurately determined and periodically adjusted. This requirement was the primary motivation for the development of the SeaWiFS Surface Acquisition System (SeaSAS). The SeaSAS frame was a unique device consisting of a pedestal and two rails with sensor mounting plates (Fig. 1) connected to a gear box. When not in use, the two rails can be locked together in the horizontal position, which prevents large accelerations during adverse environmental conditions. The gear box enabled the two rails to move in a scissor-like fashion (i.e., when the sea-viewing sensor was moved upwards, the sky-viewing sensor moved downwards the same amount). The entire assembly could be rotated (and locked) in the horizontal (azimuthal) plane, and a graduated band permitted positioning to within 0.5°. An external module, especially designed for the SeaSAS instrument, measured the vertical (two-axis) tilt and horizontal (compass) pointing of the radiometers, so the stability of the pointing angles could be monitored during data acquisition (Hooker et al. 1999).

Fig. 1. The SeaSAS frame with the rails oriented at approximately 40° with respect to nadir and zenith. The pointing module is attached to the upper right rail (vertically orientated).

The SeaSAS frame was very large, because the radiometers were large, and could not be mounted on lightweight superstructures or used very easily on small boats. The follow-on revisions maintained the accuracy and flexibility in pointing of the original, but were successively smaller. The first of these was the SeaWiFS Underway Surface Acquisition System (SUnSAS), which was used on both small and large boats (Hooker and Lazin 2000). SUnSAS (Fig. 2) made the same measurements as SeaSAS and had an azimuthal band that permitted pointing accuracy to within 1°. The surface-viewing radiometer viewed the sea surface through a square aperture that could be blocked with a calibrated plaque, so it could also measure the radiance of the plaque, $L_p(0^+,\lambda)$. The plaque option was a a required part of one of the above-water methods (Carder and Steward 1985) in the Protocols, but it had to be gray to prevent saturation of the seven-channel sensors used at the time.

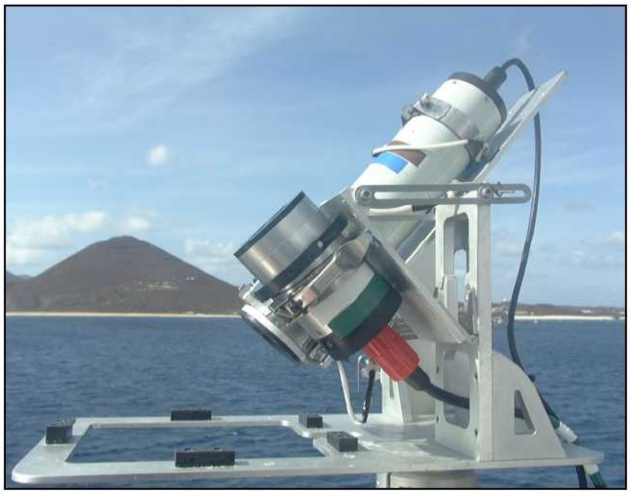

Fig. 2. The SUnSAS frame on the bow of a ship. The long white cylinder is the data logger, which is integral with the L_T (and L_p) sensor, and the L_i sensor is the smaller silver sensor in the foreground. Both devices are attached to hinged plates that can be secured at the desired viewing angle.

The micro Surface Acquisition System (microSAS) deployment frame was based on the SUnSAS design (Hooker et al. 2000b). The primary differences were a result of trying to make the entire instrument package more than an order of magnitude smaller, so it could be fitted inside a cardanic gimble (thereby minimizing the negative effects of ship motion during sampling). The mechanical frame was a compact instrument mounting system wherein the light sensors were clamped to two small plates, which could be tilted to the desired nadir and zenith angles. A vertical tilting and horizontal heading sensor package was fitted inside the gimble ballast, and an azimuthal indexing system with a vernier scale and locking collar permitted accurate horizontal pointing (to within 0.5°).

All SAS deployments required manual pointing of the instrumentation, which meant the data could not be collected autonomously. The SeaWiFS Photometer Revision for Incident Surface Measurements (SeaPRISM) was based on a commercial, fully automated, eight-channel sun photometer that has been successfully used as part of the

Aerosol Robotic Network (AERONET) with many deployed in remote (island) locations (Holben et al. 1998). The normal robotic system measured the direct sun irradiance plus the sky radiance, and transmitted the data over a satellite link. To make the instrument useful for SeaWiFS calibration and validation activities, a capability was added to measure the radiance leaving the sea surface in wavelengths more suitable for the determination of Chl *a* concentration (Hooker et al. 2000b).

The primary advantages of a SeaPRISM instrument that is mounted on an offshore platform versus an in-water moored system (based, for example, on a buoy), are as follows:

1. Offshore platforms that are capable of accommodating above-water instruments are ubiquitous features of the coastal environment, so there are no extra infrastructure costs (and many offshore structures have power systems already installed);
2. A reduction in the vulnerability of the sensors (the structure, and, thus, the entire sensor system, is not easily harmed by recreational or commercial activities);
3. An increase in the pointing stability of the sensors (the sensors are not subjected to the ocean wave field);
4. An almost complete elimination in the fouling of the optical surfaces (the primary source of fouling is wind-blown particles and rather simple stowing procedures of the radiometers can minimize this problem); and
5. A simplification in maintaining and cleaning the equipment (most offshore structures provide easy access for authorized personnel).

The primary disadvantages of the SeaPRISM concept were as follows:

a. It had a small number of channels (eight), which relied on a filter-wheel design (so the channels were not sampled simultaneously);
b. It used a single sensor (so there was a time delay between measurement targets); and
c. The technology was rather old.

Note that the use of a single sensor is also an advantage, because there are no intercalibration issues to worry about.

1.1.2 Next-Generation Instruments

Despite any detractions, SeaPRISM has proved to be a capable platform for algorithm validation and coastal monitoring work (Zibordi et al. 2004). To exploit the lessons learned from SeaPRISM, a next-generation capability called OSPREy is being developed (Hooker et al. 2010). The primary objective of the OSPREy activity is to establish an above-water radiometer system, composed of multiple sensors mounted on an offshore-platform, as a lower-cost alternative to existing in-water buoys for the collection of sea-truth observations. The use of multiple sensors permits synchronous (simultaneous) and asynchronous measurements when needed, and provides a built-in backup capability (if one sensor fails, the synchronized sampling might be lost, but an asynchronous alternative can still be executed). The extra sensors also permit continuous monitoring of the global irradiance, and the addition of a shadowband attachment permits the derivation of extra atmospheric data products. A conceptual depiction of an OSPREy calibration and validation site is presented in Fig. 3.

Fig. 3. An OSPREy system showing two sensor sets on top of an offshore tower measuring the atmosphere and ocean, an ocean color satellite sampling the on- to off-shore (green to blue) productivity gradient, the Sun and Moon as calibration targets, a communications satellite for data (including meteorological) telemetry, solar panels and a wind generator for power, a shore-based support facility, and a small boat for monthly validation—including next-generation in-water AOP profiles—and maintenance visits.

The goal of the OSPREy project is to collect high-quality data satisfying the accuracy requirements for ocean color vicarious calibration and algorithm validation. This means the measurements will have a documented uncertainty satisfying the established performance metrics for producing climate-quality data records (CDRs). The plan is to enhance COTS radiometers to improve their accuracy and extend their spectral range into shorter and longer wavelengths. Greater spectral diversity in the ultraviolet (UV) will be exploited to separate the living and nonliving components of marine ecosystems; UV bands will also be used to flag and improve atmospheric correction algorithms in the presence of absorbing aerosols. The shortwave infrared (SWIR) is expected to improve atmospheric correction, because the ocean is radiometrically *blacker* at these wavelengths.

The OSPREy concept requires next-generation designs for both above- and in-water AOP sampling. The first step in the development of OSPREy was to enhance a COTS radiometer as the starting point for designing the new sensors and testing the modified sensor(s) in the field. The philosophy behind the development plan was to make a series of incremental advances and apply the lessons learned from the prior step to the next one. Within this architecture of managed risk, BioSORS was the very first step.

1.2 The PRR-800 Sensors

The distinguishing features of BioSORS sensors are as follows: a) very high spectral coverage (19 wavelengths with 10 nm bandwidths); b) high-speed, low-noise, three-stage amplification and 16-bit digitization circuitry with each detector individually amplified by an electrometer-grade field-effect transistor (FET) operational amplifier with variable gain (10^5, 3×10^7, and $10^{10}\,\mathrm{V\,A^{-1}}$) that covers more than nine decades of light levels with minimum detectable signals of less than 10 fA and 1.3 µV for the least significant bit; c) very wide dynamic range (the system does not saturate at natural light levels even when the radiance aperture is pointed directly at the solar disk); d) narrow radiance half-angle field of view (FOV) of 3.25°; and e) an irradiance cosine departure of less than 2% from 0–65° and less than 10% from 65–85°.

1.3 PRR-800 Enhancements

The aforementioned PRR-800 specifications are accurately known because the development of the PRR-800 series of sensors included a more extensive amount of instrument characterization than is usually adopted in commercial instrument manufacturing. Specific examples of this extra effort include a) spectral response function determination, b) center wavelength determination and bandwidth of an individual photodetector as assembled in the instrument to an accuracy of 0.1 nm, and c) out-of band blocking at greater than six decades. Additional details concerning the enhancements performed for the BioSORS instrumentation is described in the following sections.

1.3.1 Spectral Response

Characterization of the spectral response function for BioSORS was accomplished using a high-resolution, variable wavelength source based on a monochromator. The unit was designed and built at BSI. The lamp unit is modular and flexible, with multiple sources that are easily selected. The primary source is a xenon lamp, but a mercury arc lamp is used to quickly verify the wavelength scale. To achieve the highest spectral purity, the system uses a quartz prism monochromator as a predisperser feeding a grating double monochromator. These monochromators feature 0.5 m focal lengths and a stacked over-under design with zero tracking error. Relatively wide working slit widths (3 mm) produce 1.3 nm half bandwidth because of the low-aberration, coma-canceling design, and the use of 2,400 grooves per millimeter gratings.

During operation, the instrument is mounted to the output of the spectral tester, and the illumination wavelength is computer controlled (Fig. 4). The advantage to this system is that the spectral response of the assembled and unmodified instrument can be measured directly over many orders of magnitude, rather than having to measure the spectral characteristics of the parts and convolve a spectral response from the components. The relative response of each detector, set between 0–100% of the signal levels recorded during the spectral response, is used to determine the full-width at half-maximum (FWHM) bandwidth, which is 10±1 nm for BioSORS sensors.

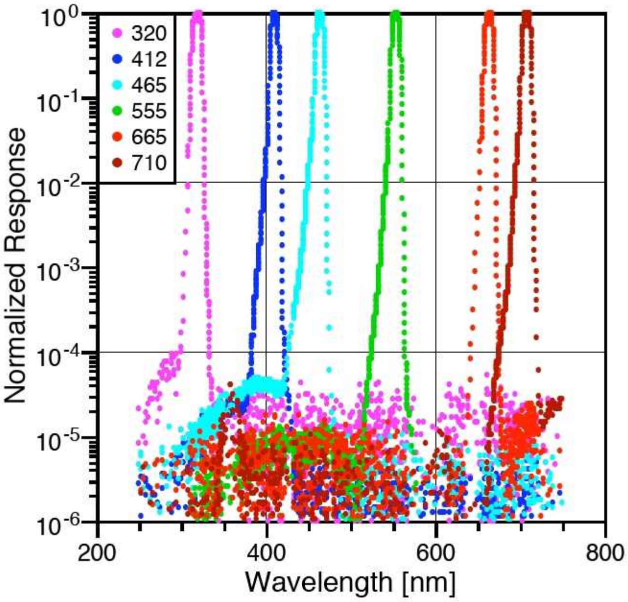

Fig. 4. A semi-log plot of a subset of wavelengths (in nanometers) for the results of the spectral test of the BioSORS irradiance sensor. Features three decades below the peak do not contribute significantly to the measurement.

1.3.2 Linearity

The linearity of each BioSORS radiometer was tested by mounting it to a moveable carriage on a 3 m optical rail, and repeatedly changing the distance between the instrument and a 1,000 W FEL lamp. With this approach, departures from linearity of down to 0.1% over four decades of response can be detected. For reference, nonlinearities in any channel in a BioSORS sensor exceeding 0.5% would be reason to open the instrument and look for a problem (perhaps caused by a bad resistor or a gain change issue).

1.3.3 Cosine Collector

The directional response of the irradiance collector on BioSORS was extensively characterized by mounting it on a directional test apparatus. The apparatus consists of an automated microstepping rotary stage and a 1,000 W FEL lamp mounted to an optical bench. In operation, the instrument is mounted such that the cosine collector is positioned at the axis of rotation. Using the FEL as a source at 165 cm, the directional response is collected from $-110°$ to $+110°$. Typically, the BioSORS irradiance collector agrees with the cosine law to within 2% from 0–65° and to within 10% from 65–85°, with an undetectable azimuthal variation. For reference, the integrated directional response error in measured irradiance of a uniformly diffuse light field is less than 1.5% (worst case).

1.3.4 Stray Light

Stray light consists of extraneous photons that are included in the measurement, but are actually outside the desired FOV. FOV is difficult to measure directly, and it is often specified using a center-point, ray-trace design scheme rather than as a measurement. The impact of FOV and stray light are tightly linked and it is as important to understand the FOV of the instrument as it is to understand the sources of stray light.

The wide dynamic range of BioSORS means that a radiance sensor can be mounted on the directional test apparatus used for cosine characterization without having to adjust for saturation by the 1,000 W FEL lamp. Using the directional test apparatus, the measured full-angle FOV (FAFOV) of the BioSORS design averaged 6.5°. Stray light would appear as shoulders or other features outside the FAFOV (there are no obvious sources of stray light in the final BioSORS design (Fig. 5).

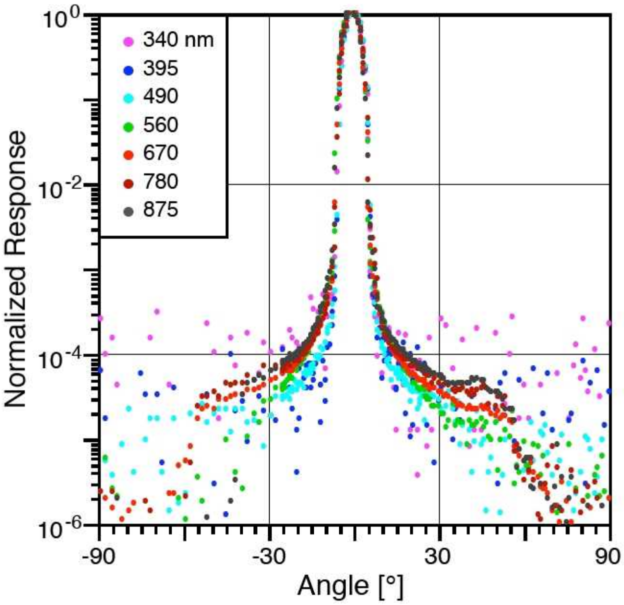

Fig. 5. A semi-log plot of a subset of wavelengths for the directional response of a BioSORS radiance sensor after final stray light and FOV revision.

As an additional test for nonspecific stray light, BioSORS was tested using two scenarios on the BSI radiance calibration apparatus: a) three different instrument-to-plaque distances of 26 (deemed to be ideal), 33.5, and 44.6 cm; and b) two lamp-to-plaque distances of 295 and 195 cm. As a test of stray light, at shorter distances, more of the plaque surface is available to contribute photons from outside the FAFOV. In the absence of stray light, as the instrument is moved closer to the plaque, the radiance is expected to not change until the FOV of the sensor includes the shadow cast by the instrument itself. In all cases, the instrument was positioned at 45° relative to the plaque. At all instrument-to-plaque and lamp-to-plaque distances, the instrument was rotated, which has the effect of changing the area of the plaque that is viewed as the channels move to the edge of the housing. With the exception of the UV channels (because of the low signal), all measurements were within 1% of the mean.

1.4 BioSORS

A preliminary testing of all the modifications detailed in Sect. 1.3 was conducted on the rooftop of the BSI building in San Diego, California. The radiometers were configured exactly as they were to be used in the field, except they were pointed only at the sky. The data collected during an approximately 24 h time period confirms the very wide dynamic range of the PRR-800 technology (Fig. 6), most notably because the data do not saturate even when the sensor is pointed at the solar disk (top), which for the relatively wide FOV of the sensor includes sky radiance contributions.

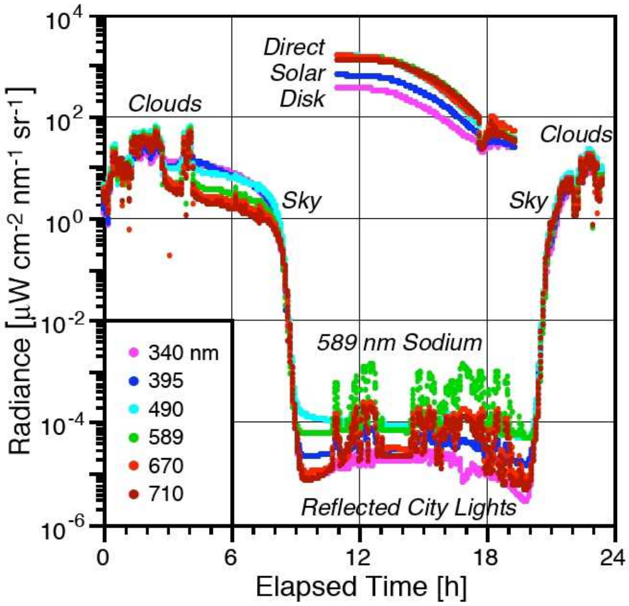

Fig. 6. A time series of zenith sky radiance over an approximately 24 h time period starting in mid-day. Also shown (top) are direct solar disk measurements taken in the middle of the following day.

The sky radiance data in Fig. 6 show the effect associated with clouds passing within the FOV of the sensor, both during Sun and sky measurements. The data also show an interesting subtlety associated with cloud-reflected city lights at night, which are seen as bright reflections in the data plus the presence of a 589 nm sodium line associated with sodium-vapor street lights.

1.5 Data Processing

Regardless of preconceptions, there are no *a priori* reasons to select water-leaving radiances from an above-water method, $\hat{L}_W(\lambda)$, over an in-water method, $\tilde{L}_W(\lambda)$, when sampling in the open ocean (which usually has a deep, optically simplistic mixed layer). There are, however, differences between the two approaches that are relevant to the problem of sampling in the coastal environment. In particular, one of the acknowledged—but largely unproven—advantages of the above-water method is it should be more capable in shallow coastal waters than existing in-water systems. One reason for this perception is all above-water methods are based on pointing a radiance sensor at the sea surface (and at a prescribed nadir angle, ϑ, here 40°), so the total radiance at the sea surface $L_T(\lambda)$, is measured. The acquisition occurs without disturbing the sea surface, so the net effect of the vertical complexity of the water column is precisely captured by the total radiance measurement.

Unwanted radiance contributions must be avoided with both above- and in-water methods. The latter is easily accomplished by floating a free-fall profiler away from the deployment platform. This is not easily done with an above-water method, which must include a prescription for avoiding the glint in the sun plane. This is frequently accomplished by pointing the L_T sensor an angle ϕ' away from the Sun (here either 90° or 135°), while remembering not to point the sensor into any perturbations (shadows or reflections) from the sampling platform.

1.5.1 In-Water Processing

The basic in-water processing follows the well-established methodology of Smith and Baker (1984). In-water radiometric quantities in physical units are denoted $\mathfrak{P}$ and represent the upwelling radiance (L_u) or either the downward or upward irradiance (E_d or E_u, respectively). The in-water values were normalized with respect to $E_d(0^+,\lambda,t)$, with t explicitly expressing the time dependence, according to

$$\mathfrak{P}(z,\lambda,t_0) \;=\; \mathfrak{P}(z,\lambda,t)\,\frac{E_d(0^+,\lambda,t_0)}{E_d(0^+,\lambda,t)} \qquad (1)$$

where $\mathfrak{P}(z,\lambda,t_0)$ identifies the radiometric parameters as they would have been recorded at all depths z at the same time t_0, and t_0 is generally chosen to coincide with the start of the cast. For simplicity the variable t is omitted in the following text.

Subsurface primary quantities $\mathfrak{P}(0^-,\lambda)$ were obtained from the exponent of the intercept given by the least-squares linear regression of $\ln\left[\mathfrak{P}(z,\lambda)\right]$ versus z within an extrapolation interval specified by $z_1 < z_0 < z_2$. The negative value of the slope of the regression fit is the diffuse attenuation coefficient $K_{\mathfrak{P}}(\lambda)$. The K_{L_u} value is used to extrapolate the upwelled radiance through the upper layer to determine $L_u(0^-,\lambda)$ at null depth $z = 0^-$. The water-leaving radiance is obtained using

$$\tilde{L}_W(\lambda) \;=\; 0.54\,L_u(0^-,\lambda), \qquad (2)$$

where the constant 0.54 accurately accounts for the partial reflection and transmission of the upwelled radiance through the sea surface, as confirmed by Mobley (1999). It is important to note the formulation given in (2) assumes there are no artificial perturbations to the $L_u(z,\lambda)$ measurement (a commensurate assumption is made for the above-water approach), and if they are present and unavoidable, corrections to the data are required. Artificial in-water perturbations, for which spectral corrections are routinely applied, is the so-called self-shading effect (Gordon and Ding 1982, and Zibordi and Ferrari 1995).

The appropriateness of the extrapolation interval, i.e., whether or not it satisfied the linear decay of $\ln\left[\mathfrak{P}(z,\lambda)\right]$ in a chosen near-surface layer, was evaluated on a cast-by-cast basis by successive trials using a specific optical quantity (usually L_u or E_d) and a specific wavelength. A direct comparison of the extrapolated $E_d(0^-,\lambda)$ value with the independently measured solar $E_d(0^+,\lambda)$ value—which should closely agree—identified profiles characterized by poor quality (usually because of the presence of large optical stratifications within the extrapolation interval). The use of the red channel ($\lambda = 665$ nm), where seawater is characterized by high absorption and the data show a fast decay to radiometric noise levels as a function of depth, helped in excluding noise from the extrapolation interval.

1.5.2 Above-Water Processing

The aforementioned Q02 method (Sect. 1.1) is used here because for a meaningful comparison with the (nadir-viewing) in-water sensors, the above-water methodology needs to be corrected to account for the bidirectional dependency of the upward radiance field below the surface with that exiting the surface. The basic equations for this transformation (Morel and Gentili 1996, and Mobley 1999) are an established part of the Protocols and have been successfully incorporated into above-water measurements (Hooker and Morel 2003, Hooker et al. 2003, and Hooker et al. 2004), so only only a brief summary is presented here.

The basic difficulty in above-water radiometry is to remove the reflected sky light from the surface measurement, and it is this procedure that distinguishes most above-water methods from one another. For the Q02 method, the sky glint is removed by measuring L_i in the same plane as L_T, and at a zenith angle ϑ' equivalent to ϑ ($\vartheta' = 180 - \vartheta$), as shown in Fig. 7.

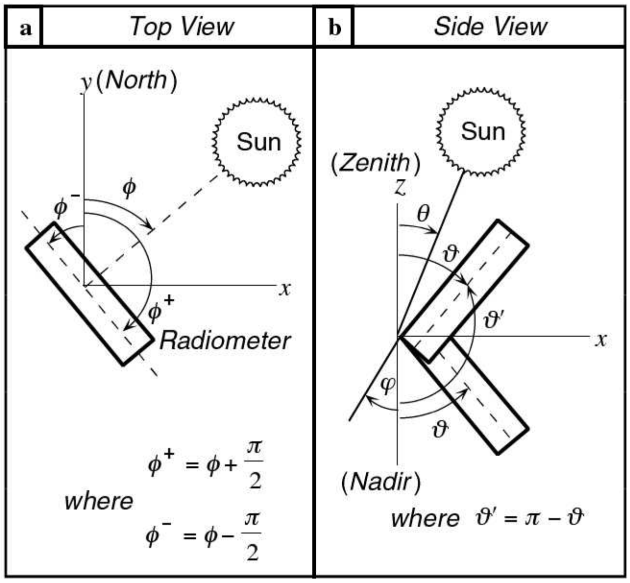

Fig. 7. The coordinate systems used for instrument pointing: **a)** looking down from above (the z-axis is out of the page), and **b)** looking from the side (the y-axis is out of the page). The ϕ coordinate is the solar azimuth angle, θ is the solar zenith angle, and ϑ is the radiometer pointing angle with respect to the vertical axis, z. The perturbations (or tilts) in vertical alignment, which can change the pointing angles, are given by φ.

Note that ϕ is measured with respect to an arbitrary reference, in this case due north, and ϑ is measured with respect to nadir (the direction pointing straight down to the sea surface). The angle ϑ' corresponds to the angle ϑ measured with respect to the zenith (the direction pointing straight up from the sea surface).

The L_i and L_T measurements can then be used to derive the water-leaving radiance (omitting the pointing angles for convenience):

$$\hat{L}_W^{S95}(\lambda) = L_T(\lambda) - \rho L_i(\lambda), \qquad (3)$$

where the S95 notation acknowledges the principal source of the formulation, the SeaWiFS 1995 revision of the Protocols (Mueller and Austin 1995), and ρ is the surface reflectance factor. If the interface was level, ρ would be the Fresnel reflectance (and equal to a constant 0.028 for a 40° viewing angle and relative solar azimuth of 90–135°). Generally, the sea surface is wind roughened, so ρ depends on the capillary wave slopes, and, thus, on wind speed (Austin 1974 and Mobley 1999). The wavelength dependence originates from the normal dispersion of the refractive index of water, which is weak and can be neglected. An updated version of the S95 method using a more accurate ρ value derived from the Mobley (1999) results, which include a wind speed (W) dependence, is referred to as the S01 method (Hooker et al. 2003).

The radiance bidirectionality is parameterized by the so-called Q function, which takes a particular value, denoted Q_n, for the nadir-viewing measurements. For above-water measurements, the angular parameters are imposed by the pointing angles of the sensors, as well as the surface effects of reflection and refraction. When dealing exclusively with Case-1 waters, the functional dependence of the variables can be simplified. In particular, it is assumed that the inherent optical properties are universally related to the chlorophyll a concentration (Morel and Prieur 1977), C_a.

Because a nadir-transformed, above-water estimate of L_W is equivalent to the in-water value, a corrected above-water formulation can be produced (Morel and Mueller 2002):

$$\hat{L}_W^{Q02}(\lambda) = \frac{\Re_0}{\Re(\theta', W)} \frac{Q(\lambda, \theta, \phi', \theta', C_a)}{Q_n(\lambda, \theta, C_a)} \hat{L}_W^{S01}(\lambda), \qquad (4)$$

where the Q terms are evaluated at null depth ($z = 0^-$), θ' is the above-water viewing angle (ϑ) refracted by the air–sea interface, and the factor $\Re$ merges all the effects of reflection and refraction (the $\Re_0$ term is evaluated at nadir, i.e., $\theta' = 0$). All the correction terms are computed here from look-up tables (Morel et al. 2002).

1.6 Radiometric Intercomparisons

Within the context of the generalized difference between above- and in-water methods, an above-water acquisition effort—even if platform perturbations are recognized and minimized—is still more likely to contain platform-contaminated acquisition sequences than free-fall profiles from a simultaneous in-water method. There are exceptions to this generality (discussed below), but it remains more true than not, and is one of the reasons why in-water calibration and validation exercises predominate. Using these arguments as an overall rationale for prioritizing the data used in this study, the analytical perspective adopted here is as follows:

1. Use the in-water observations as the reference measurement for evaluation purposes.
2. When matching the above- and in-water results, use nearly simultaneous (within ±5 min) data acquisition sequences to minimize environmental influences.
3. Use radiometers with absolute calibrations from separate calibration facilities (the usual case for most investigators).

Although the discussion contained within the aforementioned rationale readily supports a decision to use the in-water measurements as the analytical reference, another reason for doing so is that the in-water data processor used here was evaluated in a data processor round robin, and its capabilities (or more correctly, uncertainties) are well quantified (Hooker et al. 2001).

The statistical approach used here is associated with providing an evaluation of an above-water method using the simultaneous in-water measurements as reference values. Toward that end, the primary analytical variable is the relative percent difference (RPD), ψ, between the two simultaneous results. The results of interest are the different determinations of water-leaving radiances, so the RPD formulation is given as

$$\psi(\lambda) \;=\; 100\,\frac{Y \;-\; X}{X}, \tag{5}$$

where Y is the observed value and X is the reference value.

For above- and in-water intercomparisons, Y and X in (5) are denoted by $\hat{L}_W$ and $\tilde{L}_W$, respectively. Because there are two sources of above-water data, BioSORS and microSAS, additional distinctions are provided by which of the two instruments is used. In addition, the two above-water instruments can be intercompared, in which case, the results from the established microSAS instruments are used as the reference value (X) in (5).

The field testing of the prototype took place in 2004 during the Biogeochemistry and Optics South Pacific Experiment (BIOSOPE) cruise (Claustre et al. 2008). The BIOSOPE activity emphasized a significant diversity of AOP sampling from different instruments, and permitted comparisons with traditional above- and in-water techniques. The latter provided the opportunity to compare the capabilities of BioSORS against instruments with a well-established performance history. The first data products to be intercompared were obtained from simultaneous samplings of the new system with the older, seven-channel microSAS instrumentation (Fig. 8).

Fig. 8. The BioSORS (left) and microSAS (right) instruments mounted on the bow platform of the research vessel (R/V) *Atalante* during BIOSOPE.

The wavelength configuration for BioSORS during the BIOSOPE field commissioning campaign spanned the ultraviolet and near-infrared domains, but included many of the relevant ocean color remote sensing bands for a variety of satellites: 320, 340, 380, 395, 412, 443, 465, 490, 510, 532, 555, 560, 625, 665, 670, 683, 710, 780, and 875 nm. The microSAS radiometers, in comparison, only contained the bands 412, 443, 490, 510, 555, 560, and 865 nm. The derived $L_W(\lambda)$ values obtained during simultaneous sampling and involving only the common wavelengths (within 1 nm) between BioSORS and microSAS are presented in Fig. 9. The two sensor systems agreed to within 2.9% (on average) for the center wavelengths that were the same.

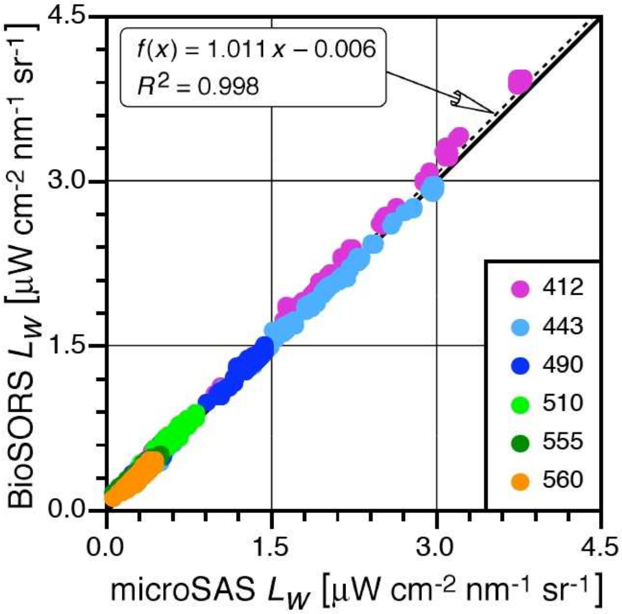

Fig. 9. An intercomparison of microSAS and BioSORS in predominantly oligotrophic (Case-1) waters for six wavelengths given in nanometers. The one-to-one line is shown as solid, and the least-squares linear fit to all the data as dashed (regression information is given in the inset panel).

Comparisons between BioSORS and the in-water AOP profilers were also made, but the number of casts involved are significantly less because the two different types of sampling were frequently far apart in time.

1.7 Summary

Above-water methods for calibration and validation activities are attractive, because turbid, optically complex and strongly absorbing waters in shallow (nominally Case-2) environments impose significant limitations on in-water sensor systems. Above-water instrumentation requirements are well understood and are frequently based on three spectral measurements—the global solar irradiance, the indirect (sky) radiance reaching the sea surface, and the global radiance above the sea surface. The data can be collected rapidly and from a wide variety of platforms, including moving vessels and stationary towers, but careful attention to instrument metrology (viewing angles and measurement geometry) and strict adherence to deployment protocols are required. This requirement was the primary motivation for the development of the early, pedestal-mounted legacy instruments, such as SeaSAS, which emphasized control of the pointing angles and relationship to the Sun that are critical in reducing measurement uncertainties.

All subsequent SAS deployment systems used manual sensor pointing, which meant the data could not be collected autonomously. SeaPRISM was based on an existing commercial, fully automated, eight-channel sun photometer that was successfully used as part of AERONET. In addition to controlling the geometry of the measurements, among the benefits that autonomous operation by SeaPRISM demonstrated was a significant reduction in the fouling of the optical surfaces and the utility of above-water structures as a convenient platform for deployment. The primary disadvantages of the SeaPRISM concept came from the small number of wavebands (eight) and the lack of synchronous sampling inherent with a single sensor and a filter-wheel design.

BioSORS is a modification of existing high-performance radiance and irradiance instruments (PRR-800) originally used for in-water observations to the above-water approach. The distinguishing features of the BioSORS radiometers are a) wide spectral coverage using 19 wavebands (all 10 nm wide); b) high-speed, low-noise, three-stage amplification and 16 bit digitization and three additional stages of variable gain; c) a very wide dynamic range (9 decades), so the system does not saturate at natural light levels even when the radiance aperture is pointed directly at the solar disk; d) a narrow radiance FOV of 3.25° specifically targeting above-water measurements; and e) an excellent irradiance cosine response. In addition to a instrument characterizations in the laboratory for stray light, spectral coverage, and FOV, time series measurements of sky radiance in a large metropolis (San Diego) show subtleties, such as cloud reflections of sodium-vapor street lights.

Field intercomparisons highlighted the significant diversity of AOP approaches from different instruments, and permitted comparisons with traditional above- and in-water techniques. During BIOSOPE, for example, BioSORS was compared with instruments that have well-established performance histories, such as the older, seven-channel microSAS instrumentation. The derived values obtained during simultaneous sampling and involving only the common wavelengths (within 1 nm) between BioSORS and microSAS agreed to within 2.9% (on average) for the matching center wavelengths.

To exploit the lessons learned from SeaPRISM deployments, a next-generation capability called OSPREy is being developed to establish an above-water autonomous system. Composed of multiple sensors mounted on a stable platform, OSPREy is proposed as a lower cost alternative to existing in-water buoys for the collection of sea-truth observations. To minimize risk, the philosophy behind the OSPREy development plan is to make a series of incremental advances and apply the lessons learned from the prior steps to the ensuing one. The first step in the development of OSPREy is to enhance a COTS radiometer as the starting point for designing the new sensors and testing the modified sensor(s) in the field. Within this architecture of managed risk, BioSORS was the very first step. Originally conceived using BioSORS technology, OSPREy will take advantage of even newer high performance AOP instruments developed with NASA funding called microradiometers (Chap. 3).

Chapter 2

The Submersible Biospherical Optical Profiling System (SuBOPS)

Stanford B. Hooker
NASA Goddard Space Flight Center
Greenbelt, Maryland

Randall N. Lind and John H. Morrow
Biospherical Instruments, Inc.
San Diego, California

James W. Brown
CSTARS University of Miami
Miami, Florida

Abstract

A recurring difficulty with in-water AOP measurements in optically complex waters is adequately resolving the presence of one or more near-surface layers. In some cases, for example close to rivers or sources of melting ice, the layers can have significantly different water properties. The SuBOPS profiler tested the new idea of using a kite-shaped profiler to obtain slower and more stable profiles over traditional rocket-shaped devices, which must fall more rapidly to maintain vertical stability. The performance of the new profiler is presented and includes intercomparisons with legacy instruments, in particular the BioPRO system, which was the most similar to SuBOPS in terms of spectral and performance capabilities. The results show the much slower descent speed and higher data rate for SuBOPS yields a vertical sampling resolution of less than 1 cm in near-surface waters.

2.1 Introduction

A number of legacy instruments that were the predecessors of SuBOPS were developed as part of the SeaWiFS Project. The perspective at the time was to produce cheaper—but appropriately accurate—sensors that could be used in open-ocean (optically deep) waters for algorithm validation exercises. The first of these was the Low-Cost NASA Environmental Sampling System (LoCNESS), so named because it was built out of the (relatively inexpensive) modular components typically used with traditional winch and crane deployment systems (Aiken et al. 1998). The LoCNESS profiler was an extremely capable open-ocean unit (Hooker and Maritorena 2000), which included a three-sensor version to measure the upwelled radiance plus upward and downward irradiance as a function of depth, $L_u(z,\lambda)$, $E_u(z,\lambda)$, and $E_d(z,\lambda)$, respectively.

Although used successfully under controlled circumstances in coastal waters at an offshore platform (Zibordi et al. 1999), LoCNESS was difficult to use in small-boat operations or in optically shallow (Case-2) waters, and the light sensors were not mounted on the same horizontal plane—they were separated by the length of the profiler. A smaller version of LoCNESS, called the miniature NASA Environmental Sampling System (miniNESS), was built to determine if light sensors could be mounted on the fins (almost in the same horizontal plane) in a more compact configuration without degrading the quality of the measured signals. Intercomparisons of miniNESS with traditional profilers established the efficacy of the new concept during open-ocean cruises, and then subsequently during coastal campaigns at an offshore tower (Hooker et al. 1999).

The success of miniNESS led to a new design effort called the micro NASA Environmental Sampling System (microNESS) to further decrease the overall size and weight of the profiling package. At the same time, there was a strong desire to replace the analog cabling (associated with traditional profilers) with digital interfaces. The change to digital interfaces was particularly important when combined with the desired size reduction because it helped ensure a) a decrease in power requirements, b) a smaller, lighter profiler with a lower descent speed and, thus, a higher vertical sampling resolution, c) a reduction in the perturbation caused by the instrument to the *in situ* light field, and d) a profiling system that could be easily deployed from a small boat. The latter three are particularly important for coastal, optically shallow (Case-2) applications.

2.2 Design Requirements

Within the context of sampling protocols and data processing, working at the 1% uncertainty level requires the elimination—or at least the significant minimization during sampling or correction during data processing—of any degradation influencing the accuracy of the observations. The perspective here is on coastal sampling, and although the near-shore environment can be optically similar to open-ocean (deep water) conditions, the chance of encountering greater turbidity and optical complexity increases as the water depth decreases. Another unique aspect of shallow water sampling is damage from bottom impacts, or the possible loss of an instrument from entanglement with sea floor debris or structures, is significantly greater.

The principal *theoretical* difficulty of collecting high-quality AOP observations in turbid waters is the degradation of the data from self-shading effects, the severity of which is proportional to the diameter of the light sensors (Gordon and Ding 1992). The need to use small sensors is offset, in part, by the aforementioned desire to have the maximum spectral information possible—whether for satellite match-up analyses or biogeochemical research objectives. Fitting all the needed electronics and optics for a large number of wavelengths in a cost-effective design inevitably increases the diameter of the housing. In the end, a compromise between affordability and size is chosen.

The primary *practical* problem with obtaining good AOP observations in shallow waters is properly resolving the optical complexity of the water column. The near-shore environment often contains multiple layers of distinct water types that are optically different. The presence of one or more optically different near-surface layers can alter the usual log-transformed linear decay of the measured optical properties, and, thus, significantly degrade the accuracy of the (estimated) surface values. In these situations, it is crucial that the vertical sampling of the water column discriminates the layers with enough data points that the data processing scheme can accommodate their influence. When one or more layers are very close to the sea surface, this is a hard requirement to satisfy, because of the turbulence of the air–sea interface (from surface gravity and capillary waves) and the bulkiness of the instruments.

The surface waves add a significant amount of noise to the data from wave-focusing effects, and they can cause excessive tilting of the nadir-viewing sensors, as well as splash effects (e.g., foam and bubble formation). The physical size of the instruments dictate the mounting options—which must permit unobstructed viewing for all the sensors—and this usually prevents all the measurements from being taken in the same horizontal plane. Consequently, there are usually depth offsets between the various sensors, which means some portion of the upper water column is not sampled by all of the sensors. The most extreme offsets occur when sensors are placed on opposite (vertical) ends of the mounting assembly (as is the case with BioPRO).

The hazard associated with the sea floor, either from bottom impacts or debris entanglements, cannot be removed by simply not sampling very close to the bottom. As the water depth decreases to very shallow values (defined here as being less than 10 m), bottom contributions—either from light reflections or the optical influence of distinct turbidity layers—can have an increasingly important effect on near-surface parameters, so this part of the water column needs to be measured.

Regardless of how these myriad problems are addressed, the chosen deployment system must be able to make a vertical profile of the water column that is free of any perturbations from the sampling platform, usually a boat. For coastal campaigns, small vessels are ubiquitous, so there is the added challenge of getting good data from an actively moving platform. Although winch and crane systems can be adapted to small boats, they usually do not have significantly large cranes (as found on deep-ocean research vessels), so it is unlikely an optical package can be deployed an appreciable distance away from the ship.

2.3 The BioPRO System

A reliable procedure for obtaining a vertical profile of light parameters devoid of ship perturbations is to use a free-fall instrument that is floated away from the vessel before measurements are started. This technique has been used extensively in a variety of sensor systems based on a common instrument design developed for open-ocean waters (McClain et al. 2004), i.e., deep water and extensive mixed layers). The light sensors are connected in line with power and telemetry modules to form a long cylinder. A radiance sensor is positioned on the *nose* to measure the upwelled radiance, $L_u(z,\lambda)$, and an irradiance sensor on the *tail* to measure downward irradiance, $E_d(z,\lambda)$. The addition of weight to the nose and buoyant (foam) fins to a tail bracket produces a rocket-shaped package that falls through the water column with minimal tilts (less than 5° over most of the profile).

Adjustments to the amount of weight and fin surface area are used to fine tune the stability of the package during descent, but fundamentally, the most stable configuration occurs at the highest descent velocities. The power and telemetry cable extends through the field of view of the irradiance sensor, but the small diameter of the cable minimizes any negative effects on the measured light field. The addition of a temperature (and, if possible, a conductivity) probe, provides a good description of basic water column properties. To ensure the data are acquired during stable illumination conditions, a separate irradiance sensor is mounted as high on the ship's superstructure as possible (so the data are not degraded by shadows or reflections) to measure the total solar irradiance, $E_d(0^+,\lambda)$.

BioPRO is a 19-channel (λ_{19}) device based on a rocket-shaped design, although the fins are not buoyant. The tail buoyancy comes from a foam collar attached to the main body at the end of the profiler, and the two fins are solid plastic (Fig. 10). The overall length is approximately 59.7 cm, so it is a rather compact design (typical free-fall profilers in use for open-ocean sampling at the time BioPRO was designed were about 1.24–1.78 m in length). Using only the collar weight and adding no additional weights, the descent speed is about $30\,\mathrm{cm\,s^{-1}}$. To achieve greater stability, weight is added resulting in a typical descent speed of $40–60\,\mathrm{cm\,s^{-1}}$.

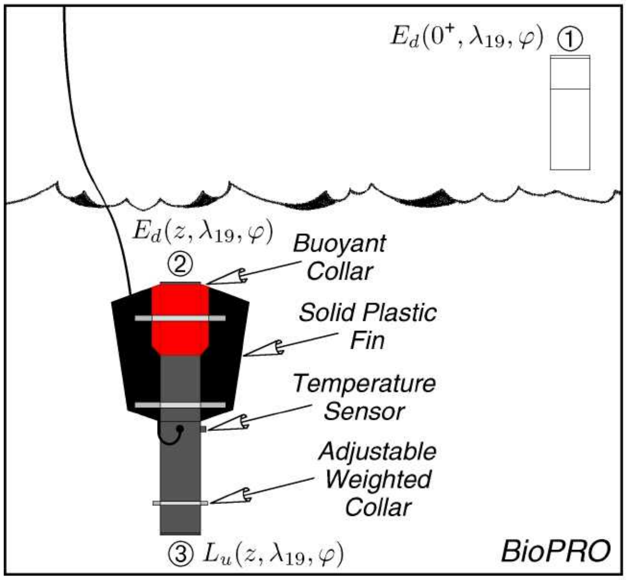

Fig. 10. A schematic of the BioPRO profiling system showing the three types of light measurements involved. The two solid plastic fins provide some protection for the buoyant collar during deployment and recovery. The numeric bullets clarify the number of individual light sensors and are used in all subsequent instrument diagrams. The use of different gray colors are to provide contrast for easier interpretation of the schematic.

One advantage of BioPRO, in terms of sampling capabilities, is it can be deployed easily by only two people, so data collection can commence quickly when light conditions are optimal. BioPRO is most frequently deployed from the stern of the vessel, and whenever possible, the ship maintains a small or impulsive headway speed of approximately 0.5 kts or less (depending on surface currents, winds, and waves). The profiling instrument is carefully lowered into the water and repeatedly dropped and recovered within the near-surface layer until it has drifted clear of any possible perturbation effects from the vessel. When the profiler reaches the desired distance from the stern (usually 30–50 m), it is ready for deployment and can be *dropped* or released.

Once released, the nose weight orients (or *rights*) the profiler into a vertical alignment, and the entire package starts to descend (the first few meters of data frequently have large tilts and are ignored). The greater the nose weight, the shorter the righting time, but there is also an increased chance of large back-and-forth oscillations, because the weighted nose and buoyant fins establish a natural pendulum. The cable is almost neutrally buoyant and has a low coefficient of drag, so the profiler falls freely through the water column. The desired depth is usually the 1% light level, but deeper casts to completely sample some other aspect of the water column are frequently made.

The most important aspect for collecting good data with a free-fall profiler is to prevent the telemetry cable from ever coming under tension, because even brief periods of tension can adversely affect the vertical orientation (two-axis tilt) and descent velocity of the profiler. To ensure this does not occur, the operator leaves a few coils of cable at the surface. A tangle-free and continuous feed of cable into the water is also needed, so all of the cable (approximately 125 m for BioPRO) is laid out or *flaked* on deck prior to each deployment in such a manner as to minimize any entanglements. The profiler descends at approximately $50–60\,\mathrm{cm\,s^{-1}}$ so a coastal ocean cast can be acquired very quickly.

The Recommended Standard 485 (RS-485) signals (or RS-422 for some instruments) from the in-water profiler and the above-water solar reference are combined in a deck box and converted to RS-232 communications for computer logging. The deck box also provides the (computer-controlled) power for all the sensors and was designed to avoid instrument damage due to improper power-up sequences over varying cable lengths. The RS-232 data are logged on a Macintosh laptop using software developed at the University of Miami Rosenstiel School for Marine and Atmospheric Science (RSMAS) in partnership with NASA.

The software time stamps the two data streams (in-water and above-water measurements), which are both acquired at a 12 Hz data sampling rate, and simultaneously writes them to disk. The data is stored as American Standard Code for Information Interchange (ASCII), tab-delimited (spreadsheet) files. The software controls the logging and display of the data streams as a function of the data collection activity being undertaken: dark data (caps on the radiometers), down cast, etc. The selection of the execution mode automatically sets the file name, so all the operator has to do is push buttons to initiate and terminate data acquisition. All of the telemetry channels can be displayed in real time, and the operator can select from a variety of plotting options to visualize the data being collected.

The spectral configuration of AOP profilers are necessarily tied to the remote sensing and scientific research objectives. The former are further divided between verifying the vicarious calibration of the satellite sensor, and validating (or creating) the data products derived from bio-optical algorithms that require a well-defined set of wavelengths; whereas the latter permit a wider diversity of choices, although for many ocean color investigations they are most frequently composed of blue–green band ratios of the remote sensing reflectance (O'Reilly et al. 2000). Whether for ground truth observations, algorithm validation, or the aforementioned *in situ* stability analyses, it is desirable that the center wavelengths and bandwidths for the individual channels agree as closely as possible.

The BioPRO band set is a compromise between research and remote sensing requirements and is composed of the following wavelengths (each is 10 nm wide and the channels that are specifically selected for remote sensing applications are underlined): 320, 340, 380, 395, 412, 443, 465, 490, 510, 532, 555, 560, 625, 665, 670, 683, 710, 780, and 860 nm.

Although the calibration and validation activities for the remote sensing objectives can be restricted primarily to the near-surface layer of the water column, generalized inquiries into the biogeochemical properties of the ocean require water column sampling throughout the euphotic depth (i.e., to as deep as the 1% light level). The optical profiling systems discussed here were all designed to contribute to extensive sampling of the euphotic layer.

2.4 Evaluation of BioPRO

The BioPRO design was evaluated by intercomparing it to microNESS, which was especially designed to have a smaller size and weight—and to a certain extent—a slower descent speed. The microNESS profiler was conceived as a successor system to miniNESS, which was built to determine whether or not light sensors could be mounted on the fins (in very nearly the same horizontal plane) in a more compact configuration without degrading the stability of the rocket-shaped profiler and, thus, the light-field measurements. The compactness was achieved by significantly reducing the overall length of the instrument, which reduced the *righting moment* (the distance from the weighted nose to the buoyant fins). Intercomparisons of miniNESS with traditional profilers established the efficacy of the new concept during open oceanic cruises, and then subsequently during coastal field campaigns (Hooker et al. 1999).

The success of miniNESS led to the microNESS design effort (Fig. 11), the main objective of which was to further decrease the overall size and weight of the profiling package. This was achieved by replacing many metal components with synthetics, switching from a four-fin to a two-fin design, and reducing the size of the electronics and, thus, the diameter of many components. The solar reference has seven channels, so the in-water light sensors have redundant 412 nm channels, which are used for self-shading severity analysis. The emphasis on coastal sampling prescribed a high-precision depth sensor, which is fitted to the *nose* of the instrument. Although capable of slower descent speeds than traditional free-fall profilers, the rocket form factor required relatively high speeds for stability. This, coupled with the relatively slow data rate (6 Hz), meant near-surface effects (e.g., wave focusing) were significantly aliased during vertical profiling.

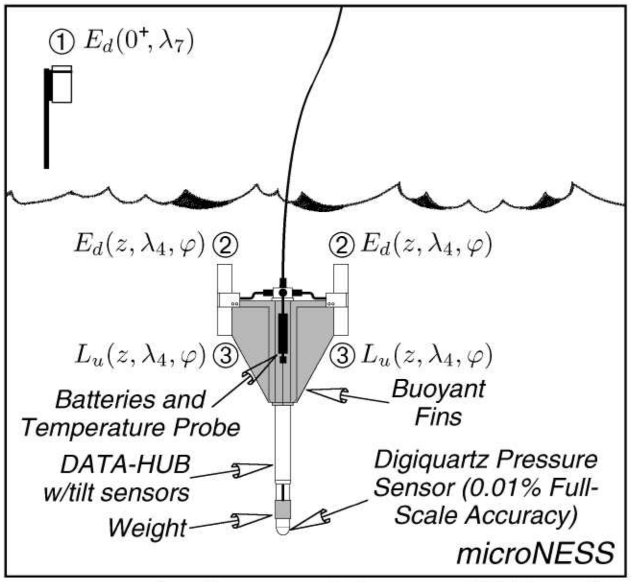

Fig. 11. A schematic of the microNESS profiling system showing the two four-channel, all-in-one light sensors (L_u and E_d are in the same housing) mounted on the edge of the buoyant fins.

Another microNESS design objective was to replace the traditional analog cabling with digital interfaces. This objective was particularly important, because when combined with the desired size reduction, it would help ensure the following: a) lower power requirements and, thus, a battery option; b) a smaller, lighter profiler (a 1.0 m length and an in-air weight of 4 kg); c) a reduction in the light field perturbation caused by the instrument (the main-body diameter was reduced to 4.6 cm); and d) a profiling system easily deployed from a small boat. The microNESS profiler was a capable system (Barlow et al. 2003), although it suffered from elevated uncertainties in the 510 nm channel (as did some other profilers with a similar heritage).

An intercomparison of BioPRO and microNESS based on common wavelengths is presented in Fig. 12. Because the data were not simultaneous, like the BioSORS evaluation (Fig. 9), changes in the solar geometry between the casts are accounted for by using the normalized water-leaving radiance, $[L_W(\lambda)]_{\mathrm{N}}$. Predominantly open-ocean, oligotrophic (Case-1) waters were used to ensure the water types were not a limiting factor in the comparisons—the objective was to discern the performance of the instruments, without having to qualify the results as a function of the water masses. The unbiased percent difference (UPD†) for each channel between the two profilers averages -7.6% to 0.3%, with an overall average of -2.2% (for the Fig. 12 wavelengths), which is to within the calibration uncertainty. The largest difference corresponds to the 510 nm channel, which was a problematic wavelength with

---

† The UPD is defined as $200(Y - X)/(Y + X)$, where X is the reference instrument or data, which in this case is the microNESS profiler.

the class of radiometers used with microNESS (Hooker and Maritorena 2000). A least-squares linear regression of the data (Fig. 12 inset panel) shows almost one-to-one correspondence with over 95% of the variance explained.

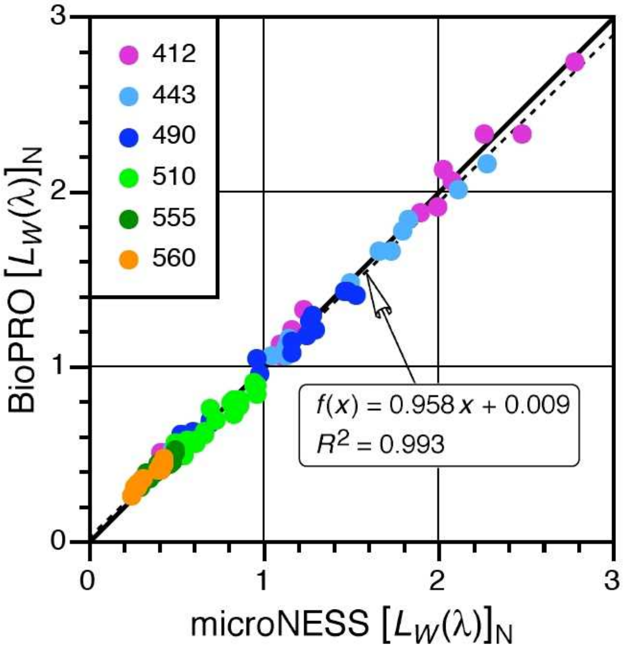

Fig. 12. An intercomparison of microNESS and BioPRO in predominantly oligotrophic (Case-1) waters for six wavelengths given in nanometers. The units for $[L_W(\lambda)]_N$ are μW cm^{-2} nm^{-1} sr^{-1}. The one-to-one line is shown as solid, and the least-squares linear fit to all the data as dashed (regression information is given in the inset panel).

One reason for the good agreement in Fig. 12 is the extrapolation intervals of the two profilers were rather similar. In addition, the vertical resolution (i.e., the number of acceptable data points) in each extrapolation interval was adequate for open-ocean (deep mixed layer) conditions: approximately 4 cm for BioPRO and about 7 cm for microNESS. The reason for the difference between the two profilers is the BioPRO instrument has a higher data rate, so it collected approximately 43% more data on average.

2.5 SuBOPS—A Kite-Shaped Profiler

The SuBOPS free-fall profiler is based on the same radiometers used with BioSORS and BioPRO (i.e., the PRR-800 series of optical sensors packaged into 3.5 in housings). The changes that were made to create the new design were motivated by the desire to collect the best possible data in coastal (Case-2), optically complex waters.

A free-fall design permits the avoidance of ship-induced perturbations, but it does not deal with the problems of self-shading perturbations, optical complexity, near-surface effects, and bottom hazards. The SuBOPS profiler was designed with the goal of minimizing these effects in the most cost-effective manner possible. This was accomplished by using the following design principles:

1. Repackaging the electronics and optics in a smaller 3.5 in (8.9 cm) housing in keeping with in-water designs already successfully used in coastal campaigns (Hooker et al. 1999, Doyle et al. 2003, Hooker et al. 2004, and Hooker and Zibordi 2005);
2. Decreasing the overall length for irradiance (and radiance) from 22.0 in (55.9 cm) to 13 in (33.0 cm) and mounting the light sensors as close as possible to the same horizontal plane;
3. Increasing the stability of the instrument package during descent (minimizing the vertical tilting of the sensors as they fall through the water column) while improving the vertical resolution of the sampling by a) maintaining a higher data sampling rate (12 Hz), and b) reducing the descent speed by switching from a rocket-shaped device (BioPRO and its predecessors) to a kite-shaped design; and
4. Relying on a slow descent speed (about 20 cm s^{-1} or less) and a bottom-pointing spar to minimize damage from accidental bottom impacts.

Note that the reduction in size also reduces the total weight and makes the profiler easier to handle from small boats. A schematic of the SuBOPS profiler is presented in Fig. 13.

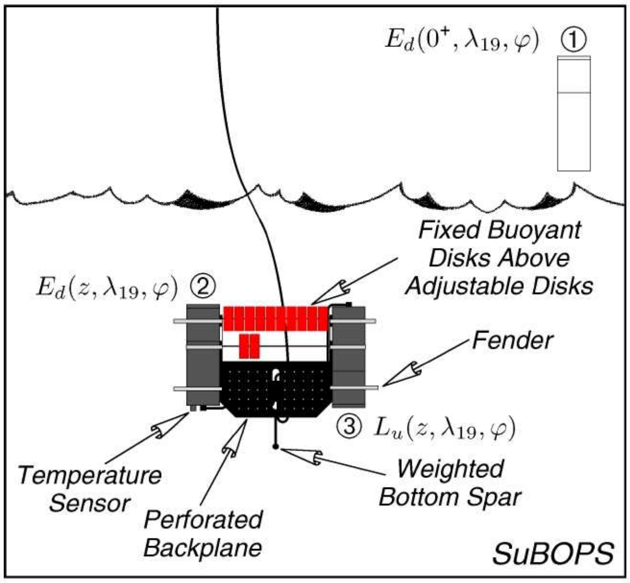

Fig. 13. A schematic of the SuBOPS profiler. Any needed weight is added to a bottom-pointing spar (or *stinger*), which also protects the L_u aperture in the case of an accidental bottom impact.

Of the design changes adopted in creating SuBOPS, the most significant—in terms of the mechanics of operating the instrumentation and its behavior during descent—was to change the basic design for mounting the light sensors from a rocket-shaped deployment system to a kite-shaped backplane. This change allowed the buoyancy to be distributed as a primary set of small disc floats (used in the commercial fishing industry) along the top of the profiler, plus an adjustable secondary set of one or more floats immediately below (Fig. 14). The primary set provides the upward buoyant thrust to keep the profiler vertically oriented, and the secondary set is used to ensure the two light sensors are level (the E_d sensor is slightly bigger and heavier than the L_u sensor, because it contains more electronics and the ancillary tilt and temperature sensors).

Fig. 14. The early SuBOPS prototype in preparation for redeployment in Mission Bay (California) after having the weighted bottom spar adjusted (not blackened for clarity). Note the aluminum fenders protecting the sensors at the bottom of the profiler (not blackened pending final dimensioning).

SuBOPS can be trimmed for very slow descent speeds (less than $15\,\mathrm{cm\,s^{-1}}$). During trials in a swimming pool, the profiler descended so slowly it would come to rest on the cable catenary while being vertically oriented to within 1°. The vertical orientation specification for the new backplane was vertical tilts to within 2.5° for the entire water column (under favorable conditions). Although higher sea states can cause significant tilts during the early descent of the profiler, once these perturbations subside, the rest of the profile typically meets this specification. Note that vertical tilts are not so damaging as long as the profiler is going back and forth through zero, because larger tilts can be filtered out in the data processing scheme.

The light sensors are mounted against a thin perforated plate or backplane. The perforations help reduce the tilting influence of water currents by allowing some of the water to pass through the plate (as well as the open area associated with the disc floats). The distribution of the floats within the interior of the profiler protects them from accidental ship impacts during profiler deployment and recovery. The light sensors are likewise protected by fenders mounted at the top and bottom of each radiometer.

The power-telemetry cable attaches to a Y-cable connected to the two light sensors, and a strain relief on the cable attaches to a four-point cable harness (Fig. 14). When the cable is pulled, the harness extends away from the backplane and the profiler *kites* up to the surface (if submerged), and this direction is in the direction of the pitch axis. The direction perpendicular to the pitch axis is the roll axis. The latter is adjusted by moving the secondary row of floats. A pitch bias is counterbalanced by attaching weight to the appropriate side of the backplane. Additional refinements to the kite-shaped backplane and more deployment detail are provided in the description of the C-OPS instrumentation (Chap. 4).

2.6 SuBOPS Evaluation

The intercomparison results between SuBOPS and BioPRO for eight common wavelengths are shown in Fig. 15 (six of the wavelengths are common to Fig. 12). Predominantly eutrophic (Case-2) waters were used because the focus of SuBOPS was to begin the process of making better AOP observations in coastal waters. The average UPD for each channel between the two profilers ranges from −3.5% to 3.6%, with an overall average of 1.3% (for the wavelengths plotted in Fig. 12), which is to within the calibration uncertainty. A least-squares linear regression of the data (Fig. 15 inset panel) shows an almost one-to-one correspondence with over 95% of the variance explained.

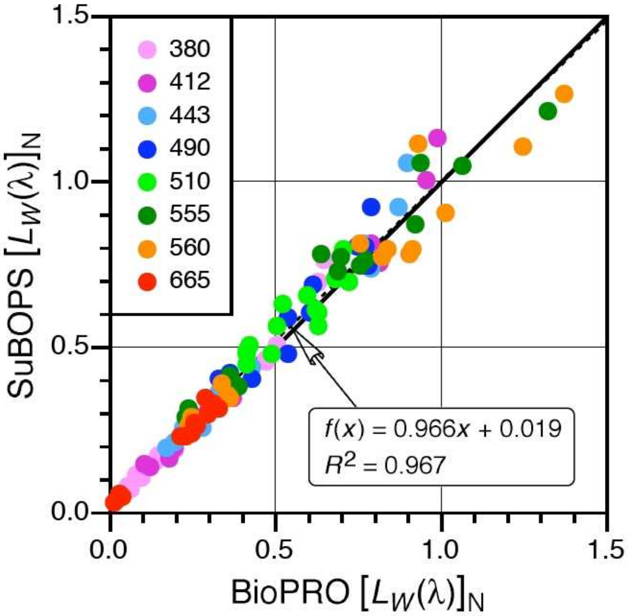

Fig. 15. An intercomparison of BioPRO and SuBOPS in predominantly eutrophic (Case-2) waters for eight wavelengths, given in nanometers. The units for $[L_W(\lambda)]_N$ are $\mu\mathrm{W\,cm^{-2}\,nm^{-1}\,sr^{-1}}$. The one-to-one line is shown as solid, and the least-squares linear fit to all the data as dashed (regression information is given in the inset panel).

Deeper, but nonetheless turbid, waters were used for the intercomparisons presented in Fig. 15, because of the difficulty of avoiding bottom impacts with BioPRO in shallow water. Most casts were executed in calm conditions, to minimize BioPRO near-surface tilting when it was released, thereby minimizing wave-induced tilting. Although these conditions might be considered nearly optimal, they are not as ideal as the open-ocean (deep mixed layer) conditions for the prior BioPRO intercomparison (Fig. 12), so there is greater variance in the distribution of the data.

The most highly attenuated parts of the spectrum were in the UV and near-infrared (NIR) channels for which diffuse attenuation coefficient (K_d) values were 3–4 m^{-1}. These channels are not shown in Fig. 15 and had average UPD values ranging from -7.0% to 27.8%. The large differences are primarily associated with the inability of the BioPRO profiler to collect sufficient data in the near-surface waters to provide good data products for highly attenuated channels. Even though the extrapolation intervals for BioPRO extended approximately 29% more than SuBOPS, the slower descent speed of SuBOPS resulted in about 16% more data in the extrapolation interval. The start of the extrapolation interval was shallower for the SuBOPS data set, which is important for the most highly attenuated channels.

2.7 Design Refinements

After establishing the prototype, the SuBOPS instrumentation was used to test and refine various aspects of the new deployment capability. One of the first aspects to be refined was the flotation, because the original flotation could not be machined or shaped into smaller pieces. Consequently, the smallest integral unit was one flotation disk, which was too coarse an element for quickly fine tuning the descent of the profiler. If only a small amount of flotation was needed, an entire disk needed to be added, which meant that more weight needed to be added to reduce the net buoyancy, and this process required fine tuning with a series of test casts. Although this system worked, it was time consuming and there were water masses for which an ungainly amount of buoyancy and weight was needed to trim the profiler to lower descent speeds.

A new flotation material that could be machined and cut into pieces without compromising its strength was substituted for the original flotation disks. The new material was very strong, which meant that the top-most portion on the profiler could be hollowed out. This allowed an elongated compressible bladder filled with air to be fitted into the cavity, which significantly improved the *loitering time* of the profiler closer to the sea surface by providing a so-called *hydrobaric* buoyancy system. The volume of the bladder is set so the profiler barely sinks. As the depth increases, the bladder is compressed more and more and the descent rate increases, until it reaches terminal velocity.

A design objective of the hydrobaric buoyancy system was to acquire 200 or more samples in the upper 2 m of the water column, i.e., a vertical sampling resolution of at least 1 cm. The prototype system very nearly satisfied this requirement, and the extent of the accomplishment is seen by comparing this new capability to another legacy profiler, the SeaWiFS Profiling Multichannel Radiometer (SPMR). This comparison is made with respect to the SeaWiFS Free-Falling Advanced Light Level Sensors (SeaFALLS) profiler, which was a modified SPMR having slightly larger fins for greater stability and finer trim tuning (Fig. 16).

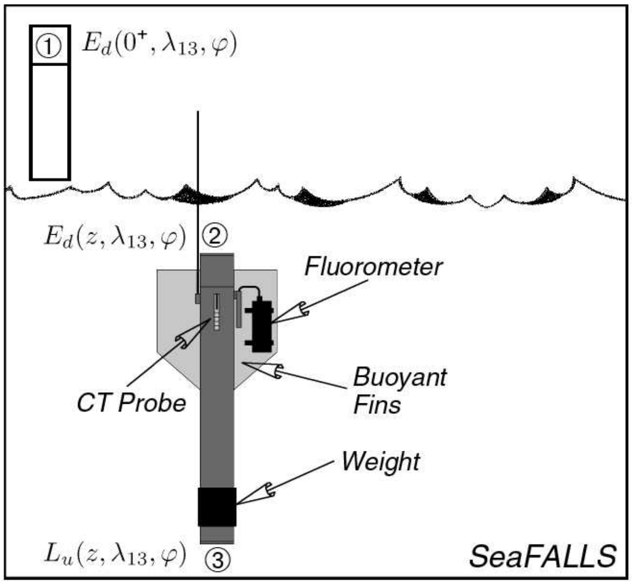

Fig. 16. A schematic of the SeaFALLS profiler. A unique aspect of this instrument was the fluorometer mounted on one of the fins.

As shown in Fig. 17, the new SuBOPS unit fitted with the hydrobaric buoyancy system has a vertical sampling resolution at 2 m of about 90 samples per meter. The total number of samples collected at 5, 10, and 15 m depth is N_5=519, N_{10}=829, and N_{15}=1,138, respectively. In comparison, the rocket-shaped SPMR has a high descent rate, which yields an average sampling resolution of about 6–7 samples per meter, and the total number of samples collected at 5, 10, and 15 m depth is an order of magnitude less than the SuBOPS profiler.

If profiler orientation is used to reject data that exceeds a vertical tilt of 5°, the sampling resolution of the SPMR is further degraded in the near-surface waters, because the profiler has a large *righting moment*. That is, because of its length (about 1.24 m), it takes time (which is to say, depth) for the SPMR to become vertically oriented. SuBOPS, on the other hand, starts out more vertically oriented, and because it initially sinks very slowly, not much depth is lost before it is reliably sinking in a near-vertical orientation.

Because of the shape of the backplane and the four-point harness, when the SuBOPS unit is retrieved from depth, it has a tendency to *kite* up to the surface. That is,

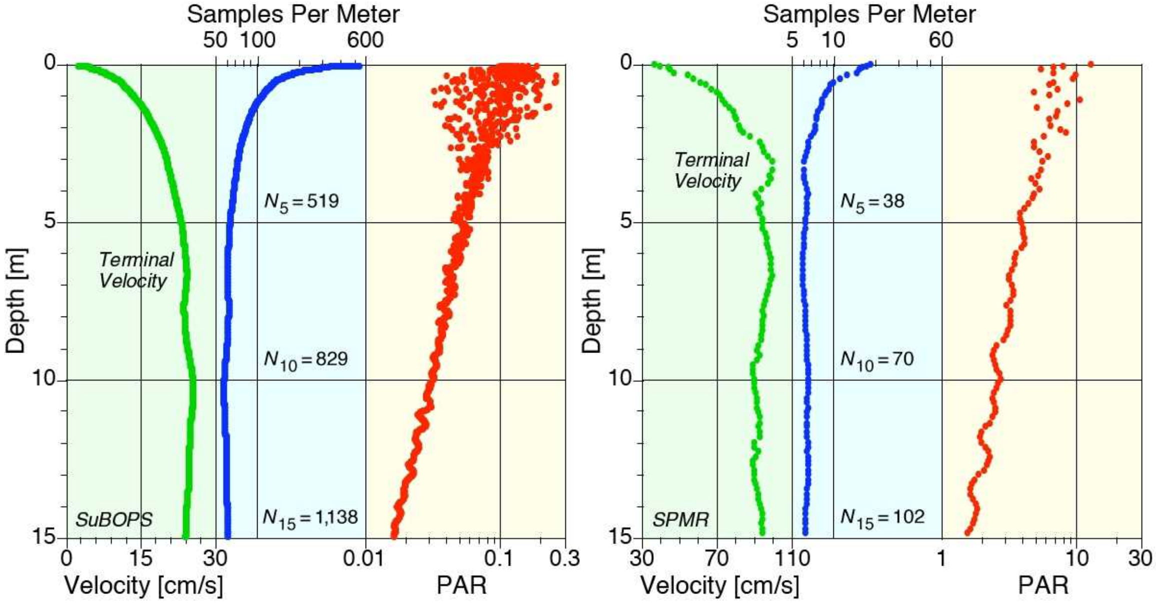

Fig. 17. A comparison of the descent velocity, vertical sampling resolution (samples per meter), and in-water photosynthetically available radiation (PAR) for SuBOPS (left) and an SPMR (right) in open-ocean (Case-1) waters during clear-sky conditions. Only the upper 15 m of the profiles are shown to provide greater detail of near-surface differences.

it moves upward in a vertical orientation with small vertical tilts in many cases. In fact, it is not unusual for the majority of the up cast to have vertical tilts less than 10°. This is significantly different from legacy rocket-shaped profilers, which usually had an attachment point at the end of the instrument, so when the instrument was retrieved, the profiler started to lay over and tilted significantly. A notable exception was the microNESS design, which had a small diameter main housing, a large flat fin area, and an extended side attachment mounting plate (Fig. 11), so it also had a tendency to kite upwards when first retrieved.

The kiting motion is particularly advantageous when trying to keep the profiler at the surface, perhaps because a temporary perturbation needs to pass. For example, when waiting for a cloud to pass over the Sun, the profiler can be *bobbed* at the surface by applying short sharp tugs on the cable. With this technique, the instrument tends to kite up to the surface and stay the same distance away. This is desirable on a boat, because in many cases the boat must maneuver if the profiler starts getting too close, which mixes up the water and takes time. By bobbing the profiler at the surface, the instrument can be kept in a ready-to-deploy mode without much effort.

A tangible expression of the improved resolution that is achieved with SuBOPS is the significant improvement in capturing the high frequency perturbations associated with wave-focusing effects close to the sea surface, as expressed in the Fig. 17 PAR data. A notable consequence of the low SPMR sampling resolution is a significantly aliased sampling of wave-focusing effects during clear-sky conditions—the phenomenon appears as noise. For the SuBOPS data, however, the central tendency of the *in situ* light field close to the sea surface becomes evident. A picture of the SuBOPS prototype fitted with the new flotation capability is presented in Fig. 18. Note the use of two fenders on each radiometer to improve protection during deployment and recovery. The red foam is a custom-blended, low-density polyurethane resin specially formulated to have a very high resistance to penetration by solvents.

Fig. 18. The SuBOPS instrumentation with the custom-blended foam, which can be machined and shaped (the weighted spar is shown not wrapped in black tape for clarity of presentation).

A recurring problem in shallow water, particularly in rivers or tidally influenced coastal waters, is the presence of currents. Currents push against a profiler as it descends and create a tilt bias as a function of depth. Another source of tilt bias is the power-telemetry cable, which when released, starts to sink and pulls against the cable harness attaching the cable to the backplane. Currents and cable tension tend to act along the same axis, because the profiler naturally aligns itself with the current in the direction of the cable when it is held at the surface.

If the axis joining the two radiometers along the long dimension of the backplane is considered the *roll* axis, then the cable and current forces act perpendicular to that axis, which is the *pitch* axis. Roll biases are basically caused by the unequal weights of the two light sensors, and are easily adjusted for by using the movable floats in the second tier of flotation below the main flotation housing. Pitch biases can be more significant and are removed by tilting the sensors in opposition to the bias.

The mechanism used to overcome a tilt bias is based on a two-point system, wherein one point close to one end of the radiometer is fixed and a second point close to the other end of the radiometer is allowed to pivot. The amplitude of the opposing pitch is set by the distance that the sensor is moved relative to the flat backplane (Fig. 19). Both sensors need to be moved the same amount, so there are numeric scales on both radiometers to ensure they are both to the same bias angle (the numeric scale is a convenience, because the distances are easily set and confirmed using a small metal ruler or a caliper).

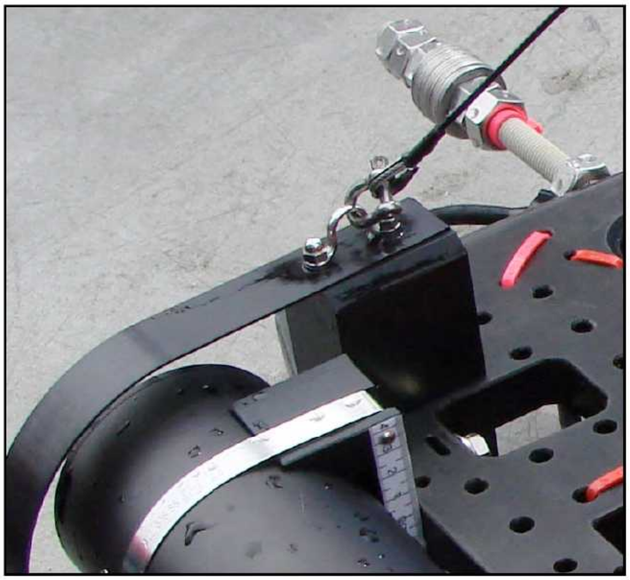

Fig. 19. The SuBOPS instrumentation with the mechanism for adjusting the pitch of the radiometers (left numeric scale) shown in greater detail.

Also shown in Fig. 19 is the weighted spar (which is not wrapped in black tape for clarity of presentation), with stainless steel nuts and washers to finely tune the descent of the profiler. The combination of using small weight adjustments, a pitch bias, a compressible bladder, and movable floats of variable thicknesses, allows the user to trim SuBOPS to a wide range of descent velocities (10–100 $\mathrm{cm\,s^{-1}}$) while maintaining vertical tilts to within 5°. If there is more than one current system within the water column, or if one in particular is especially strong in one depth regime, it may not be possible to find a pitch adjustment that adjust for the ill effects of the current while permitting good tilts outside the influence of the current. It should be possible, however, to find a setting wherein more good data are collected than if the tilt adjustment was not available.

The original mechanical configuration of BSI optical sensors had the pressure transducer and temperature probe fitted in the E_d sensor. The normal location for the latter was on the end cap, which meant it was positioned rather deep in the water column, even when the profiler was close to the surface. This meant that the shallowest observations did not have simultaneous water temperature (T) data, which was a significant disadvantage in optically complex waters, because such waters are frequently characterized by one or more near-surface layers of differing optical properties. For example, in an estuary it is rather typical to have a thin layer of fresh river water overlaying the saltier oceanic water below. To ensure near-surface layers were detectable by more than just their light signatures, a temperature probe was added to the L_u end cap, which meant it was very close to the same plane as the E_d cosine collector (Fig. 20).

Fig. 20. The SuBOPS instrumentation with the extra T probe fitted inside a perforated shroud for protection and mounted on the L_u sensor end cap (bottom right). The multicolored radiance aperture for C-OPS (Chap. 4) is visible in the background (top right).

2.8 Summary

In-water legacy systems are not always well suited for properly resolving the optical complexity of shallow waters, such as near-surface layers, principally because of their large instrument size, proximity of the sampling platform, or high rate of descent. The exceptional performance of the 19-channel PRR-800 made it the ideal foundation for a new profiler specifically designed to meet the unique challenges presented by deployments in optically shallow waters. The first steps in this development were a reduction in the diameter of the housing and minor modifications in the rocket-shape of the existing PRR-800 free-fall collar. The resulting BioPRO system was adaptable and stable enough to deploy in a variety of environments, could utilize the available self-shading algorithms, but was ultimately too long and descended too quickly to use in optically shallow waters.

Comparisons of BioPRO and microNESS (a rocket-shaped legacy profiler) showed that a radically new approach was needed. Inspired by the split PRR-800, the new profiler divided the downward irradiance and upwelling radiance capabilities of the PRR and separated them on either side of a wide, thin plastic back plane, forming a unique, kite-shaped profiler. The new SuBOPS backplane featured semi-rigid foam disks along the top, and stainless steel weights at the bottom, so buoyancy (and, thus, the descent rate) could be finely adjusted. The descending pitch, roll, and rate of fall was controlled by adjusting the amount and position of floats and weights attached to the backplane. At the end of the cast, SuBOPS kites up to the surface by simply hauling in on the power-telemetry cable. With PRR electronics supplying acquisition rates of 12 Hz for all 19 channels, descent speeds of less than $20\,\mathrm{cm\,s^{-1}}$, and vertical resolutions for coastal profiles of 1.0–1.5 cm, observed instrument tilts were regularly less than 5° from the vertical.

Inspired by the excellent results obtained with the prototype unite, three additional innovations were incorporated to the SuBOPS free-fall back plane:

- Replacing the semi-rigid foam flotation disks with a machined, rigid foam material;
- Adding a flotation chamber filled with multiple elongated compressible air bladders to produce a hydrobaric profiling system; and
- Engineering a pivot point in the back plane that allows an adjustment in the mounting angle of the light sensors relative to the backplane.

Even though all three of these innovations improved the amount of high-quality data collected during a profile, the hydrobaric buoyancy system provided the largest increase in data and vertical sampling resolution.

The custom-blended rigid foam is easily machined and impervious to water even after many profiles, ensuring consistent buoyancy from profile to profile, as well as campaign to campaign. A SuBOPS instrument equipped with hydrobaric profiling has a significant capability to loiter very near the surface and sink very slowly (less than $5\,\mathrm{cm\,s^{-1}}$). As the bladder compresses, the descent rate increases until the amount of buoyancy supplied by the air bladder vanishes and terminal velocity is reached. The final improvement with SuBOPS allows the system to be deployed in situations where the telemetry cable is pulling the pitch of the instrument outside of the usable tolerance, such as in tidal currents or riverine outflows. As much as 8° of positive or negative pitch bias in the backplane can be accommodated by pivoting the V-blocks that fasten the instruments to the back plane. Vertical profiles using this system have been acquired at temperate and arctic stations in less than 3 m of water depth with free-fall velocities of less than $10\,\mathrm{cm\,s^{-1}}$, which provides vertical resolutions of less than 1 cm.

Chapter 3

Development of the Microradiometer

Charles R. Booth, John H. Morrow, and Randall N. Lind
Biospherical Instruments, Inc.
San Diego, California

Stanford B. Hooker
NASA Goddard Space Flight Center
Greenbelt, Maryland

Abstract

A microradiometer consists of a photodetector, preamplifier with controllable gain, high resolution (24 bit) analog-to-digital converter (ADC), microprocessor, and an addressable digital port. In other words, it is a fully functional networkable sensor, all of which resides on one small, thin, circuit-board assembly that is sleeved inside a metal cylinder. With the addition of the front-end optics (collector, window, and filter stack), the basic form factor resembles a shortened pencil. The microradiometer design was developed in response to a need for smaller, faster, and potentially less expensive radiometers, which could be easily scaled to either more or fewer channels and more easily deployed in coastal waters. Because each microradiometer channel has an individual ADC, no multiplexer is required, and no cabling is needed, thereby eliminating a source of electronic leakage and improving reliability. The metal cylinder provides additional isolation from electromagnetic interference sources (e.g., radio frequencies). The photodiode current is converted to voltage with an electrometer amplifier with originally two, but subsequently three gain settings, and the resulting voltage is directly fed to the ADC. The entire assembly, including the photodetector, is located on a single circuit board measuring $0.35 \times 3.0\,\mathrm{in}^2$. Each microradiometer is also equipped with a temperature sensor located close to the photodetector. Clusters of microradiometers can be matched with front-end optics to form small, fast, less expensive, multiwavelength radiometers for a variety of measurements. Each cluster is managed by an aggregator that allows the array of individual radiometers, plus any ancillary sensors, to function as a solitary device.

3.1 Introduction

Greater radiometric accuracy, decreased costs, and the need for multidisciplinary research are all technology-forcing challenges to be addressed by the next generation of optical instruments. To develop a commercially successful marine spectroradiometer, the device must also appeal to the majority of investigators working in this field. This effort focused on the development of a *smart photodetector*, called a microradiometer, and its ancillary interface modules. It is not an exaggeration to suggest that a microradiometer can be used anywhere that a filter-photodetector has been used in the past. Thus, it is anticipated that this microradiometer module will become the cornerstone of a wide variety of instruments that help meet these needs.

When research objectives require clusters of microradiometers, the final instrument can be assembled easily by selecting the desired filter assemblies and optical front ends. It is unnecessary to modify the sensitivity of each channel for optimal dynamic range because the sensitivity is dynamically configured. Furthermore, the design eliminates many of the electronic interconnections required in existing radiometer designs, which increases redundancy and improves reliability. The principal benefits to the microradiometer development are:

- Increased radiometric accuracy in the field;
- Decreased instrument size and weight;
- Lower power consumption;
- Enhanced flexibility in the configuration of above- and in-water instruments; and
- Reduced costs associated with production, calibration, maintenance, reconfiguration or modification, and field research.

The culmination of these benefits is the entire analog signal path is of minimum length, free of connectors or cables, and is totally contained in a shielded metal sleeve.

As aquatic research shifts toward coastal monitoring and shallow waters, deployments from small research vessels becomes a necessity. The principal advantages of the microradiometer concept are a) greater accuracy, which permits improved data products in a challenging environment; b) smaller size, which minimizes self shading for in-water instruments; c) reduced weight, which facilitates hand deployment from small boats; and d) lower power consumption, which permits battery-operated scenarios.

Table 1 shows how clusters of microradiometers can be arranged in tubular pressure housings using the MMS concept. The combination of the number of microradiometers and the sensor-housing diameter yields different packing efficiency (P_e) values. Although a 19-channel instrument is not the most efficient, the multiwavelength sensors have rather comparable P_e values. The 19-channel design was chosen for the first C-OPS instrument (Chap. 4), to make comparisons with SuBOPS, the principal legacy instrument (Chap. 2), as comprehensive as possible—the channel configuration was exactly the same for the two profilers.

Table 1. The housing diameter (HD) in centimeters for different clusters of microradiometers as a function of the number of photodetectors, N_P. The packing efficiency, P_e, for an N_P and HD combination is the ratio of N_P times the cross-sectional area of a microradiometer (with clearance) to the cylinder cross-sectional area (minus sidewall thickness).

N_P	*1*	*4*	*7*	*13*	*19*	*31*	*37*
HD	1.3	2.9	3.8	5.3	6.9	7.6	8.5
P_e	1.0	0.7	0.7	0.6	0.6	0.7	0.7

Alternative definitions for P_e are possible, but the one used here attempts to balance the need for maximizing the number of microradiometers while minimizing the size of the sensor housing, so the self-shading effect is constrained as much as possible. In other words, an optimal tradeoff is sought between the need for the maximum amount of spectral information versus the desire to minimize sensor size and self-shading effects. The latter is particularly important for high-quality data products in turbid waters.

Using clusters, a single radiometer approximating the size of a fountain pen or a high-performance, hyperspectral sensor with a diameter less than 9 cm (3.5 in) can be built. From a packing efficiency perspective, *double-ended* 7-channel sensors, with E_d on one end and L_u on the other, would be preferred, because this would provide 14 channels in a 3.8 cm form factor. Two sensors are typically used in a free-fall design, so there is no increase in the number of sensors, just their configuration.

The underlying electronics for all sensor scenarios presented in Table 1 are the same (as is the rated depth for a standard housing, which is 100–150 m), so savings from true economies of scale can be realized—especially for machine-made components where per-unit costs decrease significantly as the numbers produced increase. A depth rating to 350 m is anticipated, but this has not tested or marketed. There is no depth rating on the electronics. Different packing fractions will require different housing components, and each will require some level of redesign. Furthermore, each packing fraction will require different aggregator boards, either some different, or all different. The microradiometers themselves are the same.

3.2 Miniaturization

One early issue in the development of microradiometers concerned the difference between the size of circuit elements that could be manipulated by hand during testing (such as with jumpers, test leads, etc.) and those that are physically too small to manipulate easily without special equipment. The final microradiometer has components that are so small, they must be machine assembled, necessitating batch sizes of 100 or more. Consequently, an intermediate hybrid prototype stage was needed to permit adequate circuit construction and access by hand.

For the hybrid prototype (Fig. 21), the analog front end for data acquisition was built in the final small form factor, while the digital processing and programming portion—where final miniaturization takes place—was scaled to allow human assembly and testing. The comparability of testing of the hybrid with the final design was increased using the same advanced printed circuit board materials and board masking techniques as the final design.

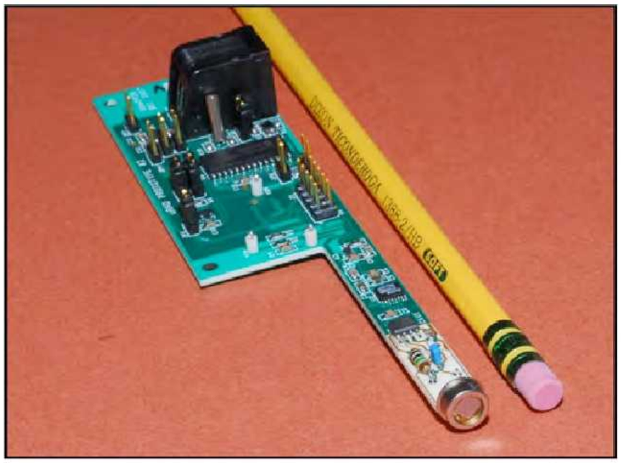

Fig. 21. A hand-made microradiometer prototype. The pencil-shaped board protruding to the right (with the photodetector) is the final form factor, which will be machine assembled (not shown are the *bottom-side* circuits). The larger area behind the protrusion is scaled for human manipulation.

When hybrid testing was completed, the final microradiometer circuit board was laid out for machine manufacturing using the Rogers RO4003C glass reinforced hydrocarbon–ceramic laminate, a lead-free compatible process, coupled to a Parylene encapsulation conformal coating. The entire assembly, with photodetector, is located on a single circuit board measuring $0.35 \times 3.0\,\mathrm{in}^2$ (Fig. 22). A fully assembled microradiometer, with metal sleeve and front-end optics, has a dimension of $0.435 \times 3.79\,\mathrm{in}^2$. The size of the photodetector is a primary driver of the final outside diameter of the microradiometer. Other factors that impact the final outside diameter are the wall thickness limitations of the material and machining for shield tubes and filter sleeves.

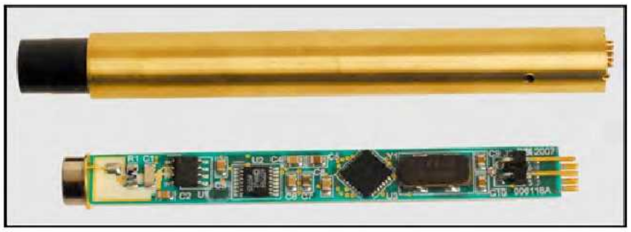

Fig. 22. An individual microradiometer (bottom) and then one sleeved in brass with fore-optics assembled (top). The metal cylinder provides mechanical support and isolation from electronic noise.

3.3 Data Acquisition Sequence

A significant hurdle in developing microradiometers was creating the internal command and control firmware needed to drive the data acquisition. Although designed as standalone *intelligent* photodetectors, up to 200 microradiometers can exist in a multiple-component system. In practice, system expansion is only limited by data rates, and it is useful to understand the sequence of events involved in data acquisition. At the start of data acquisition, all microradiometers are issued a `Sample` command that starts sampling with the desired conversion time and averaging. When a second `Sample` command is issued, the current sample (or sample average) is transferred into a buffer contained within each microradiometer. Data is transmitted to the host computer via an RS-485 or RS-232 protocol. The maximum acquisition rate is, therefore, limited by data transmission and the number of channels configured.

Several of the commands available can be used with a wildcard tag (`*`), so a population of microradiometers can be controlled. For data acquisition, two of these are:

- `ADC Sample Rate` (4–125 Hz); and
- `Averaging Time` up to 4.2 min at 125 Hz sampling.

The following aspects of individual microradiometers are also configured:

- `Input Source`, each microradiometer has three sets of signal sources, although normally only one is used—alternate sources may include grounded input and reference voltage, or temperature;
- `Instrumentation Amplifier`, not used except for bridge sensors (e.g., temperature and pressure);
- `Dark Correction`, the microradiometer enters a mode where it is presumed to be dark, and it averages several readings at all gain settings, which are stored internally as the signal offset;
- `Range Configuration`, high gain, medium gain, low gain, auto gain; and
- `Gain Ratio`, radiometer can alternately sample a source with multiple gains, and compute the ratio and standard deviation of the ratios (but only between adjoining gains).

3.4 Performance Analysis

Performance analysis covers linearity tests over a variety of current levels and at different temperatures. Dark offsets and noise levels are also measured at a variety of current levels. The results of the analyses are compared with reference instruments. An important aspect of the performance obtained is the choice of the photodetector. For the results presented here, the Hamamatsu S1226 series was chosen because of the anticipated wavelengths for C-OPS (Chap. 4), along with a sensible weighting of the advantages and disadvantages of logical alternatives.

The Hamamatsu S1336 and S1337 series, for example, has a better temperature coefficient, but it also has increased infrared (IR) sensitivity relative to the S1226 series, potentially adding out-of-band blocking requirements in certain scenarios. Additionally, it has a decreased shunt resistance relative to the S1226 series, which can amplify front-end low frequency operational amplifier noise. There are additional intricacies in the decision making to select the photodetector, but these two represent the main tradeoffs that were considered in choosing the S1226 series for C-OPS.

The S1336 series is being used for the 1,020 nm channel for OSPREy. This photodiode was qualified for this task after an extensive round of testing, similar to what is presented here. It should also be noted that any system should be subject to a full end-to-end characterization with all of its specified components to evaluate linearity and stability. Different photodiodes cannot be arbitrarily placed in circuits without actually testing the performance of the resulting compound system.

3.4.1 Linearity Characterization

Linearity data were acquired using the flux from a light emitting diode (LED) coupled into an optical fiber assembly that divides the flux from the LED into four output fibers. One of the optical fibers leads to a silicon photodiode attached to a Keithley 6485 Picoampmeter, and the remaining three fibers are directed to microradiometers under test.

The test sequence sets the LED at a variety of different intensities (constant current mode) and then measures the electrometer and microradiometers simultaneously. The test can be run with either random light levels or with a slow ramp, the ramp giving the smoothest results and the random tests may show up autoranging artifacts more easily. The system was fully automated with the LED operating under computer control (Fig. 23). Test results indicate that this device was linear to within ±1% over a dynamic range of eight orders of magnitude and did not saturate at the highest intensity level.

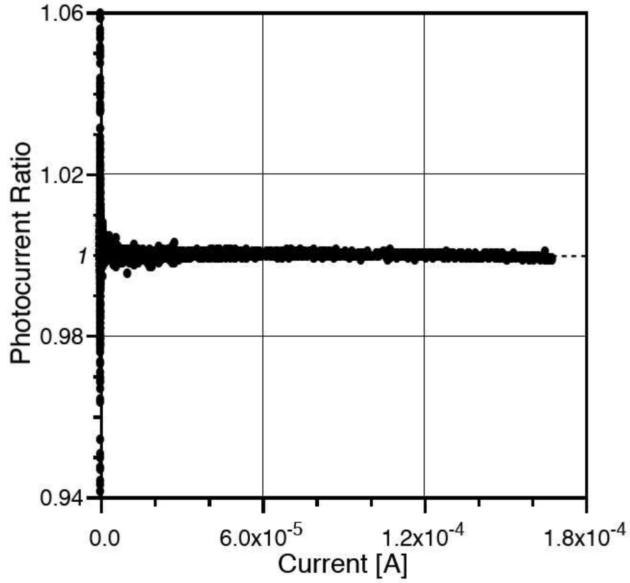

Fig. 23. Measurements of the microradiometer amplifier using final design components and measurements of a reference electrometer.

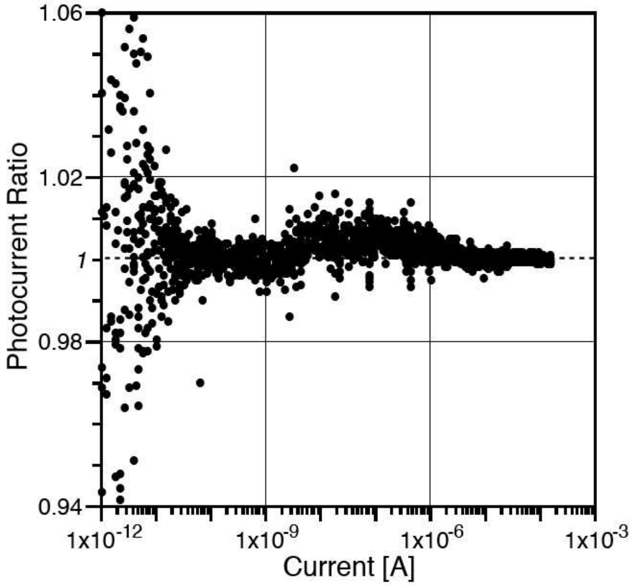

Fig. 24. Same as Fig. 23, but plotted on a semi-log scale. Measurements of the two radiometers agree to within ±1% over the full range, except at signal levels below 5×10^{-11} A, which are affected by noise.

Microradiometers are typically highly linear throughout their range. At the high end, as the signal levels decrease relative to the maximum, the reported noise increases (Fig. 24) because of a combination difficulty controlling LED brightness at levels below 1% of its maximum brightness, limitations in settling time for autoranging, limitations of the electrometer, and the inherent sensitivity of the microradiometers. Microradiometers are also typically linear at the low signal end (Fig. 24), i.e., less than 10 nA of photocurrent.

To verify that the devices would not saturate in full sunlight, a microradiometer was assembled with a 24 KΩ gain resistor and operated on the roof of the BSI facility with a 665 nm filter installed using a radiance front end. The device was pointed at the Sun, and a reading of 52 μA was obtained. This reading is well below the maximum photocurrent for the device. Using a magnifying lens, saturation was produced at a level of 171 μA. This is considerably larger than any natural photocurrent expected anywhere on Earth.

3.4.2 Temperature Characterization

There are several areas where temperature is expected to affect microradiometers: "dark" offset, sensitivity, and stability at the gain switchpoints. To investigate dark offset and gain switchpoint offset, the microradiometers were run over a series of temperature cycles over time. To investigate the sensitivity or gain as a function of temperature, the 19 microradiometers from the first production run were assembled and tested for temperature response. The host data acquisition software was programmed to acquire data at 0.2 Hz. Typically, every 3 min the data acquisition was paused and each microradiometer was polled for temperature. During the series, temperature ranged from below 10°C to above 50°C.

3.4.2.1 Auto or High Gain Offset

The dark offset for a microradiometer is generated by a combination of offsets of various electronic components. At high gain, the normally largest contributor is the operational amplifier (*electrometer amplifier* or *op-amp*), which has two major contributors to the total offset: input offset voltage, and input offset bias current. Input bias current is normally the largest contributor at high gain, and it is multiplied by the amplifier feedback resistor, which is 10^9 at high gain and 10^6 at low gain. The amplifier that is used in the microradiometers is specified with typically very small input bias current (10^{-14}A), but this may reach 4×10^{-12} A at 85°C. The bias current typically doubles every 10°C above 25°C making high temperature operation more sensitive to varying temperature. The range of changes in dark offset voltage with changing temperature during the high gain tests was considerable, ranging from 90 μV to 3,472 μV. Two microradiometers showed negative temperature coefficients, and the majority showed some degree of positive temperature coefficient.

Temperature behaviors are notoriously stochastic. The AD7799 24 bit ADC has an input voltage offset temperature coefficient of 10 nV °C^{-1}, which is much smaller than the op-amp coefficient of 1.3 μV °C^{-1} (but may range over

$\pm 2\,\mu$V and may not even be monotonic). Another accurate way to look at temperature coefficients is to use the separate logged temperature data, which is periodically extracted from the microradiometers. In these data, there is little evidence that the offset is not tracking temperature, as expected. It is evident that there is a considerable difference in the temperature effect between different microradiometers. In particular, the high gain temperature drift has the most impact at temperatures above 30°C.

3.4.2.2 Low Gain

After completing the testing on auto gain, which selects high gain for the microradiometers, the devices were programmed to run on low gain to be able to examine the expected temperature stability and performance near the points where the circuit switches gains. If the device is zeroed at 20°C and its offset drifts up by $30\,\mu$V with respect to the measured signal, the low gain reading will have a maximum temperature-induced error of $30\,\mu\mathrm{V}/\ 3400\,\mu\mathrm{V}$or 0.8% at the switching point. Absent any other errors on the high-gain side, this will result in a 0.8% discontinuity in the transfer function.

For example, a typical microradiometer temperature coefficient has a slope of $-0.00124\,\mathrm{V}\,^{\circ}\mathrm{C}^{-1}$, which corresponds to a measured value of $-1.24\,\mu\mathrm{V}\,^{\circ}\mathrm{C}^{-1}$, or a change of $-0.0365\%\,^{\circ}\mathrm{C}^{-1}$ relative to the gain change point. This implies the microradiometer would have a low gain, offset-induced error of -0.365% for data recorded 10°C above the temperature at which the radiometer was zero corrected. Note that this temperature coefficient is consistent with the specifications in the manufacturer's data sheets ("average drift $1.3\,\mu\mathrm{V}\,^{\circ}\mathrm{C}^{-1}$") for the operation amplifier that is used in this circuit.

If certain applications suggest that an error that approaches these levels at the gain change point is objectionable, then a simple engineering change can be made that increases the low gain level by, for example, a factor of 5. This then allows the gain change point to be raised to 17 mV, which would also reduce the potential nonlinearity, due to temperature shift of the low gain offset, by a factor of 5. It is important to *dark correct* all radiometers near the temperature at which they will be used. Fortunately, temperatures of 53°C should only be seen in heated transfer radiometers, and the changes at lower temperatures are not as significant.

3.4.2.3 Gain Sensitivity

Gain changes due to temperature may arise from changes in the resistor that sets the gain, change in the reference voltage used by the ADC or by the ADC itself, or changes in the responsivity of the photodetector. The ADC specifications state $1.0\,\mathrm{ppm}\,^{\circ}\mathrm{C}^{-1}$. The reference used has a stated stability of $10\,\mathrm{ppm}\,^{\circ}\mathrm{C}^{-1}$, typical, and $25\,\mathrm{ppm}\,^{\circ}\mathrm{C}^{-1}$, max. The $1\,\mathrm{G}\Omega$ resistors are specified at $100\,\mathrm{ppm}\,^{\circ}\mathrm{C}^{-1}$, and the $1\,\mathrm{M}\Omega$ resistors are specified at $25\,\mathrm{ppm}\,^{\circ}\mathrm{C}^{-1}$. The microradiometer systems presented in this report use the Hamamatsu S1226 photodiode, which has a very low responsivity temperature coefficient—almost zero for 400–600 nm. At longer wavelengths, the coefficient starts to increase up to $0.5\%\,^{\circ}\mathrm{C}^{-1}$ at 1,000 nm.

The lineator determines the optical gains at 660 nm, for which the temperature coefficient of the detector is approximately $+0.05\%\,^{\circ}\mathrm{C}^{-1}$. Temperature testing reveals what every field researcher is already aware of: *if an instrument is allowed to overheat in sunshine and is then deployed in the (usually) much colder ocean, temperature effects will be visible in the data.* If a shaded location is not available, covering the instrumentation with a white sheet while outside, and keeping the sheet wet in high temperatures, is a simple but reliable way to prevent excessive solar insolation. The testing also implies that thermally regulated instruments will be the most stable. In most cases, the majority of this error could be addressed by temperature correction.

3.5 Multiple Microradiometer Systems

Microradiometers are standalone photodetectors, but clustering multiple microradiometers together to build a high-performance instrument system requires additional electronics. The exceptional expandability afforded by the use of microradiometers results from an inherent organizational hierarchy that was designed into the system from the outset. Adding to the ease of expandability is the fact that the basic building block of a more complicated sensor is the microradiometer, which is a sensor itself.

Depending on the complexity of the integration, the basic system architecture for instruments built from microradiometers involves three major classes of electronic devices, which are as follows: a) the microradiometers; b) the aggregator components (Fig. 25); and c) the master aggregator components (primarily used in the deck box, which is the controller of larger sensor systems).

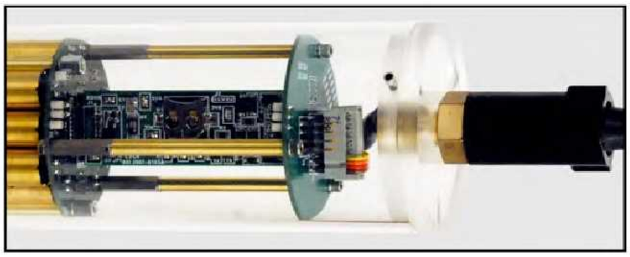

Fig. 25. The aggregator assembly (to the right of the brass microradiometers on the left) within an MMS radiance sensor. The clear acrylic housing is for demonstration purposes only.

Microradiometers are the operational optical sensing units, each with a microprocessor, photodetector, optical filter package, data acquisition system, and communications electronics (Fig. 26). They can be used as individual standalone sensors, but power must be supplied from an external source along with a communications interface. For single-channel applications, e.g., measuring PAR, very small handheld sensors are rather simple to make. For larger sensors with multiple channels, a practical problem is the packing efficiency of the cylindrical microradiometers, so certain channel numbers become critical in minimizing the size of the sensor (Table 1). The total number of channels that can be installed in a sensor need not be installed when the sensor is first built. One of the advantages of the microradiometer architecture is it is relatively easy to replace or add microradiometers to reconfigure or complete a sensor. This flexibility allows a phased approach for resource allocations.

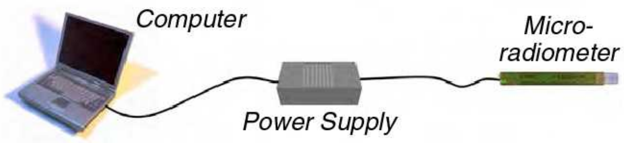

Fig. 26. Individual (or sometimes multiple) microradiometers may be addressed from a computer using a small, external power supply with a communications interface. This is the simplest configuration for single-channel sensors.

Aggregators are used to bundle larger collections of microradiometers (Fig. 27) and ancillary sensors (such as pressure or temperature) in individual instrument sensors. Aggregators control the data flow to and from the microradiometers. They also have onboard removable data storage, which is provided by a microsecure digital (microSD) card, and power control. They also provide additional sensing capabilities including two-axis tilt angles, input voltage and current, plus internal humidity and temperature.

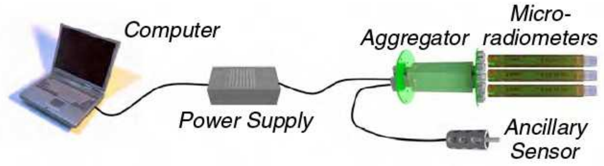

Fig. 27. Adding an aggregator assembly permits the control of data acquisition from multiple microradiometers plus one or more ancillary sensors.

To accommodate the dual objectives of supporting microradiometer clusters plus other smaller form factors, four logic boards are needed. The required functionality is contained physically on two small rectangular circuit boards, $0.88 \times 2.5\,\mathrm{in}^2$. One board is dedicated to generating power supplies for the aggregator and microradiometers, as well as providing transient and over-voltage protection. The other board is dedicated to microprocessor, communications, and memory functions.

The two circuit boards mount parallel to one another with a 1 in round printed circuit assembly (PCA) connector at each end (new production units use round boards as described in Sect. 3.6). One end provides downstream microradiometers with power and communications. The other end handles external communication (full or half duplex RS-485, and RS-232) and raw power, in addition to providing a serial peripheral interface (SPI) bus for peripherals such as the pitch and roll module. The devices are conformal coated to reduce stray currents that can degrade performance, and their gains and offsets are automatically adjusted during calibration at the factory. Ancillary devices can also be based on the microradiometer design to create easily interfaced temperature, atmospheric pressure, or other types of sensors.

Figure 28 shows a partially assembled, 19-channel cluster attached to a base aggregator board. Six more will be installed on the aggregator (three each on the outer rows with four microradiometers) for a total of 19 channels. Optical filter assemblies will be threaded into the metal sleeves for wavelength selection (although, as discussed above, the instrument could be completed later if resources were a limiting factor). Table 1 gives the housing diameters that can be achieved using microradiometer technology. The 7- and 19-channel models are available as COTS instruments for measuring either radiance or irradiance.

Fig. 28. Completed microradiometers are individually sleeved in brass and may be assembled in arrays on an aggregator board. Shown are 13 individual microradiometers.

When multiple sensors are in operation, a deck box with an embedded master aggregator operates as a high-speed controller (Fig. 29). The master aggregator sets the sampling rates and coordinates the polling of all the attached aggregators with their microradiometer assemblies. This is the type of architecture used in aquatic profiling systems, such as C-OPS, or for above water radiometry, such as OSPREy. Indeed, Fig. 29 can easily be interpreted as an E_d and L_u pair with a pressure transducer (top two microradiometers plus ancillary sensor), and a solar reference (bottom microradiometers).

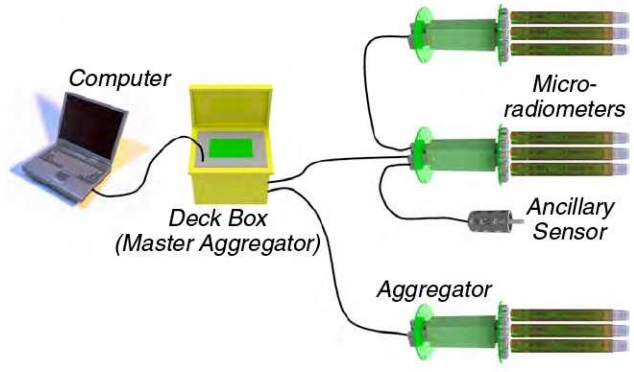

Fig. 29. When multiple sensors are being used, a master aggregator located in the deck box operates as a high-speed controller.

Figure 30 shows a functional multichannel radiance sensor, complete with the optical front end, 19 brass-encased individual microradiometers, and one aggregator assembly. The actual pressure housing for this radiometer, which is made from aluminum (not clear acrylic), is 2.75 in (7 cm) in outside diameter. The different colors of the 19 apertures correspond to the different wavebands selected for each microradiometer.

Fig. 30. A 19-channel radiance sensor built from microradiometers and using the architecture diagrammed in Fig. 27. The clear acrylic housing is for demonstration purposes only.

3.5.1 Irradiance Sensors

The MMS architecture is expandable, and up to 200 microradiometers can be used in a multiple-component system with up to 10 data aggregators. In practice, system expansion for a radiance sensor is only limited by data rates, because each microradiometer, after application of the fore-optics is, in fact, a radiance sensor. Irradiance sensors are considerably more constrained, however, because each microradiometer has to properly view the solitary diffuser used in the construction of the cosine collector.

The fore-optics used with microradiometer irradiance sensors are patterned after the PRR cosine collector. This collector has outstanding directional response and mechanical stability. It was modified once before, but only slightly, to accommodate the smaller-diameter housings required by BioSORS and SuBOPS. For those applications, the primary modification was to scale down from the 4 in diameter of the original PRR housing, to 3.5 in for the BioSORS and SuBOPS sensors. Although the MMS irradiance sensor is smaller still, the modified PRR design proved robust in the past and was the logical starting place to begin designing an MMS irradiance sensor. Note that the size reduction and sensor modifications associated with producing the BioSORS and SuBOPS sensors were part of the first steps in the incremental progression of designing and developing the microradiometer architecture.

The PRR cosine collector was specifically constructed to try and meet the instrument design specifications of the Protocols in an economical and robust design. To cover a wide wavelength range, the irradiance diffuser consists of a raised trapezoidal quartz piece covered with a thin sheet of vacuum-formed Teflon, which acts as a diffuser (Morrow et al. 1994). Thin Teflon diffusers have been used for many years, especially in the construction of UV instruments (Booth et al. 1994). For the PRR, up to 19 filter-photodetector assemblies (FPA) are set in a circular array at the base of the assembly arranged to view the same area at the bottom of the diffuser. To improve the azimuthal response, in addition to the integrating cavity, a secondary Teflon sheet diffuser is installed at the base of the reflecting cavity and the detector array is aimed at this diffuse light source.

As with all flat diffusers, the Fresnel reflectance of the exterior Teflon surface increases at large incidence angles, which significantly decreases the flux. To mitigate this problem, the side walls of the trapezoid dome both increase the signal and provide a surface with a reduced angle of incidence, thereby increasing the response from larger zenith angles. An occluding ring is used to further tune this relationship. The PRR cosine collector agrees with the cosine law to within ±5% for incidence angles less than 70°, and ±10% for the entire working envelope. A cosine collector should not acquire light from angles greater than 90°, so an outer rim raised to the level of the top of the diffuser acts as an additional occluding ring. Symmetrical diagonal notches in the outer rim of an above-water irradiance sensor allows the release of any water that might become trapped in the recessed area between the rim and the diffuser.

To cover a wide spectral range, the Teflon diffuser is coupled to a reflecting cavity, which was carefully designed to function as an optical integrator and to also provide the necessary strength for operation underwater at depths up to 350 m. Underwater, the integrated error in measured irradiance of a uniformly diffuse light field is less than 2.5% throughout the visible spectrum, and less than 1.5% for the corresponding surface reference used in air. In comparison, experimental uncertainties from factors such as alignment of the instrument in the test fixture were observed to contribute as much as 2% uncertainty at 60° and 6% at 80°.

3.5.1.1 The Lens Solution

A microradiometer is a complex assembly of filter, photodetector, acquisition electronics, and microprocessor, all packaged in a thin metal cylinder. For multiple waveband instruments, it is not possible to tilt the individual microradiometers to orient them at the center of the secondary diffuser and still maintain a small sensor diameter, because microradiometers are too long. Several options were considered to solve this problem. The final design uses a single lens to control the FOV and viewing angle, centering each microradiometer on the same area of the lower intermediate diffuser. A conceptual illustration of what an irradiance sensor looks like, using the components discussed here, is presented in Fig. 31.

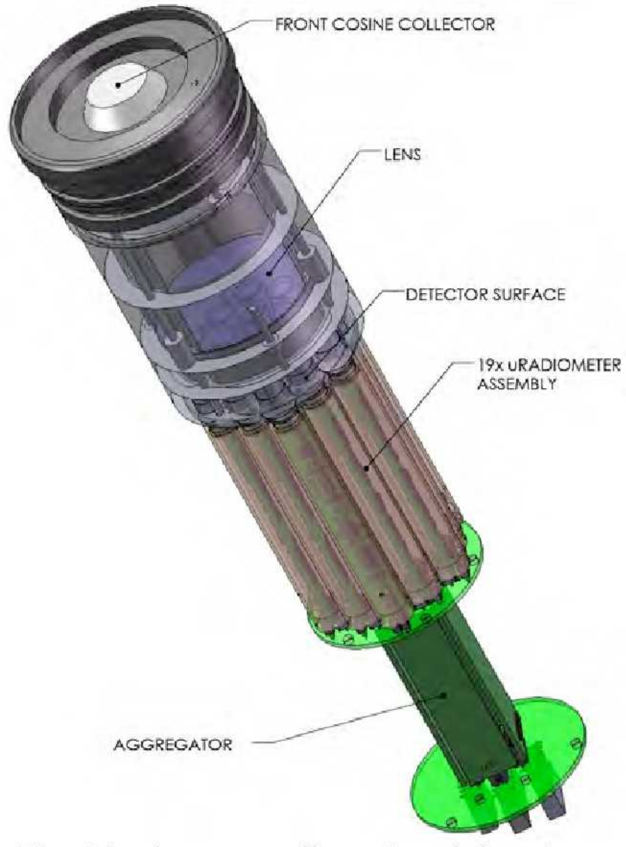

Fig. 31. A cut-away illustration of the primary features of an MMS irradiance 19-channel sensor.

In order to choose the lens, the original PRR design was modeled using `Zeemax` ray-trace software from ZEMAX Development Corp. (Bellevue, Washington). The software was first used to set the *baseline* design. The positional nomenclature for FPA reflects the relationship between the detector and the center of the collector. Given the concentric circular arrangement of detectors, a detector positioned on the outer ring of detectors is referred to as an *edge* detector, because it is closest to the outer edge of the array (and the outer edge of the housing). The centermost detector is called the *center* detector and all others are *middle* detectors occupying intermediate positions in the array.

The angle of incidence (AOI) to the FPA is important, because interference filters change their passband and out-of-band properties with changing AOI. A comparison of the traditional PRR optical design with an early proposed lens design is shown in Fig. 32. The six *spot* plots display the distribution of the radiance intensity of the rays as traced from the rear diffuser impinging on the photodetector, as a function of changes in the AOI. The lens design results in a larger distribution, and the edge pattern (lower right) has significant vignetting and distortion with respect to the baseline image above it. This distortion has two aspects: a) the wider pattern indicates a greater range of angles of flux on the detector (and, thus, through the filters); and b) the vertical asymmetry warns that the position of the photodetector in the array may influence the resulting cosine response, particularly if the field is asymmetrically illuminated.

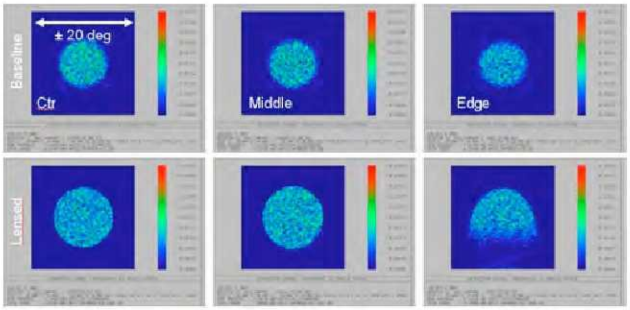

Fig. 32. A comparison of the traditional PRR optical design with a proposed lens design. The plot shows the radiance intensity distributions of the rays from the rear diffuser hitting the photodetector as a function of incidence angle. In these renderings, the PRR baseline is the top row and the candidate lens design is the bottom row.

To better understand the implications of the asymmetrical collector illumination using the lens approach, a PRR cosine collector with an empty instrument body was assembled, and a macro lens with a digital camera was installed to take an image of the second cosine collector while under *worst case* illumination (50 cm from an FEL lamp source). In this instance, the worst case was grazing illumination of the cosine collector where approximately 50% of the collector was illuminated.

Figure 33 shows the image taken of the secondary diffuser of a PRR instrument when the primary diffuser (the cosine collector) is illuminated at an extreme grazing AOI. The left image is untouched, and shows a slightly illuminated crescent on the left side. The image on the right is contrast enhanced (to the maximum) to accentuate the gradient.

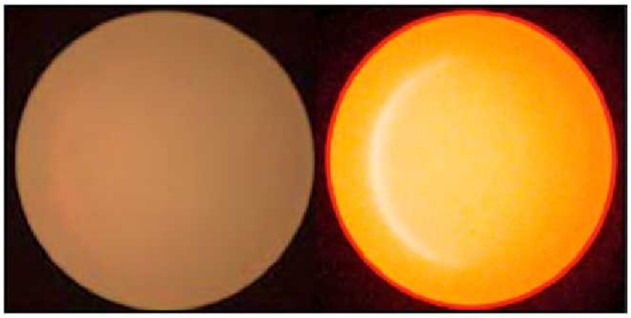

Fig. 33. A digital photograph of the bottom of the secondary diffuser when exposed to extreme grazing illumination angles. The right image has the contrast artificially enhanced.

Color distribution histograms for Fig. 33 show the distribution of color across the surface of the diffuser is affected by the asymmetries. Unlike a normally toned photograph, the ideal histogram shapes in this case would be narrow and Gaussian. Although this was found to be true for the blue channel, the red channel displayed two forms of asymmetry. Horizontal and vertical sections through the image of the collector taken with only the red channel active, showed a semicircle of brighter light on the left side (Fig. 33).

These results indicate the red channel is less diffused than the shorter wavelengths, because the diffuser is less diffuse in the longer wavelengths. As a practical matter, this indicates detectors with longer wavelengths should be positioned at the center of the detector array, and the shorter wavelength detectors at the outer positions where the diffuser is almost completely effective. The use of secondary baffles near the filter to constrain the angular distribution was explored, but this approach was discarded, because it caused too much asymmetry in the imaging of the secondary collector.

A variety of COTS lenses with different focal lengths were modeled using `Zeemax`. The results were evaluated in terms of the amount of asymmetry in the collection of flux from the second diffuser, the range of AOI on the filter, and by total throughput. The final design achieved approximately 20% better collection at the edges, with only a slightly broader AOI distribution. Figure 34 illustrates the relative position of the optical elements comprising the irradiance collector and fore-optics. The commercially available plano-convex lens uniformly projects the flux exiting the secondary diffuser to allow a parallel, radial arrangement of microradiometers.

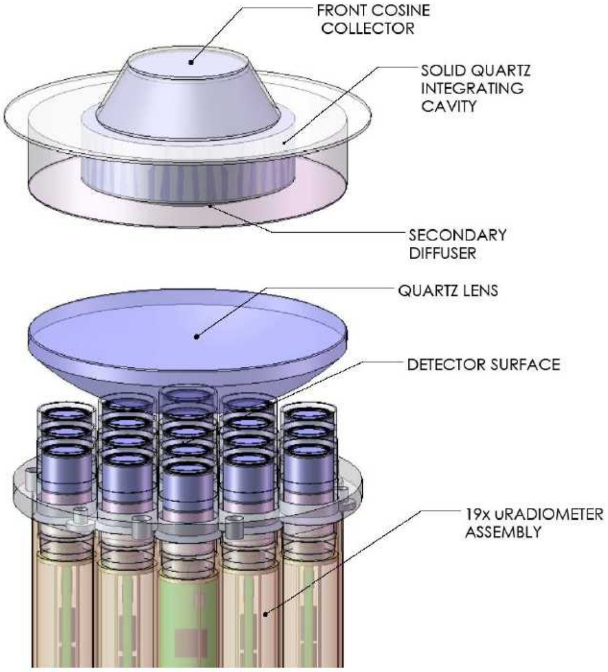

Fig. 34. A magnified illustration of the primary components of an MMS 19-channel irradiance sensor.

3.5.1.2 Irradiance Testing

A full calibration sequence was used to determine how well the irradiance configuration performs. The sensitivity was measured using the standard BSI calibration protocol with the irradiance sensor placed 50 cm from an FEL standard of spectral irradiance traceable to NIST. Data were recorded at a sample rate of 5 Hz, for a period of 60 s, first with the direct beam blocked and then with the beam unblocked. Analysis of the resulting data show an ADC resolution is 0.5 µV and minimum detectable photocurrents of less than 10^{-15} A.

Sensor performance is not just measured using light data—the dark data are equally important. The noise equivalent irradiance (NEI) is the irradiance level equal to the standard deviation of the dark signal. The main gain element, the feedback resistor, is 1 GΩ in the MMS and 10 GΩ in the PRR-800. Because of the lower resistance used with microradiometers, a higher NEI is expected than for the PRR. The noise levels of the MMS sensor is about 1.5 times higher than a PRR, which is expected given the factor of 10 difference in feedback resistors used at the highest gains in the two instruments. The average NEI value for the wavelengths tested was $4.2 \times 10^{-5}\,\mu\mathrm{W\,cm^{-2}\,nm^{-1}}$.

One key part of the field test was to measure the global solar irradiance (Fig. 35), which was done at the BSI rooftop calibration facility. While the tests were marred by a computer crash at 0100 local time, the remainder of the testing was nominal and was completed without incident. The data were originally recorded at 5 Hz. At this rate, 432,000 scans per day were recorded, with each scan containing the average of 25 ADC operations, or around 10^6 observations per day, per channel. No data were discarded before they were subsequently binned into 1 min (boxcar) averages. The small *hump* in the PAR data corresponds to nighttime and is caused by the full Moon, which is clearly seen on the cloudless nights. Although a notable feature in the nighttime data, a temperature-controlled instrument would be better suited for accurately monitoring the monthly lunar cycle.

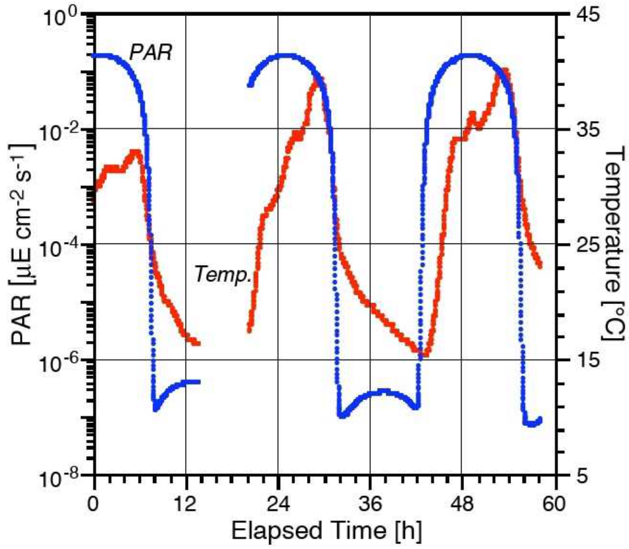

Fig. 35. The global solar irradiance, presented as PAR (blue), and the internal sensor temperature (red) over approximately a 60 h time period starting close to local noon. The data gap is from a failure in the computer used to log the data.

3.5.2 Radiance Sensors

Radiance sensors built using the MMS architecture are considerably less complex than irradiance sensors, because the basic building block—the microradiometer with front-end optics—is essentially a fully functional radiance sensor. The design of the radiance MMS also has roots in the successful PRR radiance design, but is carefully rescaled to a more compact size. Consequently, there are no significantly new aperture components for the radiance sensor, such as the lens that had to be added to the irradiance sensor design.

The radiance design uses a clear quartz pressure window designed for a working depth of up to 350 m. The upper aperture plate, along with the distance from the plate to the detector plane, determines the FOV, while the lower aperture plate and light traps reduce out-of-field stray light. The sensor has an 18° FAFOV in air (13.4° in water). A cut-away illustration showing the relative position of the components is presented in Fig. 36 (compare to Fig. 31).

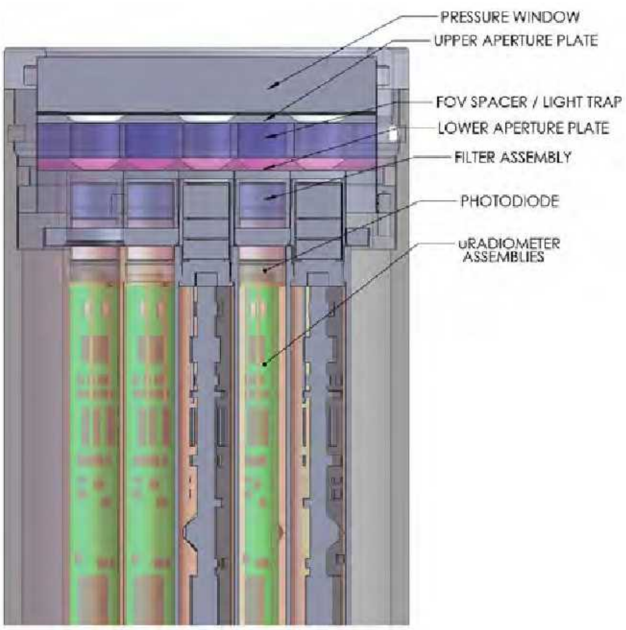

Fig. 36. A cut-away plane view of a 19-channel radiance sensor based on microradiometers.

To determine how microradiometers function in the MMS architecture to measure radiance, a full calibration sequence was performed. The sensitivity was measured using the standard BSI calibration protocol, with a calibrated 100 cm^2 Spectralon plaque at 287.1 cm from an FEL standard of spectral irradiance traceable to NIST. The instrument viewed the plaque at an angle of 45°. Data was recorded at a sample rate of 5 Hz, for a period of 60 s, first with the direct beam blocked and then with the beam unblocked. The computed responsivity of the MMS radiance sensor shows it is slightly more sensitive than the PRR-800 designs.

As noted earlier for irradiance sensors, useful performance information is also derived from dark data. The noise equivalent radiance (NER) is the radiance level equal to the standard deviation of the dark signal. The main gain element, the feedback resistor, is 1 GΩ in the MMS and 10 GΩ in the PRR-800. Because of the lower resistance used with microradiometers, a higher NER is expected than for the PRR. A comparison of the two sensor types, however, shows they are very similar in performance. The average NER value for the wavelengths tested was $3.6 \times 10^{-6}\,\mu\mathrm{W\,cm^{-2}\,nm^{-1}\,sr^{-1}}$ for the microradiometer.

3.5.3 Ancillary Sensors

The following ancillary sensors are regularly integrated into profiling instruments based on clusters of microradiometers: a) water pressure, b) water temperature, c) vertical two-axis tilts (pitch and roll), d) internal nitrogen pressure; and e) internal temperature. Three distinct approaches to data acquisition are used, depending on the sensor type. Water temperature and water pressure are integrated directly with microradiometer-style data acquisition hardware, but benefit from an onboard programmable gate array (PGA). To the aggregator, they appear to be simply *another microradiometer* sharing the firmware command set and data bus. The pressure measurement uses a piezo-resistive silicon, absolute, pressure sensor that is temperature compensated and offset corrected. The sensor is available in a variety of ranges from 0–5 psia up to 0–500 psia. Water temperature is recorded using a custom-manufactured platinum resistance temperature detector (RTD) with a stainless steel probe, which meets or exceeds the International Electrotechnical Commission (IEC) standard 60751.

There are several sensors that are used for engineering monitoring purposes, including internal housing temperature and pressure. The housings are back-filled with dry nitrogen, and a pressure sensor is used to monitor the state of the nitrogen fill. Similarly, the internal electronics temperature is monitored as a diagnostic during extreme temperature conditions and as an additional indicator of overcurrent events. These so-called *housekeeping* channels are integrated to a low resolution, 10-bit ADC located on an aggregator PCA.

Instrument two-axis tilt (pitch and roll) is monitored using a low-power, dual-axis 1.7 g accelerometer with an SPI digital interface. Data are harvested from the SPI and integrated into the data stream as an ancillary channel.

3.5.4 MMS Deck Box

Monitoring for sensor problems and determining their cause(s) is an important function for ensuring successful field deployments and good science. In-water instruments can sometimes fail because of housing leaks. Deployment conditions in the field sometimes require cables that are hundreds of meters long, and experience has shown time and again that field failures are frequently caused by connector or cable problems. In anticipation of these issues, strategies and protocols can be used to reduce the complexities of deploying instruments in the field. Part of the mitigation strategy adopted with MMS instruments is as follows:

- Each microradiometer can monitor its supply voltages.
- Each aggregator can measure each of the regulated voltages it produces.
- Each aggregator can measure its input voltage and the current it is drawing.
- Each aggregator has a built-in pressure sensor to monitor the atmosphere in the instrument and detect leaks.
- The master aggregator (usually in the deck box) automatically queries each aggregator attached to it, and verifies the voltage levels at the aggregators, and then adjusts the voltage to run the subordinate aggregators at the optimum voltage, thereby eliminating power supply issues caused by increased loads or resistances.
- The master aggregator can turn off power to either the surface or underwater sensor assemblies if it detects abnormal power draw or lack of proper response from the remote sensors.

The deck box (Fig. 37), which usually contains the master aggregator, also has a four-line liquid crystal display (LCD). The LCD provides feedback to the operator when power is applied. Specifically, the display shows how many sensors are found, the battery voltage (in the case of battery power), and warnings of unusual voltage or current levels. This is all done, even if the computer used for data acquisition is not connected. When the data acquisition software is operational, the host can be configured to display messages on the deck box LCD.

Fig. 37. The front panel of the deck box used with optical instruments built with the MMS architecture. The LCD is the green rectangle in the bottom-middle portion of the panel.

The deck box is configured to communicate with the computer using either RS-232 or RS-485 protocols, both at 115,000 baud. The RS-232 signaling was selected as the primary deck box-to-computer protocol because, unlike RS-485, it is native to many computers. In the future, microradiometer deck boxes will be built with a Universal Serial Bus (USB) interface. Compared to USB, RS-232 is much closer to the raw logic level communications from the microprocessors used in the deck box and other system components. Although USB is becoming increasingly common, RS-232 is enormously robust and has worked well for many years.

Communications between the deck box and remote aggregators use RS-232 or RS-485 signaling and either full- or half-duplex. Initially, full-duplex RS-485 was chosen based on the extensive experience with it. Subsequently, a half-duplex version has been qualified and is being field tested. Half-duplex is attractive because it reduces the number of conductors in connectors at the sensors, which should increase reliability. Cable size and weight will also be reduced.

In addition to the direct deck box status display, each microradiometer has a set of diagnostic flags that can be reported on request. In a similar fashion, the aggregators also have a set of flags to provide alerts regarding a variety of communications and sampling problems. Aggregators also report the voltage and current at the sensor inputs, internal temperature, and in more recent units, pressure of an internal inert gas fill.

3.5.5 MMS Operational Details

During the development of the MMS architecture, several methods of running the microradiometers were considered, including choosing the sample rate of the ADC (rates from 4–500 Hz were available). Microradiometer prototypes at a variety of sample speeds were tested and compared to sampling theory and the published data sheets for the components. The choice of 125 Hz operation was based on the range choice that the microprocessor makes when sampling the analog input. If the microprocessor detects that the sensitivity is too low, then the gain of the circuit is increased, and the following three samples are rejected to allow for a settling time of the analog front end, and the next sample is processed.

After the readings are made, and if more than three consecutive readings on the same range (either high or low) have been made, then the offset stored in memory for that range setting is subtracted from the ADC reading, and the resulting number is multiplied by the scale factor for the range. Each of these parameters, the number of readings to skip, the range delay after changing ranges, the scales for each gain, and the offsets for each gain, can be set by the user. In addition, automated routines in each microradiometer allows for the determination of the gains and offsets assuming appropriate conditions at the front end (like light or dark) are present.

Because of range changing, and the need for settling time plus the desire not to report missing data if a range change occurs, a fast sampling rate was needed. Testing revealed that even given averaging, noise increased at rates over 125 Hz, so the 125 Hz rate was selected, because it allowed at least one sample in every data transmission if there was only one gain range event. Missing data (coded as `-999`) can occur when there are multiple range changes occurring during the sample average period, but this is exceedingly difficult to avoid in any autoranging system.

A truly synchronous system could have been designed, with all microradiometers sampling at exactly the same instant, but this would have required a master clock propagated from the master aggregator; the overhead for this requirement was considered undesirable. Consequently, the ADC units were allowed to run freely, which means they are not quite synchronous, or, depending on the viewpoint, are synchronous to within 8 ms. The latter is considerably faster than the bandwidth of the system.

A key aspect of being able to operate a system built with microradiometers is that it must run dependably at the selected sampling rate. Ensuring this task executed reliably required considerable testing and code revisions. In the course of documenting the system performance presented here, the system consisted of three 19-channel sensors (57 microradiometers), plus a coordinating master aggregator operating at a 20 Hz. Each microradiometer was continuously converting in autoranging mode at a rate of 125 Hz. This means that there were over six ADC cycles performed during each sample report. The individual microradiometers asynchronously convert and store a running average of the measured signal.

An example of the sequence used to document system performance is as follows:

1. The master aggregator issues a `W` command to the subordinate aggregator to start polled sampling.
2. The receiving aggregator zeros the sampling buffer-accumulator as sampling continues. In the case of 20 Hz sampling, 50 ms after the original start command, a second start command is sent from the master aggregator, passed down through each attached aggregator, to the microradiometers.
3. Each microradiometer then transfers its accumulated reading to the transfer buffer, zeroes its accumulator, and continues sampling, all without significantly interrupting its continuous sampling at 125 Hz.
4. Following this second start command, each aggregator serially requests readings from the microradiometers that are attached to it, placing the data into a transfer buffer. At the same time, the master aggregator asks the first attached aggregator for its data and waits for a reply.
5. After the data arrives, it queries the next aggregator, and so on, until it has all the data, at which point it issues a new start command and the sequence repeats.

Note that this entire sequence must happen at the required sample rate.

To run as quickly as possible, timing gaps must be used very efficiently. For the current MMS architecture, it should be possible for four sensors to run at the same nominal (15 Hz) rate. If faster operations are needed, there are several housekeeping characters in the microradiometer-to-aggregator communications scheme that could be eliminated. In any case, four 38-channel sensors operating at 15 Hz can be accommodated with standard 115 Kbaud communications and existing hardware. To increase beyond that, 230 Kbaud communications may be required.

3.6 Improvements and Enhancements

The original two-gain microradiometer was introduced in 2008. While performance was excellent for marine applications, when the application of microradiometers was recently expanded to include sun photometry in support of the OSPREy project, the maximum signal level that the device could accommodate proved too low. Because the sun photometry application involves having the same radiometer also view the very bright Sun as well as the much darker sea surface (to derive a water-leaving radiance), more dynamic range was required and this led to the three-gain microradiometer (3GμR).

The original microradiometer gains were separated by a nominal factor of 1,000, while the 3GμR employs three gains separated by a factor of 200. The analog front end 3GμR was redesigned with different components, but the physical package outline and connections remained identical as shown in Fig. 38 (compare to Fig. 22).

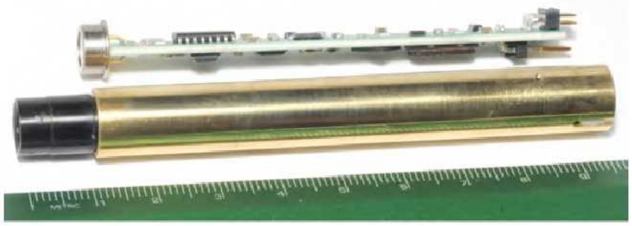

Fig. 38. A side view of a 3GμR microradiometer (top) showing the two-sided circuit board design, and a sleeved version with fore-optics attached (bottom). The ruler is marked in centimeters.

Adding a third gain stage had several advantages:

- The difference between the gains was reduced from 1,000 to 200, which decreases the stabilization time needed after a gain change.
- The voltages at which gains increase were increased by a factor of 2.5 resulting in a decrease of the medium and low gain offset uncertainty.
- The photocurrent signal range was increased to accommodate 40 times higher saturating signal levels (160 μA).

The circuit architecture of both the two- and three-gain microradiometers is very similar. The photodetector is connected to a high performance operational amplifier. The amplifier is configured as a current-to-voltage converter with the gain set using a resistor and capacitor combination selected by an analog switch. The resulting voltage is digitized by a 24 bit ADC normally running at 125 Hz. The 3GμR has an ADC resolution of 0.5 μV, and at maximum gain, a current resolution of less than 1 fA.

A microprocessor controls the switch and ADC, implements autoranging, and calculates a running average. By operating at 125 Hz, range changes can usually be made (and time allowed for settling) while maintaining an uninterrupted stream at rates as high as 20 Hz. Before each reading is averaged, it is corrected for offset and gain and is expressed as a floating point number, which is then added to the average. If a range change occurs during an averaging period, readings can be dropped while still being able to calculate and report an average, which minimizes data gaps at signal regions where gain changes occur.

The firmware contains modes for automatically determining dark offsets at each gain, gain ratios when exposed to appropriate light levels, and configuring various operation modes such as ranging mode, switch points, and other parameters. It is also possible to program the system for manual gain, different ADC sample rates ranging from 4–125 Hz, and sample averaging periods from over 20 Hz to periods up to a minute.

Both versions of the microradiometer contain a temperature sensor, and circuitry to monitor the supply voltages. Measurements of single 3GμR devices indicate that when configured for radiance measurement (14° FOV) at 490 nm, the saturating radiance is $8.5\,\mathrm{mW\,cm^{-2}\,nm^{-1}\,sr^{-1}}$, and the detection limit is $0.14\,\mathrm{pW\,cm^{-2}\,nm^{-1}\,sr^{-1}}$ at 1 Hz. This represents a range of approximately 6×10^{10}.

Another advancement since the production of the prototype MMS instrument, is the reduction in size associated with the aggregator assembly. A so-called *short-stack* aggregator design repackages most of the components from the original aggregator, deleting the data storage card, but adding connectors for additional microradiometers connected via cable (enabling a radiometer design with arrays at each end), and for the addition of data storage mounted on an additional small circuit board. A picture of the new aggregator, which is about 4.7 cm shorter than the original (Fig. 25), presented in Fig. 39.

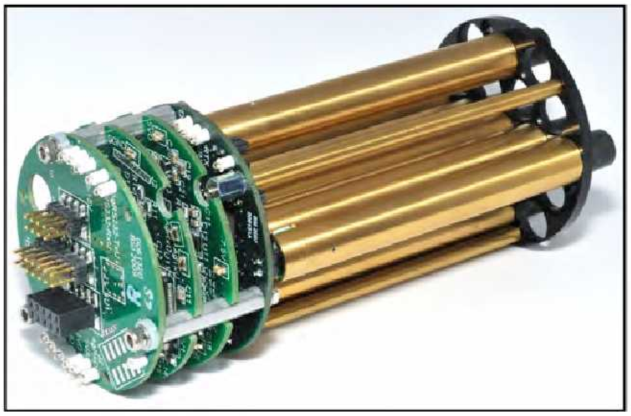

Fig. 39. The new aggregator board assembly (left) shown with a 19-channel array populated with seven microradiometers for clarity. From left to right are the connector board providing interface with external devices and RS232, RS485, and microradiometer data busses. The second board is the microprocessor board, followed by the power supply board, the microradiometer interface and connector board, and finally, the microradiometers in brass cylinders with fore-optics attached.

Although compact, numerous test points are provided as part of the new design. The new aggregator configuration also provides a physical pathway to route a rigid optical fiber assembly, a provision that the OSPREy radiometers use to combine spectrograph and microradiometer technologies in the same instrument. An internal pressure sensor is also included that allows integrity monitoring of the 30 psi dry nitrogen fill of the instrument cavity. This aggregator retains the same power conditioning circuitry, real-time clock, RS-232, RS-485, two-axis tilt sensor, and firmware as the original aggregator.

3.7 Microradiometer Specifications

Each microradiometer contains its own complete control and acquisition system composed of a microprocessor, 24 bit ADC, voltage reference, temperature sensor, and electrometer front end. The electrometer is configured with three gains controlling the conversion of current to voltage.

A cluster of microradiometers, typically sampling different wavelengths, is controlled by an aggregator which synchronizes the polling and acquisition of signals from each of the individual microradiometers to ensure simultaneous sampling at all wavelengths. The aggregator also contains the power conditioning circuitry and data communications interfaces, and may also be equipped with internal data storage (1 GB microSD card) to support remote data logging.

The principal specifications of sensors built with microradiometers are as follows:

- *Detectors:* Silicone (Si), indium gallium arsenide (InGaAs), or gallium arsenide phosphide (GaAsP). The form factors for the three types of detectors are 13 mm^2 for the former, and 7 mm^2 for the latter two, respectively.
- *Photocurrent-to-Voltage Conversion:* Electrometer amplifier with three gain stages—1, 200, and 40,000.
- *ADC:* 24-bit bipolar, 4–125 Hz data rates.
- *Dynamic Range:* A little more than nine decades (usable).
- *Linearity:* Measured on all microradiometers over a signal current range of from 1×10^{-12} to 1×10^{-5} A using a programmable light source. Typically, errors are to within 1% compared to a reference system electrometer. Gain ratios are individually measured using a computer-controlled optical source and are programmed into each microradiometer.
- *Speed:* ADC sample rate is programmable from 4–125 Hz, and is normally set to 125 Hz, with averaging over the sampling period performed internally by the microradiometer.
- *Response Time:* Exponential change with a time constant less than 0.01 s. The time required for gain change is less than 0.1 s.
- *Electronic Sensitivity:* ADC resolution is 0.5 μV with a current resolution of less than 1 fA. The saturation current is 160 μA and the minimum detectable signal is less than 10^{-15} A.
- *Noise:* The Si detector typically has 15–20 fA of noise when the ADC is sampling at 125 Hz with the internal microradiometer averaging of 25 samples, resulting in a data rate of 5 Hz.
- *Optical Sensitivity:* Sensitivity depends on the spectral region and the choice of irradiance or radiance entrance optics (Table 2).

Table 2. The optical sensitivity of microradiometers expressed as noise equivalent signals at 5 Hz for radiance ($\mu\mathrm{W\,cm^{-2}\,nm^{-1}\,sr^{-1}}$) and irradiance ($\mu\mathrm{W\,cm^{-2}\,nm^{-1}}$). Radiance is adjusted for immersion in water. Typical wavelengths spanning the normal spectral range of C-OPS profiling systems are shown.

Channel	*Radiance*	*Irradiance*
320 [nm]	2.9×10^{-6}	9.0×10^{-5}
395	5.0×10^{-6}	6.9×10^{-5}
490	1.8×10^{-6}	2.3×10^{-5}
683	9.9×10^{-7}	1.1×10^{-5}
780	6.8×10^{-7}	8.0×10^{-6}

- *Dark Offsets:* Dark offsets are measured and set at the time of calibration for each gain level. Offsets can also be automatically measured and applied in the field to accommodate different temperature regimes.
- *Microradiometer Power:* ±5 VDC at 4 mA total.
- *Optical Filters:* 10 nm FWHM multicavity ion-deposited interference filters selected for greatest out-of-band blocking and minimum fluorescence and maximum long-term stability.
- *Spectral Range:* 250–1,650 nm (1,100–1,650 nm requires InGaAs detectors).
- *System Sampling Rate:* System sampling rate depends on the number of sensors and channels being controlled. For a standard in-water system—composed of three 19-channel sensors measuring E_d, L_u, and $E_d(0^+)$, plus pressure, two-axis tilts in both irradiance sensors, and water temperature—a system sampling rate of 12 Hz is reliably achieved.
- *Radiance Size:* A 19-channel in-water radiance sensor has a diameter of 6.9 cm, a length of 25 cm, and a weight of 1.6 kg.
- *Irradiance Size:* A 19-channel in-water irradiance sensor (with a pressure transducer, two-axis tilt sensors, and a water temperature probe) has a diameter of 6.9 cm, a length of 34 cm, and a weight of 1.7 kg.

3.8 Summary

Microradiometers represent a next-generation change in the technology available to acquire high-quality optical measurements for field and laboratory applications. The MMS architecture was developed with the intent of immediately using it in a next-generation in-water profiler, i.e., C-OPS. Consequently, much of the design effort was evaluated from the perspective of the imagined new instrument. One of the anticipated benefits of using the microradiometer technology was the opportunity for an unprecedented amount of simplicity in assembly and repair. Both of these accomplishments were expected to reduce the cost of acquiring and maintaining sensors with a state-of-the-art observational capability.

Prior to C-OPS, changing, replacing, or repairing a filter or filter-photodetector combination required disassembly of the entire electro-optics section of the instrument, which was a time-consuming and tedious procedure with the added risk of unintended damage to associated components. Significant effort was subsequently required to test the subassemblies and then recalibrate the sensor.

In contrast, changing a filter or replacement of an entire microradiometer with C-OPS requires only a few hours to unplug the component and replace it before recalibrating. In addition to the savings in time (and money), the potential for unintentional damage is minimized with the microradiometer design, because so much of the electronics is modular. Consequently, there are significantly fewer connectors and cables that must be dealt with. Compare, for example, the partially disassembled PRR-800 irradiance sensor shown in Fig. 40 with the microradiometer equivalent shown in Fig. 31. Note also the number of cables and connectors in Fig. 40, most of which carry low-level analog signals, versus the absence of these in Fig. 39.

Fig. 40. A PRR-800 irradiance sensor with pressure housing removed. Visible are individual coaxial cables conducting the detector photocurrents to a stack of five input amplifier boards (with four channels per board). Completing the stack is an ancillary input board for temperature, pressure, and angle, the microprocessor board, and the multiplexer digitization board.

Chapter 4

The Compact-Optical Profiling System (C-OPS)

John H. Morrow, Charles R. Booth, and Randall N. Lind
Biospherical Instruments, Inc.
San Diego, California

Stanford B. Hooker
NASA Goddard Space Flight Center
Greenbelt, Maryland

Abstract

The C-OPS instrument successfully integrates a number of new technologies, each focused on different aspects of the practical problem of resolving the optical complexity of the near-shore water column. Although C-OPS represents a significant improvement over BioPRO and other legacy profilers, C-OPS was designed from inception specifically to operate in shallow coastal waters and from a wide variety of deployment platforms. In terms of the mechanics of operating the instrumentation and its behavior during descent, the most significant improvement was to change the basic design for mounting the light sensors from a rocket-shaped deployment system, used in legacy profilers, to the kite-shaped backplane developed for SuBOPS (Chap. 2). This change allowed the flotation to be distributed as a primary hydrobaric buoyancy chamber along the top of the profiler, plus an adjustable secondary set of one or more movable floats immediately below. The primary set provides the upward buoyant thrust to keep the profiler vertically oriented. The secondary set, coupled with an adjustment mechanism perpendicular to the flotation adjustment axis is used to ensure the two light sensors are level. The hydrobaric buoyancy chamber can contain one to three air-filled bladders, which compress slowly and allow the profiler to loiter close to the sea surface, thereby significantly improving the vertical sampling resolution in near-surface waters. Electronically, the system is self-organizing; when initially powered, the aggregator queries each sensor to determine optimal power required for operation over the existing length of the cables and the population of detectors available to the configuration. Typically, each sensor geometry (E_d, E_u, and L_u) is composed of 19 microradiometer detectors, clustered using the MMS hierarchical architecture coordinated through a master aggregator (Chap. 3). Although the use of microradiometers provides improvements in a variety of operational specifications compared to SuBOPS (e.g., reduced electronic noise and slightly faster data acquisition rates), most notable is the reduction in instrument diameter: C-OPS light sensors use a 2.75 in (7 cm) outside diameter housing, which is 27% smaller in diameter than SuBOPS.

4.1 Introduction

The C-OPS instrument is a culmination of several new technologies, each focused on different aspects of resolving the optical complexity of the near-shore water column. Although C-OPS represents a significant improvement over BioPRO and other legacy profilers, it was designed from inception specifically to operate in shallow coastal waters and from a wide variety of platforms ranging from offshore towers, small boats, and ocean-class research vessels. Electronically, the system is self-organizing; when initially powered, the aggregator queries each instrument to determine the optimal power required for operation over the existing length of the cables and the population of detectors available to the configuration.

Typically, each radiometer (E_d, E_u, and L_u) is composed of 19 individual microradiometer detectors, which are controlled as a single cluster using the MMS hierarchical architecture (Chap. 3). The operation of each cluster is coordinated through a master aggregator (Fig. 29), which is usually the (power and telemetry) deck box. Although the use of microradiometers affords improvements in a variety of operational specifications compared to SuBOPS (e.g., reduced electronic noise and slightly faster data acquisition rates), the most notable enhancement is the reduction in size and weight for the optical sensors. The C-OPS sensors have a 2.75 in (7.0 cm) diameter, which is 27% smaller in diameter than the 3.5 in (8.9 cm) PRR-800 sensors used with SuBOPS.

4.2 C-OPS Description

To function well in shallow coastal waters, the C-OPS instrument uses the basic SuBOPS design featuring two parallel sensors mounted symmetrically on either side of a kite-shaped free-fall backplane (Fig. 41). The sensors use microradiometer clusters housed in a 2.75 in (7 cm) in diameter aluminum cylinder that is 27% smaller in diameter than SuBOPS. The pressure transducer for C-OPS is installed on the upper surface of the upwelling radiance or irradiance instruments.

The original twin V-block pairs used to mount the SuBOPS sensors were changed to single elongated blocks for ease in adjusting the pitch orientation of the sensors. As with SuBOPS, roll adjustment is accomplished by controlling the distribution of secondary floats laterally. The lateral floats were redesigned with a slot, so they can slide easily into position and fiberglass nuts are used to hold them in place. A temperature sensor can be mounted on either end cap, but the L_u sensor end cap is preferred, because this permits measurements very close to the sea surface.

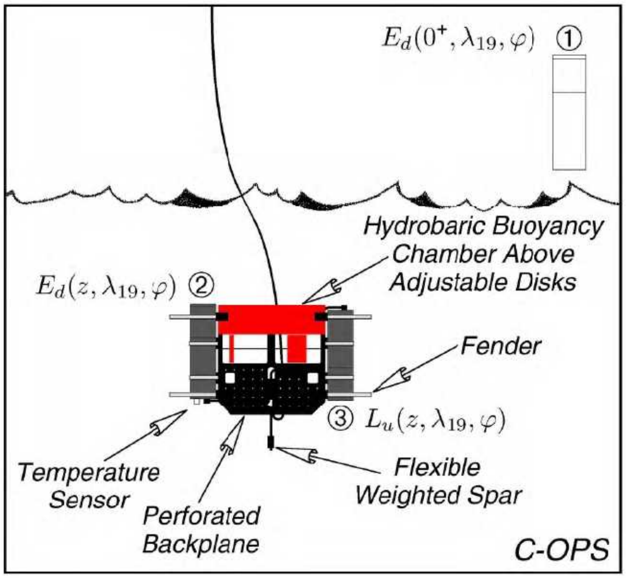

Fig. 41. A schematic of the first C-OPS instrument; newer models have the temperature probe mounted on the L_u endcap to permit measurements as close to the sea surface as possible. Any needed weight is added to a bottom-pointing flexible spar.

The rigid spar used with SuBOPS could be damaged during the recovery of the profiler, so it was replaced by a plastic flexible spar for C-OPS. The flexible spar somewhat protects the L_u aperture in the case of an accidental bottom impact, because it hits the bottom first, but the primary protection for C-OPS is that it is usually tuned for slow descent rates (typically about a $20\,\mathrm{cm\,s^{-1}}$ terminal velocity). The flexibility of the material has additional advantages as a counterpoise in buoyancy control. As with SuBOPS, the main rigid foam buoyancy element features a hollow chamber that can hold 355 mL of air in compressible bladders (Fig. 42) or a combination of bladders and incompressible foam.

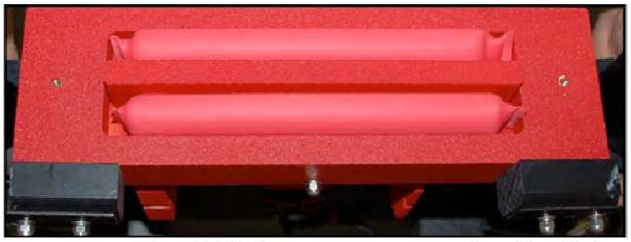

Fig. 42. The C-OPS main buoyancy chamber hollowed out and fitted with two bladders plus a solid foam insert. The removable flotation pieces for adjusting the roll stability of the backplane, with one piece to the left and one to the right, can be seen just below.

4.3 Design

The C-OPS instrument architecture was designed to be inherently flexible. The core elements can be added or removed to accommodate a wide range of research activities. Microradiometers are used as the photodetector elements in all of the light sensors; aggregators ensure that ancillary sensors (e.g., temperature, pressure, pitch, and roll) featured in an instrument are integrated into a single data stream with the microradiometers. As a complete system for the discussion presented here, C-OPS consists of a solar reference with BioSHADE accessory (Chap. 5), two in-water light sensors (selected from E_d, E_u, and L_u), a deck box, and the cabling that connects them all together. Figure 43 shows the interrelationship between the different components used in C-OPS.

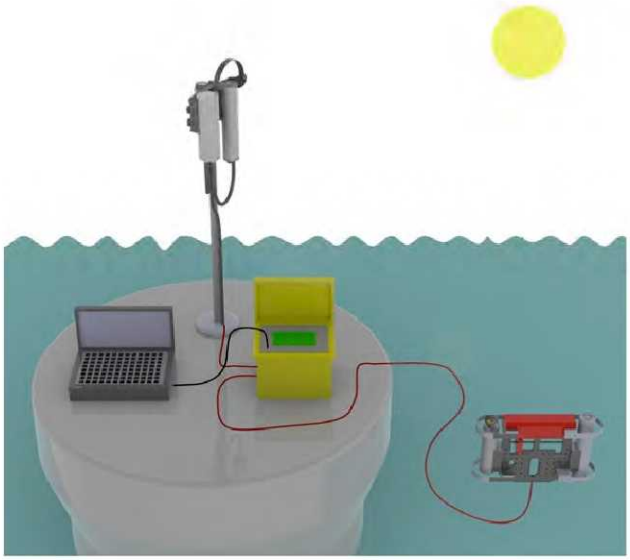

Fig. 43. The C-OPS components configured together showing how the above- and in-water components communicate as sensor groups over corresponding dedicated cables.

Table 3. The specifications for the data-telemetry (sea) cables used with the BioPRO, SuBOPS, and C-OPS free-fall optical instruments. Because SuBOPS was the transition instrument between the legacy (PRR-800) sensors and the new microradiometer sensors, the new cable characteristics were specified using SuBOPS and then evaluated with C-OPS. The three internal synthetics involved are polyethylene (PE), polyurethane (PU), and polypropylene (PP). Conductor specifications are given in American Wire Gauge (AWG) sizes. Bulkhead connectors on the light sensors and deck box are SubConn Micro 6-pin male connectors with female locking sleeves, and SubConn Micro 6-pin female connectors with female locking sleeves, respectively.

Cable Characteristic	*Red Polyester Overbraid Cable*	*Pale Red Polyurethane Cable*
Manufacturer	Cortland Cable Company	Storm Products
Power Conductors	2×20 AWG with PE Insulation	2×20 AWG with PP Insulation
Telemetry Conductors†	4×24 AWG with PE Insulation	4×24 AWG with PP Insulation
Outer Diameter	0.320 in (nominal)	0.320 in (nominal)
Strength Member	Kevlar (1,000 lb breaking rating)	Kevlar (500 lb breaking rating)
Outer Jacket	Black PU with Red Polyester Overbraid	Red Low-Density PU
Connectors	SubConn Micro In-Line (MCIL6)	SubConn Micro In-Line (MCIL6)
Instruments	BioPRO and SuBOPS	SuBOPS and C-OPS

† The four data telemetry conductors are packaged as two individual sets of twisted, shielded pairs.

All C-OPS instruments require a master aggregator (the deck box) to provide power, coordinate data streams from the individual instruments, and deliver data to a computer. There is no requirement to use all components at all times, and because the deck box polls all elements at the time the system is started, it is self organizing; data acquisition does not require a description of the configuration before recording takes place. In the most common C-OPS configuration, a 19-channel solar reference is used to measure spectral global irradiance. A BioSHADE with the optional Biospherical GPS (BioGPS) unit (Chap. 5) can be attached to the reference to add a shadowband capability to the data stream as well as position and time.

Once the system is configured, the RS-485 signals from the above- and in-water components are combined in the deck box and converted to RS-232 communications for computer logging. The RS-232 data are recorded on a laptop computer using commercial software developed by BSI, or custom-built software developed by RSMAS in partnership with NASA. The latter is a continuing testbed for evaluating desired changes in the Protocols associated with deploying the instrumentation.

The deck box provides computer-controlled power to avoid any damage to the instrumentation from improper power-up sequences over varying cable lengths. Shielded six-conductor cables, up to 500 m long for the sea cable and 150 m long for the solar reference surface cable (both fully loaded with 19-channel sensors and all accessories), are used to provide power and return the data from the instruments to the deck box. A standard C-OPS design has a maximum deployment depth of 150 m. The slow descent speed can result in large horizontal displacements of the profiler if subsurface currents are substantial. When coupled with the offset distance needed to avoid platform perturbations, this means cables significantly longer than 150 m are needed to achieve the maximum deployment depth.

Experience with early free-fall designs (e.g., BioPRO and SuBOPS) revealed that the cable was an important component in stability and other behaviors of the instrumentation during descent. The original in-water (sea) cable was designed with an emphasis on strength and ruggedness. Because the profiling systems were deployed by hand, a red polyester outer braid was used to provide a coarse, but easy to handle, surface texture to provide a grip similar to rope (Table 3).

The diameter of instrumentation cable is controlled by the number of conductors required in the application, the presence of a Kevlar strength member, and a waterproofing and protective polyurethane layer. The PRR-800 (BioPRO) electronic design required power and ground, and also included two individual sets of twisted shielded conductors to accommodate the data stream. The shielding is particularly desirable for the solar reference, because it is frequently mounted in the presence of shipboard communications equipment, which are usually active transmitters. The red color made it significantly easier to see the profiler at a distance from the deployment platform during deployments. For use with SuBOPS, the SubConn Microseries of wet-pluggable connectors replaced all connectors originally used for the instrument and deck box.

The red braided cable was robust and easily gripped, which made it easy to use in a wide variety of conditions. Unfortunately, it was also somewhat stiff, and at times, difficult to manage in the time compressed environment of many field campaigns. A recurring problem was the *memory* of the original winding, which made it cumbersome to coil the cable quickly into a bucket. Although the stiffness of the cable provided a somewhat stabilizing influence on free-fall profilers, from a rudder-like effect, the overall influence on instrument pitch was problematic, and the cable was redesigned for the specific purpose of free-fall deployments.

The new sea cable is a paler shade of red. The design retained the original specifications of the conductors in order to remain compatible with legacy instruments, as well as the Kevlar strength member (Table 3). The individual conductor insulation was changed to polypropylene to support high temperature terminations. Additionally, a water blocking compound was incorporated to provide roundness and prevent water propagation in the event of an outer jacket breach. The red braid was removed entirely and a new, low-density, polyurethane, 0.050 in thick outer jacket provides abrasion resistance and waterproofing.

4.4 Operation

The deployment and operation of the C-OPS instrument is situationally dependent on weight distribution and buoyancy, which is itself contingent upon water density. The initial adjustments control platform orientation (pitch and roll). Subsequent adjustments are used primarily to set the proper buoyancy for the system, which determines the magnitude and depth of the terminal velocity, and pitch adjustments to provide bias offsets for currents and the power-telemetry cable. (The pitch axis is perpendicular to the axis connecting the two light sensors and is in the direction of the cabling harness.)

Preparing a C-OPS instrument for use in the field begins with ensuring that the solar reference is properly sited, i.e., the cosine collector has an unobstructed view of the sky, and is cabled to the deck box. The importance of this part of the deployment procedure is presented in Chap. 8. The steps necessary to prepare the C-OPS in-water instrumentation for deployment are as follows: a) connect the power telemetry cable to the Y-cable on the backplane and attach the strain relief to the harness; b) install the desired number of air bladders within the main buoyancy chamber; c) add the desired amount of weight to the counterpoise at the bottom of the instrument; and d) adjust the distribution of the secondary flotation. The instrument is subsequently placed in the water and the descent and vertical tilt observed.

Weight or buoyancy is adjusted as needed to ensure that the instrument is tuned to be almost neutrally buoyant, but biased slightly negative. At this point, the relationship between the near-surface behavior of the instrument and the ultimate terminal velocity is controlled by the ratio of air flotation to weight. The larger this ratio, the longer the system will tend to loiter near the surface. The greater the additional weight, the faster the terminal velocity of the system at depth. These two factors control the wide range of sampling strategies that can be applied to situations such as use in very shallow coastal water or deep oceanographic stations.

When the buoyancy adjustment is complete, the instrument is allowed to drop 1–3 m below the surface (water depth permitting) and the pitch and roll orientations are noted. Secondary flotation is adjusted laterally as needed to zero the roll values. Usually, it is possible to achieve less than ±0.5° difference from zero in roll, depending on surface conditions. In calm waters, roll adjustment to within 0.1° is normal. Pitch adjustment uses the geometric relationship between the bottom of the V-block mounts and the backplane. Pivot nuts are loosened and the pitch angle is adjusted on the irradiance side of the instrument to a value that cancels the backplane bias measured during the initial deployment. A plastic dial caliper is used to measure the V-block position relative to the backplane, and then the radiance V-block is adjusted to match. This ensures that the two instruments are parallel relative to the backplane.

The entire attitude adjustment process, from attaching the cable to the initial test profiles, lasts approximately 15–30 min (depending on the experience of the operator and the *in situ* environmental conditions). After the initial tuning, the instrument performance is highly robust and rarely needs adjustment unless the density of the water changes significantly (such as moving from a marine to riverine environment, or moving from the open ocean to the marginal ice zone) or the *in situ* current field changes. Currents pose the most significant challenges, but the main point is to ensure good vertical tilts (less than 5°) close to the sea surface (top 1–5 m). Subsurface currents can degrade data quality, but they usually do not significantly degrade the final data products, so the most important adjustments are those influencing the near-surface behavior of the profiler.

The C-OPS (and SuBOPS) instruments are usually deployed from the stern of a research vessel (although bow deployments are also made to avoid the turbulent mixing that occurs at the stern of a boat). The instrument is first lowered into the water, and allowed to drift away from the ship or to have the ship drift away from the instrumentation. The latter is frequently accomplished by the windage on the vessel. If the profiler does not drift away, short, impulsive headway maneuvers (or *bumps*) of approximately 0.5 kts are used to create enough propeller *wash* to push the profiler or boat away. Ships equipped with thrusters can usually maneuver away from the profiler in a variety of orientations.

The objective of the short impulsive maneuvers is to position the profiler well clear of any possible shadows or reflections caused by the deployment platform. In most cases, three vertical profiles (or *casts*) are acquired, so the profiler needs to be even farther away to allow for some loss of distance when the instrument is pulled back to the surface between casts. In most circumstances, if the profiler is initially placed 30–50 m away from the deployment platform, three casts can be executed without any need for significant repositioning.

A cast is executed by simply releasing the telemetry cable and *paying out* cable at a sufficient rate to prevent it from ever coming under tension. Although the harness of a kite-shaped backplane keeps the instrument in a mostly vertical orientation (so it is not subjected to a significant righting event), the release of the tension associated with the cable still results in oscillations, which can be accentuated or dampened by surface waves. Even brief periods of tension can adversely affect the attitude and descent of the profiler. To ensure this does not occur, the operator leaves some slack cable at the surface. Care is taken to not leave too much free cable in the water, because the cable can move under the ship and become entangled in the propeller or stern thruster intake (if present). To ensure a tangle-free and continuous feed of cable into the water, all of the cable (usually 100–300 m) is coiled in a large bucket or laid out on deck prior to each deployment sequence in such a manner as to minimize entanglements.

Once the profiler reaches the desired depth, which is usually set by the 1% light level or the proximity of the sea bottom, the cable is pulled in to bring the profiler to the surface. Because C-OPS behaves like a kite when the cable is under tension, the profiler has a tendency to ascend vertically (or *pop up*) to the surface without moving significantly closer to the deployment platform (depending on environmental conditions). Small bumps by the ship or a C-HOIST unit (Chap. 8) can be used to haul the cable in faster. If a winch is used, care must be taken to ensure the diameter of the drum is sufficiently large to not damage the cable (C-HOIST does not use a drum).

During a cast, the solar irradiance is monitored for constancy to ensure data collection occurs during stable atmospheric conditions. In addition, the vertical tilt of the profiler is continuously checked to make sure the vertical tilts are to within 5°, particularly near the surface. At depth, the terminal velocity is noted and compared to the desired specification. The amount of negative buoyancy determines the descent speed, as well as the ability of the profiler to sink through high shear features, like the thermocline or a subsurface current.

Once data collection activities are completed, the profiler is washed off with fresh water. The optical apertures are dried with a paper tissue by blotting the surfaces; wiping should be avoided because it can cause scratches. If the cable bucket is large enough, the instrument is wrapped in a white cloth to protect it from solar radiation and placed inside the bucket. Both the bucket and the instrument are then properly secured. If severe weather is expected, the cable and instrument should be brought inside for safe keeping.

4.5 C-OPS Evaluation

The field commissioning of the C-OPS instrument was in predominantly mesotrophic (Case-1) waters. The objectives of the field campaign involved more than just an evaluation of C-OPS, which was done on a not-to-interfere basis with the other cruise priorities. In addition, the station work did not permit simultaneous deployment of equipment, so time differences between when one instrument sampled and when the other sampled was on the order of 24–64 min (with an average of 42 min).

The lack of simultaneity in instrument deployments was not considered a significant detraction to the field commissioning exercise, because a) the measurements were being conducted in Case-1 waters with longer space and time scales for homogeneity, and b) the primary purpose was to test the capabilities of the new profiler under realistic conditions with adequate information to make informed decisions about how to proceed with problems should they arise. Because the continuing refinement of the SuBOPS deployment system was the basis for the C-OPS design, the intercomparison was also an evaluation of how well the engineering concepts associated with kite-shaped deployment systems can be adapted to instruments with differing sizes and weights.

The results of the intercomparison of C-OPS and SuBOPS during the field commissioning campaign is presented in Fig. 44 (for the same eight wavelengths presented in Fig. 15, for which six of the wavelengths are common to Fig. 12). The average UPD for each channel between the two profilers ranges from −5.2% to 6.5%, with an overall average of 1.8% (for the wavelengths plotted in Fig. 44), which is to within the calibration uncertainty. A least-squares linear regression of the data (Fig. 44 inset panel) shows almost one-to-one correspondence with over 95% of the variance explained.

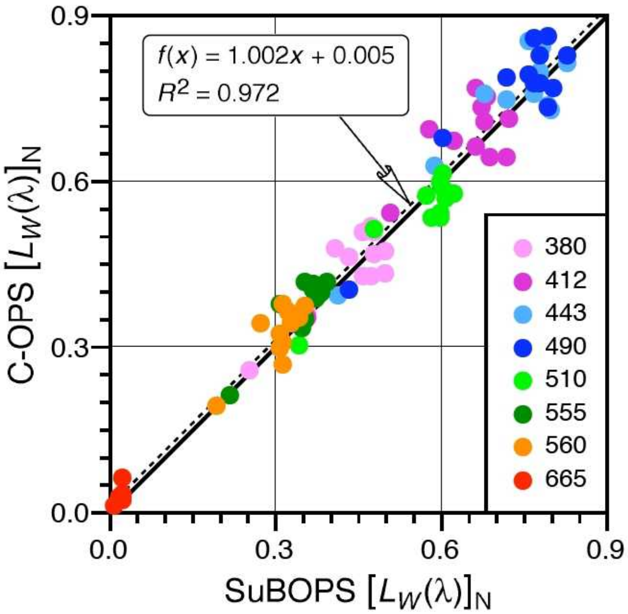

Fig. 44. An intercomparison of the SuBOPS and C-OPS instruments in mostly mesotrophic coastal (Case-1) waters for eight wavelengths, which are given in nanometers. The units for $[L_W(\lambda)]_N$ are $\mu W\,cm^{-2}\,nm^{-1}\,sr^{-1}$. The one-to-one line is shown as solid, and the least-squares linear fit to all the data as dashed (regression information is given in the inset panel).

The larger variance in Fig. 44 with respect to the BioPRO and microNESS intercomparison (Fig. 12), which was also in Case-1 waters, is caused by the greater variability of the site and a larger time difference between the measurements by the two profilers. The increase in environmental variability for the C-OPS and SuBOPS intercomparison was caused by an atypical, and rather rapid, evolution in the near-surface waters (upper few meters of the water column). In some cases, the TChl a concentration was changing by more than 5% in a 45 min time period.

The operational evaluation of C-OPS was in predominantly turbid (Case-2 waters with very short time and space scales for homogeneity (Fig. 45). For this activity, the two profilers have almost exactly the same backplane configuration, buoyancy capabilities, and pitch adjustment mechanisms—the primary difference is the use of microradiometers for C-OPS and the PRR-800 technology for SuBOPS. The level of turbidity is well characterized by the average K_d values: 10.7 at 320 nm, decreasing to 0.78 at 560 nm, and then increasing to 3.3 at 780 nm. For this field campaign, simultaneous measurements were permitted during controlled circumstances (e.g., while the ship was anchored and the sea state was relatively calm), so the difficulties associated with spatial inhomogeneity were somewhat offset by an ability to sample the water masses contemporaneously.

Fig. 45. The C-OPS (left) and SuBOPS profilers (right) deployed simultaneously for operational evaluation. The two instrument systems are shown in a river system with a water depth of approximately 6 m.

Although the C-OPS microradiometers have some design features that are a legacy of the technology used in SuBOPS, the microradiometers are essentially new sensors. Consequently, it is appropriate to consider simpler intercomparisons in the operational testing, like the performance of the solar references. This is doubly attractive in this case, because the instruments were deployed simultaneously, so any differences will be much more closely related to true instrument performance issues rather than environmental factors.

An intercomparison of the SuBOPS and C-OPS solar references during the operational evaluation is shown in Fig. 46 for an expanded set of wavelengths than was used in the previous intercomparisons to show more spectral information, but still containing most of the same wavelengths. The average UPD for each channel between the two radiometers ranges from -2.5 to 3.9%, with an overall average of 1.3% (for the wavelengths plotted in Fig. 46), which is to within the calibration uncertainty. A least-squares linear regression of the data (Fig. 46 inset panel) shows almost one-to-one correspondence with over 95% of the variance explained.

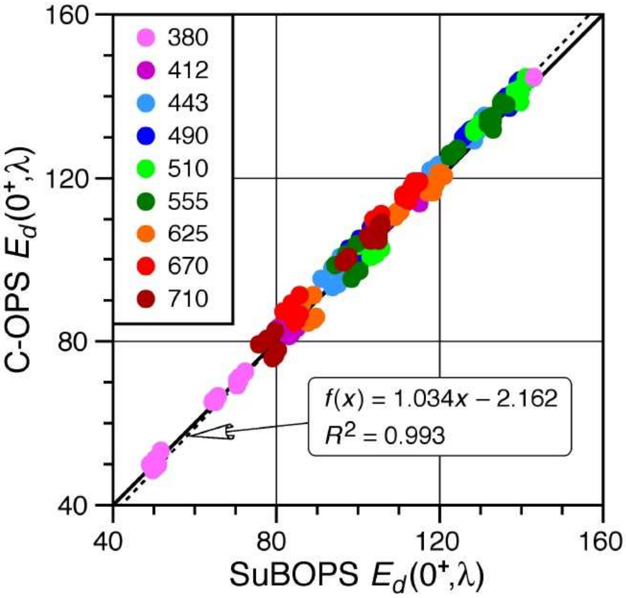

Fig. 46. An intercomparison of the SuBOPS and C-OPS solar references in primarily coastal (Case-2) waters for nine wavelengths given in nanometers. The units for $E_d(0^+)$ are $\mu\mathrm{W\,cm^{-2}\,nm^{-1}}$. The one-to-one line is shown in solid, and the least-squares linear fit to all the data in dashed (regression information is given in the inset panel).

The intercomparison of the in-water sensors for the operational evaluation of C-OPS and SuBOPS is presented in Fig. 47 (for the same wavelengths shown in Fig. 46). Ignoring first the far red and NIR plus the far UV, the average UPD for each channel across the 380–625 nm part of the spectrum ranges from -7.0% to 5.6%, with an overall average of -0.8%, which is to within the calibration uncertainty. Considering now all the wavelengths shown in Fig. 47, the average UPD does not change significantly, it is -0.3%, but the range increases in the red and NIR wavelengths and covers -17.4% to 19.7%. A least-squares linear regression of the data (Fig. 47 inset panel) shows almost one-to-one correspondence with almost 95% of the variance explained.

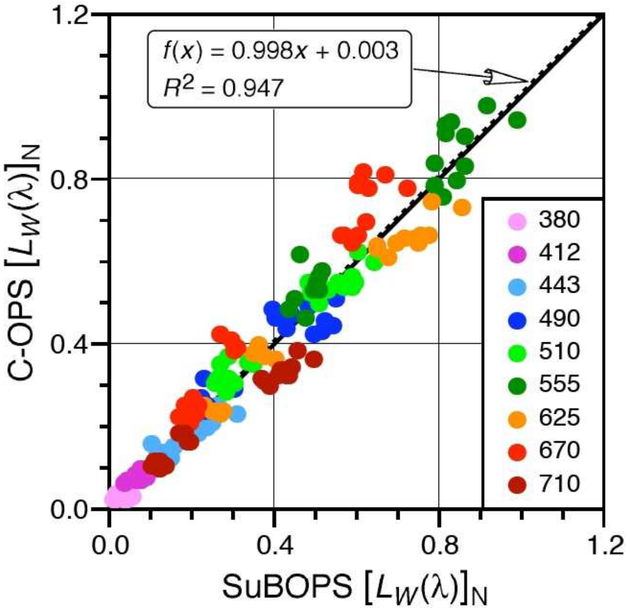

Fig. 47. An intercomparison of the SuBOPS and C-OPS instruments in primarily eutrophic coastal (Case-2) waters for the nine wavelengths in Fig. 46. The units for $[L_W(\lambda)]_N$ are $\mu\mathrm{W\,cm^{-2}\,nm^{-1}\,sr^{-1}}$. The one-to-one line is shown as solid, and the least-squares linear fit to all the data as dashed (regression information is given in the inset panel).

If other wavelengths are considered for the intercomparison, the range continues to increase with the addition of the farthest UV and NIR bands, and reaches −50.7% at 780 nm. The reason for this increase is the aforementioned near-surface layer evolution at the sampling site. Although the two profilers were very similar in their capabilities (e.g., they both had vertical tilts to within 1.5°), the C-OPS profiler loiters at the surface better than SuBOPS, so it collected more data in the area that was changing the most. This translated to the C-OPS extrapolation intervals having almost 70% more data (on average) than SuBOPS. For the highly attenuated wavelengths—the far UV, red, and NIR part of the spectrum—this is a very important difference between the two profilers.

4.6 Advancements and Enhancements

While retaining the features of the hydrobaric chamber, the C-OPS backplane was modified to achieve greater terminal velocities by removing a significant amount of the backplane material (which is heavy). The resulting D-shaped frame also eliminates the counterpoise in favor of a horizontal weight-bearing rod that is not within the field of view of upward irradiance instruments. There is sufficient flat surface normal to typical retrieval forces that the instrument will still kite up to the surface for deployments. Using this arrangement, typical terminal velocities exceed 55 $\mathrm{cm\,s^{-1}}$ below 25 m in deep-water profiles.

Although a standard C-OPS profiler can be configured to measure any two-sensor combination of L_u, E_u, and E_d, a specialized backplane providing simultaneous profiling for all three sensor types is being tested. The new design permits the acquisition of all three principal light field components (Fig. 48), so the Q-factor (E_u/L_u) can be measured simultaneously with E_d. The Q-factor is an important parameter for understanding the bidirectional aspects of the underwater light field. Although $Q(\lambda)$ is well understood for Case-1 waters and can be computed using look-up tables based on the solar geometry and the chlorophyll a concentration (Morel and Gentili 1996), no such capability exists for Case-2 (optically complex) waters.

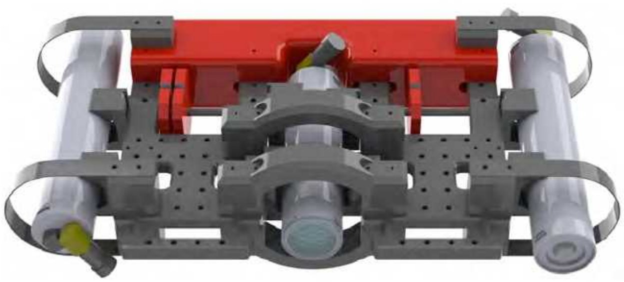

Fig. 48. A schematic of the C-OPS deployment system modified for the simultaneous deployment of three sensors: E_d (left), L_u (center), and E_u (right).

To pursue the goals of simplifying free-fall deployments and removing cable-induced perturbations to profiles, a new sea cable for C-OPS was designed. The objective of the redesign effort was to maximize flexibility and minimize memory via careful selection of jacketing and conductor stranding. Additionally, a half-duplex communication scheme was implemented to allow the removal of one of the twisted pairs used for data telemetry. All internal cable jackets were switched to low-density polyethylene, which is much more flexible than polypropylene; however, this change was made with the tradeoff that heat termination of the cable is no longer supported. The stranding of all conductors was increased to the maximum readily commercially available configurations, which significantly increased the flexibility of the resulting cable. The Kevlar strength member, internal water block, and low-density polyurethane outer jacket were all retained. The outer jacket was thinned slightly to add more flexibility while still providing adequate protection to the internal conductors and a large enough diameter for comfortable handling.

With respect to the entries in Table 3, the following characteristics apply to the new cable:

- *Manufacturer* is Storm Products;
- *Power conductors* are 2×20 AWG with low-density PE insulation;
- *Telemetry conductors* are 2×24 AWG and have low-density PE insulation;
- *Outer diameter* is 0.250 in (nominal);
- *Strength member* is Kevlar (500 lb breaking rating);

Table 4. A comparison of the specifications for the C-OPS (microradiometer) and the BioPRO (PRR-800) profiling systems, with emphasis on the in-water components. The E_s notation denotes a solar reference measuring $E_d(0^+)$. Profiler dimensions do not include the diameter of the sensors. The listed ancillary sensors are in addition to a pressure transducer, which is assumed common to both profiling systems. Profiler dimensions are given as width (W), height (H), and depth (D). The E_s notation denotes an $E_d(0^+)$ sensor.

Specification	*C-OPS*	*BioPRO*
Free-Fall Dynamics	Kite-shaped with hydrobaric buoyancy	Rocket-shaped with buoyant collar
Descent Speed	5–75 $\mathrm{cm\,s^{-1}}$	50–100 $\mathrm{cm\,s^{-1}}$
Sampling Depth	150 m (300 m optional)	350 m
Trim Adjustment	Individual pitch and roll adjustment	Simultaneous pitch and roll adjustment
Vertical Stability	2.5–5.0° (typical)	3.0–7.0° (typical)
Sampling Resolution	1 cm (less than 1 cm in 0–5 m)	4 cm
Photocurrent-to-Voltage Conversion	Electrometer amplifer with three gain stages: 1, 200, and 40,000	Electrometer amplifer with three gain stages: 1, 300, and 100,000
Analog-to-Digital Conversion	24 bit bipolar sigma-delta running at 4–125 Hz	Shared 16 bit ADC with 1, 16, and 256 gain preamp running at 40 kHz
Dynamic Range	9.5 decades (usable)	9.0 decades (usable)
System Data Rate (one and three sensors)	19 channels at greater than 30 Hz and 57 channels at 15 Hz	19 channels at greater than 20 Hz and 57 channels at 15 Hz
Minimum Detectable Signal	Less than 10^{-15} A (0.5 μV ADC resolution)	Less than 10^{-15} A (1.3 μV ADC resolution while on 256 voltage gain)
Spectral Range	250–1,650 nm†	250–875 nm
Sensor Diameter	7.0 cm	10.2 cm
Sensor Length	34 cm (E_d or E_s) and 25 cm (L_u)	55.9 cm (E_d and L_u) and 37.8 cm (E_s)
Sensor Weight	1.7 kg (E_d or E_s) and 1.6 kg (L_u)	4.8 kg (E_d and L_u) and 3.0 kg (E_s)
Profiler Dimensions	48.7 cm W × 36.0 cm H × 8.9 cm D	30.5 cm W ×55.9 cm H × 14.0 cm D
Profiler Weight	6.8 kg in air (E_d and L_u)	5.9 kg in air (E_d and L_u)
Maximum Depth	150 m (300 m available)	350 m (recommended maximum)
Cosine Collector Error	$\pm 3\%$ for $\theta < 60^\circ$; $\pm 5\%$ for $60 \le \theta < 70^\circ$; and $\pm 10\%$ for $70 \le \theta \le 85^\circ$	$\pm 2\%$ for $\theta < 60^\circ$; and $\pm 10\%$ for $60 \le \theta < 85^\circ$
Ancillary Profiler Sensors	Water temperature, pitch and roll, internal pressure, and humidity	Water temperature, and pitch and roll

† 1,100–1,650 nm requires InGaAs detectors.

- *Outer jacket* is red low-density PU;
- *Connectors* are SubConn micro in-line (MCIL6 or MCIL4); and
- *Instrument* is C-OPS.

The new cable is connector and conductor compatible with the old cable. What this means is that all old cables will work fine with systems that have been configured to work with the new cable. They can be used as spares, extensions, or primary deployment cables. The new cable will not work with an old system, however. To convert an *old* system to a *new* system, a switch must be flipped in both the deck box and each light sensor. It is not a difficult process, but it is something that should be done at the factory because of O-ring liability and N_2 purges, etc.

4.7 Summary

The C-OPS instrument successfully integrates a number of new technologies, each focused on different aspects of the practical problem of resolving the optical complexity of the near-shore water column. Structured around 19 high-speed microradiometer optical sensors, C-OPS was specifically designed to be compact enough to deploy from small or large vessels by hand.

The profiling system includes separate sensors to measure vertical profiles of spectral downward irradiance, and upwelling radiance or irradiance using a unique, variable-descent, free-fall backplane. A comparison of C-OPS with the legacy BioPRO (PRR-800) profiler is presented in Table 4.

The system is capable of deployments in fresh and marine waters, in depths ranging from 2–150 m. A multichamber, hydrobaric buoyancy system provides very slow initial descent rates with ultimate terminal velocities of 5–75 $\mathrm{cm\,s^{-1}}$, with a typical attitude control to within approximately 2.5° from vertical. Sample speeds of 15 Hz covering more than nine decades of dynamic range ensure that a representative sample is collected even in the shallowest of waters. Unlike earlier versions, the newest counterpoise design uses naval brass weights mounted inboard of the frame, eliminating any potential intrusion into the nadir field-of-view.

Surface loitering, faster terminal velocity at depth, and high data rates result in sufficient sampling to investigate optically diverse, near-surface thin layers, or produce statistically relevant data sets on surface effects. Direct benefits of this new sampling capability include lower uncertainties in the data products across the full dynamic range of the sampling problem set; better accuracy in separating the living and nonliving components of seawater; and an improved understanding of the interaction between the ocean and atmosphere.

The underlying microradiometer technology is notably more compact and more easily expanded than legacy systems (Fig. 49), ensuring a cost-effective expansion path for both AOP profiling instruments and novel systems occupying new roles in the future. The C-OPS technology is an important initial step toward supporting a coupled ocean–atmosphere observing system (i.e., a calibration and validation capability for a combined satellite mission). A mission such as this will likely highlight coastal and open-ocean processes, placing renewed emphasis on making high-quality measurements with equal efficacy in both the near-shore and open-ocean environments.

Fig. 49. Three generations of AOP profilers, which were deployed during one of the Bermuda Atlantic Time Series (BATS) cruises in 2009 (left to right, respectively): Natasha McDonald holding a MicroPro, which was based on the microNESS instrument; Stanford Hooker holding the first C-OPS unit; and Vincenzo Vellucci holding an SPMR. A second SPMR is on deck in the foreground at left.

Chapter 5

Biospherical Shadowband Accessory for Diffuse Irradiance (BioSHADE): A Marine Shadowband and GPS Accessory

Germar Bernhard, Charles R. Booth, and John H. Morrow
Biospherical Instruments Inc.
San Diego, California

Stanford B. Hooker
NASA Goddard Space Flight Center
Greenbelt, Maryland

Abstract

BioSHADE is an accessory for shipboard radiometers that is used to measure the optical properties of the atmosphere while providing the usual global irradiance measurement of a solar reference. It meets the need for improving the self-shading correction applied to in-water AOP measurements, wherein atmospheric complexity makes it more difficult to properly model the diffuse irradiance. It also provides for the capability of several atmospheric data products that are useful to the atmospheric correction part of calibration and validation activities. BioSHADE integrates seamlessly into instrument systems based on the microradiometer architecture, although it can be configured for use with the PRR-800 series of solar references or other irradiance sensors with the same form factor. It is composed of the following components: a) the stepping motor and controller unit housing an Mdrive 17 from IMS Systems, b) a data aggregator derived from the microradiometer product line, c) a power regulation subsystem, d) the housing for the electromechanical components, e) the shadowband subassembly, and f) the radiometer mounting components. The BioGPS is a 12-satellite GPS receiver designed to be operated simultaneously with radiometric instruments. The system can be fully integrated with instrumentation based on the microradiometer architecture, wherein the GPS is operated over a single cable, linking radiometers, and the BioSHADE accessory with the BioGPS. The latter ensures the accessory components and the radiometric sensors can be operated using standard cabling and deck box configurations.

5.1 Introduction

BioSHADE is an accessory for shipboard radiometers that attaches to a solar reference. It is used to measure the optical properties of the atmosphere as part of a separate data acquisition sequence. BioSHADE meets the need for improving the self-shading correction applied in coastal waters wherein atmospheric complexity makes it more difficult to properly model the diffuse irradiance. It was designed to be used during the time period when a free-fall profiler is being hauled up to the surface. This normally takes only a few minutes (depending on water depth and environmental conditions), so the design parameters established for making the shadowband measurement were based on a 90 s acquisition event. When not being used, the solar reference is able to make an uncontaminated global irradiance measurement.

A GPS can provide vital cruise track and time-of-event records for post-processing optical data collected aboard ship. The U.S. GPS consists of a constellation of medium Earth-orbit satellites operated by the Department of Defense, but having public access. Each satellite in the constellation continually transmits a microwave stream containing time and position information. After locking onto multiple satellites, a GPS receiver converts small differences in the arrival times of these transmissions into a calculated position on the ground. The accuracy and precision of the resulting geographic coordinates usually satisfies most oceanographic sampling requirements.

BioGPS is a 12-satellite GPS receiver designed to be operated simultaneously with BSI radiometric instruments. The system can be fully integrated with optical instruments based on the MMS architecture, wherein the GPS is operated over a single cable linking radiometers and the BioSHADE accessory with the BioGPS. When PRR systems, such as BioSORS, are deployed, BioGPS is used in a stand-alone configuration, remotely delivering data to a logging computer via an independent cable.

5.2 Description

BioSHADE is composed of several components: a) the stepping motor and controller unit housing an Mdrive 17 from IMS Systems, b) a data aggregator derived from the BSI microradiometer product line, c) a power regulation subsystem, d) the housing for the electromechanical components, e) the shadowband subassembly, and f) the radiometer mounting components. The motor is controlled by an aggregator, which is a microprocessor-controlled module also derived from the BSI microradiometer product line. The aggregator allows seamless integration of the BioSHADE accessory into a network of sensors built with this technology. The power regulation subsystem provides the needed optimum power to the motor (12.2 V) and the aggregator (6.4 V), as well as power (6.4 V) to other microradiometer and BioGPS systems. The mounting system is currently based on 1 in national pipe tapered (NPT) type 316 stainless steel (SS) pipe and fittings, although alternative mounting configurations are possible.

The BioGPS combines a high sensitivity GPS microcontroller with a microradiometer aggregator module. The aggregator allows the data stream from the GPS module to be integrated into any system conforming to the MMS architecture, e.g., from a multichannel solar irradiance sensor. The aggregator has two communications ports, one for upstream communications to the deck box and subsequently, the data acquisition computer, and the other for downstream communications.

5.3 Design

The design of the BioSHADE accessory is optimized for 19-channel microradiometer solar references operated in a shipboard environment. The use of a shadowband on a ship requires a different optical design than for terrestrial shadowband photometers. Most notably, it is not possible to position a partial shadowband in accordance with a fixed geographic location, because the heading of the ship is usually not constant, nor is the vertical orientation (pitch and roll) of the device. The dimensions and geometry of the shadowband assembly, therefore, are constrained by the following requirements:

- When the centers of the Sun, shadowband, and diffuser align, the cosine collector must be completely shaded from all parts of the solar disk.
- Because the shadowband is moving at a constant speed, the size of the shadow should be sufficiently large such that the diffuser is shaded for at least seven sample points. (It was determined that this number of sample points is sufficient to ascertain unambiguously that the shading of the Sun is complete.)
- The width of the shadowband should be as small as possible to minimize the area of the sky that is shaded. This requirement helps reduce the uncertainties involved in calculating the direct irradiance component of the global irradiance.
- For practical reasons, the diameter of the shadowband should not be larger than 10 in (25 cm).
- A 180° swath of the shadowband should be completed in approximately 60 s ($3^\circ\,\mathrm{s}^{-1}$ rotation rate), which when coupled with the rest of the command set, should result in a total data acquisition scenario of about 90 s.
- The shadowband should be out of the FOV of the cosine collector when moved to its lowest position for accurately measuring the global irradiance.

Using these requirements, the nominal inside diameter of the band is 8.56 in.

The band is made out of 0.06 in (1.5 mm) thick aluminum that is 1.0 in (2.5 cm) wide and anodized black. The size of the main housing is 3.5 in (8.9 cm) in diameter and 10.5 in (26.7 cm) long. A depiction of the BioSHADE accessory in operation with a microradiometer solar reference and BioGPS unit is shown in Fig. 50.

Fig. 50. A shadowband assembly schematic with a 19-channel microradiometer solar reference in the left foreground, the motor housing with supporting electronics at the right, and an optional BioGPS unit at the left rear. The narrow cylinder at center is the mounting post (1 in NPT 316SS pipe).

The minimum width of the shadowband is constrained by the size of the cosine collector, which is 0.885 in (2.25 cm) in diameter for BioSORS and C-OPS. Because the angular size of the solar disk is about 0.54°, the shadowband must be slightly wider. The requirement that the diffuser should be shaded for at least seven sample points further increases the width.

Based on these considerations, the following dimensions were chosen: the shadowband is 1.00 in (2.54 cm) wide. The distance from the collector to the band depends on the orientation of the band. It varies from 3.78 in (9.60 cm) to 4.28 in (10.87 cm), because the pivot point is 0.5 in (1.27 cm) below the plane of the irradiance collector (also referred to as the *horizon*) to satisfy the last requirement above. When the band is in the zenith, it shades a 15°-wide segment of the sky. In the normal mode, the radiometer is sampling at a rate of 15 Hz. The measurement of seven sample points, therefore, requires 0.47 s during which the shadowband moves 1.2°.

The BioSHADE motor is a size 17 stepper motor with 51,200-step resolution, which is coupled to the shadowband with a flexible coupling (Fig. 51). The system has an expected range of motion of approximately 220°. The motor is equipped with a home sensor used in initial setup. Motor power is switched and provisions are made to measure internal voltage and current to allow automatic compensation for variable cable lengths and the resulting uncertainty of voltage drops. The supply voltage ranges from 12.75–16.00 VDC depending on the configuration and length of the cable. The system consumes up to 440 mA when fully configured with the actual voltage required. Most cases can be handled with a specification of 1 A.

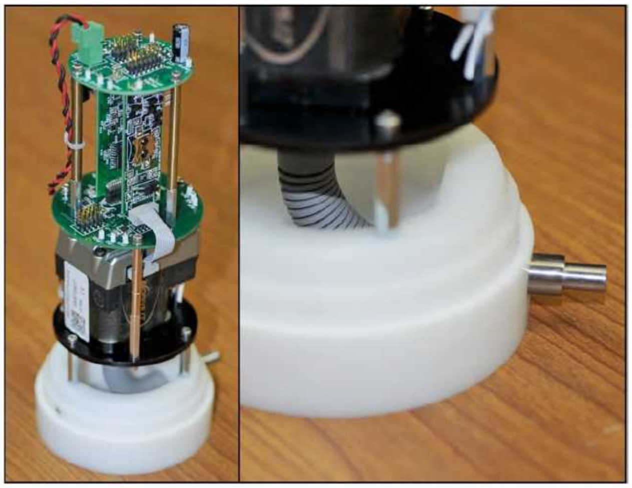

Fig. 51. The BioSHADE drive components (left), with the stepper motor above the white end cap; above the motor is the aggregator (vertically oriented green circuit board), which serves as the motor controller and electronic interface. A magnified view (right) shows the coupler in more detail. The unit is upside down in both panels.

To keep the shadowband at or below the horizon when stowed, the band needs space to rotate below the plane of the cosine collector. For the stowed angle below the horizon to be reasonably large (e.g., 40°), the clearance of the band with respect to the solar reference must be reasonably large. The needed clearance produces an eccentricity in the geometry of the band with respect to the sensor, which is shown in Fig. 52. Not shown in the figure, but used in the formulation of data products produced from the shadowband measurements, is the shadowband angle, υ, which is defined as the angle between the horizontal plane of rotation and the direction of the shadowband (measured from the zero position, which is described below).

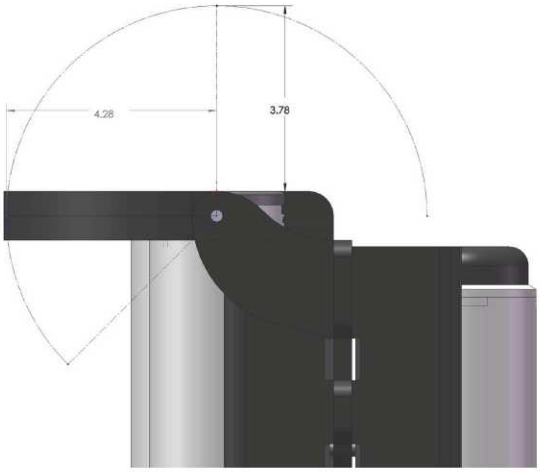

Fig. 52. A side-view illustration of the C-OPS solar reference with the BioSHADE, showing the distance between the shadowband and the diffuser for vertical and horizontal orientation of the shadowband. The BioSHADE housing is behind the solar reference (left) and the BioGPS is to the right.

5.4 GPS Operation

BioGPS can be used by itself or as part of more complicated systems, which need not be MMS instruments, although cabling and data acquisition is simplified when it is used as part of a microradiometer system. Five different modes of operation are available:

1. Fully integrated microradiometer system with a synchronized shadowband and GPS data stream controlled MMS deck box;
2. Automated shadowband movement and GPS reporting controlled by an MMS deck box;
3. Manual shadowband movement and GPS reporting controlled by a data acquisition computer;
4. Streaming GPS reporting using ASCII data; and
5. Polled GPS reporting using ASCII data.

The GPS data stream provides the following parameters: a) Universal Time Coordinated (UTC) to the nearest second, b) longitude, c) latitude, and d) the number of satellites visible. In the event that a GPS fix is invalid, `-999` is reported for each parameter.

Because the MMS architecture requires synchronized data streams at rates exceeding 12 Hz, the response times of individual sensors are critical. In contrast, the GPS engine used in BioGPS typically updates its position once per second. This slow refresh rate has implications in the way the data is buffered by the BioGPS aggregator.

The BioGPS aggregator controls the sampling of the GPS, and also responds to polled requests for data from the controlling deck box. The service time of the requests is typically less than 10 ms to maintain a 15 Hz polled data stream from multiple radiometers, and other devices such as a shadowband. This need for very short lag times means that querying the GPS and then waiting for a response would greatly slow down the system. Consequently, the GPS data stream is serviced by interrupts, because the desired sample rate (nominally 15 Hz or 67 ms per frame) is too short to request and receive data in many instances. The best-case turnaround time period is approximately 35 ms, with many lasting 100 ms or longer, which is too long to wait for a reply without disturbing the sample rate.

The data volume of MMSs can be substantial. For example, three 19-channel radiometers are projected to have 332 bytes transmitted in each data frame (104 bytes per sensor plus about 20 bytes from the deck box). At 15 Hz, this is 4,980 bytes per second, or for a system running continuously, 480 MB per day. Although many radiometric systems have intermittent duty cycles (e.g., C-OPS), others will have more frequent sampling scenarios (e.g., OSPREy), so data volume can be an important problem.

The GPS data stream conforms to the National Marine Electronics Association (NMEA) data format, which is an ASCII string of up to 80 characters. The BioGPS command structure allows the full ASCII data stream to be retrieved. To minimize the flow of redundant data, however, the NMEA string can optionally be converted to short precision (4-byte) floating point numbers. Because fresh GPS data is only available every second, the data stream can be multiplexed, with the parameter actually transmitted being rotated through the four types of parameters (time, longitude, latitude, and number of satellites). This feature further reduces the amount of data to be transmitted.

5.5 Shadowband Operation

The precise position of the shadowband is unknown when the controller unit is powered up. When under the automatic control with a C-OPS deck box, the motor is turned on and initialized at startup. First, the motor is moved counterclockwise (CCW) approximately 20°, then back and forth 15° while deck box power levels are adjusted to compensate for any voltage drop in long cables.

The second part of the initialization sequence, which is issued by the data acquisition software, involves the following command sequences:

1. `Read` the motor position.
2. `Move` negative 12,000 steps from the current read position. This move ensures that the shadowband will find the home position in Step 3, regardless of its initial position. On some occasions, the shadowband may run into stops that are integral to the device's mounting brackets, causing the motor to slip (which is acceptable).
3. `Move` into the home position (this is always in the clockwise, CW, direction).
4. `Move` to the 0 (zero) position in the negative direction (CCW), approximately 30,000 steps. The exact value is the motor *offset* and will vary from unit to unit depending on the location of the home position.
5. `Set` this position to 0. This should have the band horizontal and even with the top of the irradiance collector.
6. `Move` the shadowband from 0–180° (which is the aforementioned υ angle), with farther extension to a typical value of 220°, where the band is completely below the horizon. This latter position is also the *stowed* position when not in use.
7. `Move` the shadowband back to 0°; repeat Steps 6 and 7 as long as desired.

Extension of the motion cycle as part of the sixth step also provides an extended period of time with the band out of the field of view of the collector, so the data acquisition sequence ends with a global irradiance measurement. If the shadowband data is collected immediately after a C-OPS down cast, the global irradiances from the two events can be used to verify atmospheric stability across the measurement sequences. A sequential movement of the shadowband over the C-OPS solar reference during clear-sky conditions is shown in Fig. 53.

5.6 Shadowband Modeling and Testing

In the following discussion, BioSHADE was operated with a 19-channel C-OPS solar reference radiometer on the roof calibration facility at BSI. Weather conditions were ideal during the test period, offering several cloudless days with low aerosol loading. This analysis focuses on measurements taken on 7 October 2008, one of the clearest days of the test period.

Figure 54 shows solar reference measurements during a full cycle of shadowband irradiance at 320 nm (blue data set, right axis) and 780 nm (red data set, left axis) measured on 7 October 2008 between 17:52 and 17:56 UT. During this period, the solar zenith angle (SZA) was about 45.5°. Vertical lines indicate times when the motion of the shadowband reversed. The band is in its maximum position at points G_1 and G_3, and in the zero position at point G_2. As the band moves upward from point G_1, it will eventually be horizontal (point A_1). From this position onward, a portion of the sky will be shaded and the irradiance measured by the microradiometer will decrease. The change in signal is much larger at 320 nm than 780 nm, because sky radiance is much greater at shorter wavelengths (at 780 nm, the predominant portion of the signal is due to direct sunlight).

Fig. 53. A sequential movement of the shadowband over the C-OPS solar reference (center white cylinder) on a clear-sky day. The shadowband controller is the right-most cylinder, and the GPS is the left-most. The solar reference is slightly above the other two devices to ensure an unobstructed view of the sky. The primary cable connection is to the controller; the other devices plug into the controller to receive power and send data. The black cylinder between the BioGPS and the solar reference is a solar reference for another instrument system.

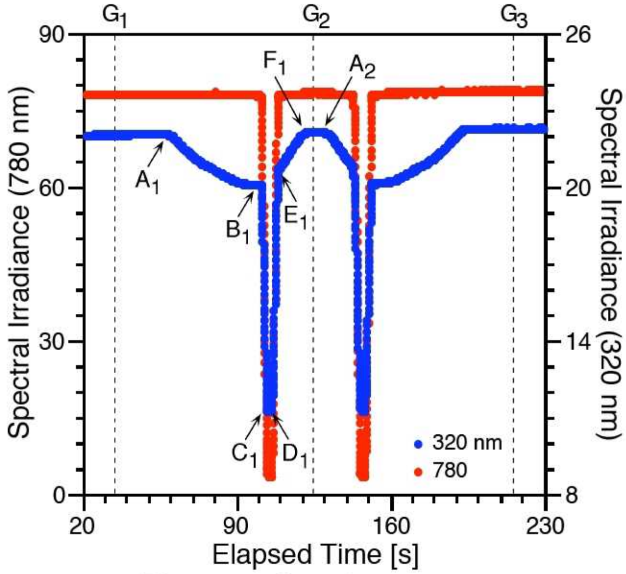

Fig. 54. The spectral irradiance measurement at 320 and 780 nm using the prototype BioSHADE accessory and the C-OPS solar reference. The data were acquired on 7 October 2008 between 1752 and 1756 UTC. Vertical lines indicate times when the motion of the shadowband reversed. Labeled points are explained in the text.

The collector of the solar reference is cosine weighted and the effect of shading the sky increases as the band moves from the horizon toward the zenith. At point B_1 in Fig. 54, the band starts to block the direct component of the solar illumination, and the irradiance rapidly decreases until the entire cosine collector is shaded (point C_1). At point D_1, the band is no longer fully occluding the diffuser and direct sunlight begins to fall on a portion of the collector, so the irradiance increases. There is very little change in irradiance between points C_1 and D_1, because the width of the band is set to ensure a reasonable number of totally occluded data points are acquired. At point F_1, the band is horizontal and the instrument once again measures global irradiance. The time required for the band to move between points A_1 and F_1, which represents a full 180° swath, is 64 s.

5.6.1 Direct Irradiance Calculation

The main purpose of the BioSHADE accessory is to provide measurements of the optical properties of the atmosphere and, in particular, to allow the calculation of the direct-horizontal spectral irradiance (i.e., the irradiance on a horizontal plane from direct solar illumination), $E_b(0^+,\lambda,t)$. The calculation requires a variety of irradiance measurements made before, during, and after the passage of the shadowband over the cosine collector on the solar reference.

To calculate $E_b(0^+,\lambda,t)$, the solar zenith angle (θ) plus the following defined quantities are needed:

$E_n(0^+,\lambda,t)$	The direct-normal spectral irradiance (irradiance on a plane perpendicular to the detector–Sun direction).
$E_i(0^+,\lambda,t)$	The diffuse spectral irradiance (irradiance from the sky on a horizontal plane).
$E_d(0^+,\lambda,t)$	The global spectral irradiance (irradiance from the Sun and sky on a horizontal plane).
$E_k(0^+,\lambda,t_\upsilon)$	The hypothetical (i.e., it is not measured directly) spectral irradiance at the solar reference for the segment of the sky that is shaded by the shadowband at time t_υ when the band is at shadowband angle υ.
$E_p(0^+,\lambda,t_\upsilon)$	The spectral irradiance at the solar reference when the band is at shadowband angle υ and not blocking direct sunlight.
$E_a(0^+,\lambda,t_\upsilon)$	The spectral irradiance at the solar reference when the centers of the solar disk, shadowband, and diffuser are aligned and direct sunlight is completely occluded.
$c_b(\lambda)$	The angular response error of the solar reference, defined as the ratio of angular response at incidence angle ϑ to $\cos(\vartheta)$.

$c_i(\lambda)$ The angular response error of the solar reference when exposed to isotropic radiation.

$c_d(\lambda)$ The angular response error of the solar reference when measuring global irradiance.

From these definitions, the following equations can be derived from inspection:

$$E_n(0^+,\lambda,t) = \frac{E_b(0^+,\lambda,t)}{\cos(\theta)}, \tag{6}$$

$$E_p(0^+,\lambda,t_v) = E_d(0^+,\lambda,t_v) - E_k(0^+,\lambda,t_v), \tag{7}$$

and

$$\begin{aligned} E_a(0^+,\lambda,t_v) &= E_d(0^+,\lambda,t_v) - E_k(0^+,\lambda,t_v) \\ &\quad - E_b(0^+,\lambda,t). \end{aligned} \tag{8}$$

The six quantities $E_d(0^+,\lambda,t)$, $E_b(0^+,\lambda,t)$, $E_n(0^+,\lambda,t)$, $E_i(0^+,\lambda,t)$, $E_k(0^+,\lambda,t_v)$, $E_p(0^+,\lambda,t_v)$, and $E_a(0^+,\lambda,t_v)$ cannot be measured directly by the solar reference, because the solar reference is affected by a small angular response error (or *cosine error*). Quantities affected by this error are indicated by the prime symbol ($'$). For example, if the shadowband is below the horizon, the signal of the solar reference is proportional to $E'_d(0^+,\lambda,t) = c_G(\lambda)E_d(0^+,\lambda,t)$.

From (7) and (8), and the definition of $c_b(\lambda)$, it can be concluded that $E'_b(0^+,\lambda,t_M) = c_b(\lambda)E_b(0^+,\lambda,t_M) = E'_p(0^+,\lambda,t_M) - E'_a(0^+,\lambda,t_M)$, where t_M indicates the time when the centers of the Sun, shadowband, and collector are all aligned. This leads to the expression for the calculation of $E_b(0^+,\lambda,t_M)$:

$$E_b(0^+,\lambda,t_M) = \frac{E'_p(0^+,\lambda,t_M) - E'_a(0^+,\lambda,t_M)}{c_b(\lambda)}. \tag{9}$$

The challenge is that $E'_p(0^+,\lambda,t_M)$ is not directly accessible from the measurements acquired with the shadowband accessory, but must be extrapolated from observations taken at times when all parts of the collector are exposed to direct sunlight. (These are times to the left of point B_1 or to the right of point E_1 in Fig. 54).

To determine $E'_p(0^+,\lambda,t_M)$, an analysis software package was developed based on the formulation presented in (9). The software also determines performance metrics of the shadowband system, so the quality of the results can also be assessed. The software procedure that was developed is illustrated graphically in Fig. 55, which also indicates the relative change of the measured irradiance from one sample point to the next. This quantity is used to determine the times when the shadowband starts to shade the cosine collector from the direct illumination of sunlight (points B and E), and when the occlusion is at the maximum (point M).

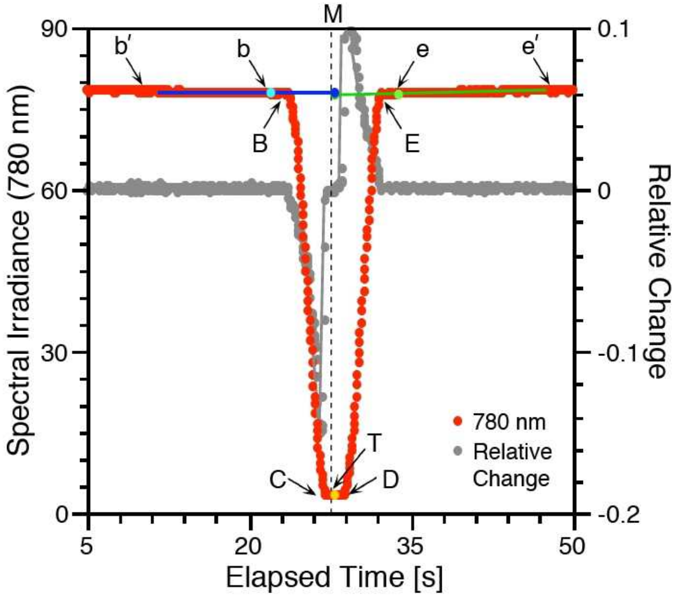

Fig. 55. A portion of the spectral irradiance at 780 nm from Fig. 54. The time M indicates when the centers of the Sun, shadowband, and collector were in line (as determined with the analysis software), and T is the intersection of the dashed line with spectral irradiance at 780 nm. The other points and the fitted lines are explained in the text.

A graphical depiction of the determination process for the $E'_p(0^+,\lambda,t_M)$ parameter is shown in Fig. 55. The $E'_p(0^+,\lambda,t_M)$ value (the blue circle on M near the top of the plot), is extrapolated via a linear regression using all measurements between points b′ and b. Additionally, $E'_p(0^+,\lambda,t_M)$ was extrapolated from measurements between points e and e′, as shown by the green circle, just below the blue circle, on M. The difference between the two extrapolated values, denoted $E'_{p_B}(0^+,\lambda,t_M)$ and $E'_{p_E}(0^+,\lambda,t_M)$, respectively, is a measure of the uncertainty for calculating $E'_p(0^+,\lambda,t_M)$ and presents the principal limitation of any shadowband approach for measuring $E_b(0^+,\lambda,t)$. As Fig. 55 indicates, the difference between $E'_{p_B}(0^+,\lambda,t_M)$ and $E'_{p_E}(0^+,\lambda,t_M)$ is rather small. The difference tends to be larger at shorter wavelengths, however, because of the larger values of $E_k(0^+,\lambda,t_v)$ and their dependence on the band position.

The variation of $E'_{p_B}(0^+,\lambda,t_M)$ and $E'_{p_E}(0^+,\lambda,t_M)$ at $\lambda = 780$ nm was investigated for several consecutive shading events during stable atmospheric conditions. The relative difference was on the order of 0.2%. The average of the two values exhibited little *noise*, from one event to the next. Consequently, this value was used for the calculations of $E_b(0^+,\lambda,t)$ presented below. A similar analysis was performed for $\lambda = 320$ nm, for which the relative difference was typically 1.5%, but the average of the two extrapolated values varied by less than 0.3% from one shading event to the next. This suggests $E'_p(0^+,\lambda,t_M)$ can be calculated from all spectral channels with high accuracy.

5.6.2 Shaded Irradiance

The accurate determination of the $E_a'(0^+,\lambda,t_M)$ parameter is also required for the calculation of $E_b(0^+,\lambda,t)$. The value $E_a'(0^+,\lambda,t_M)$ is defined here as the average of all sample points between points C and D, where the relative point-to-point change is less than 0.2% (see Fig. 55 for the definition of points C and D). The number of points contributing to this average is shown in Fig. 56 for measurements on 7 October 2008 performed for SZA values from 33–85°. The number of points increases with SZA. This can be explained as follows: the axis of the shadowband was approximately oriented in the East–West direction. At a large SZA (or close to sunrise and sunset), the Sun is either in the East or West. In this case, the angular movement of the band across the disk of the Sun is slower than when the axis is perpendicular to the line of the collector and Sun, explaining the large number of sample points contributing to $E_a'(0^+,\lambda,t_M)$.

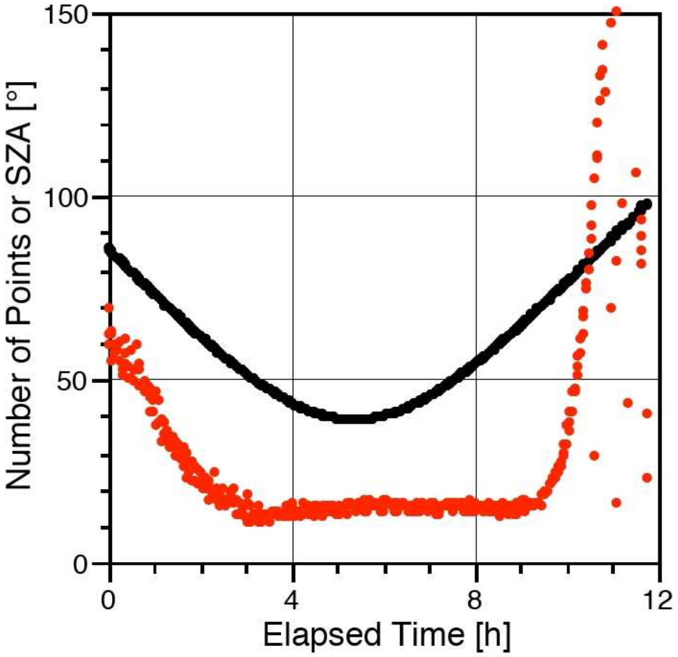

Fig. 56. The number of data points (red) contributing to the $E_a'(0^+,\lambda,t_M)$ values as a function of SZA (black). The two parameters share the same axis, but with different units.

The ability of the system to determine $E_a'(0^+,\lambda,t_M)$ with high confidence was estimated by analyzing a time series of $E_a'(0^+,\lambda,t_M)$ over several shading events (results are presented in Fig. 57). At 320 nm, there is virtually no event-to-event variation beyond the upward slope resulting from the decrease of SZA during the evaluation period. At 780 nm there is some variation, which is likely partly due to real changes of the atmosphere (e.g., change in aerosol loading); however, the event-to-event variation at this wavelength is also smaller than 0.7%.

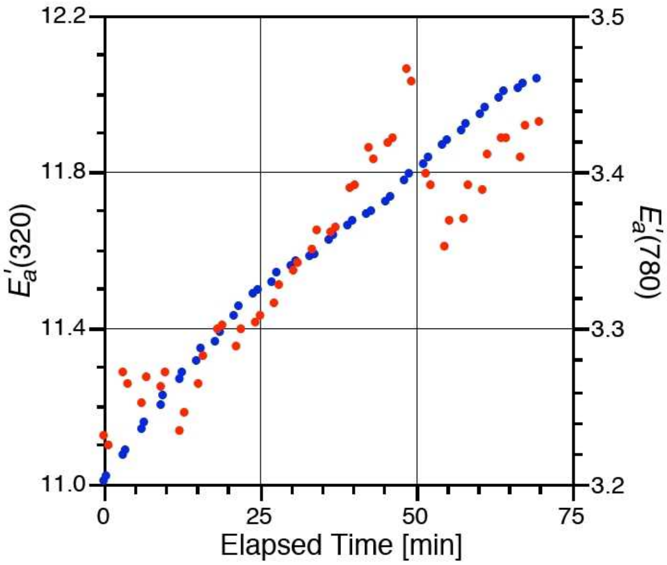

Fig. 57. Measurements of $E_a'(0^+,\lambda,t_M)$ at 780 and 320 nm (red and blue, respectively).

Figure 58 shows the diurnal cycle of $E_a'(0^+,\lambda,t_M)$ for all 19 wavelengths of BioSHADE. There is some asymmetry, with lower values generally in the morning, indicating that the atmosphere's aerosol loading has changed over the course of the day. The largest spectral irradiance is observed at 412 nm. Measurements at wavelengths larger than 600 nm are comparatively low because the largest contribution stems from direct irradiance, which is blocked.

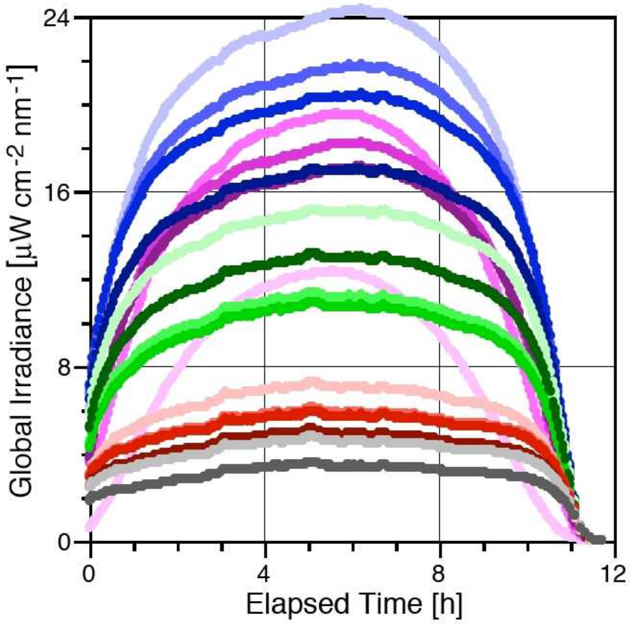

Fig. 58. Measurements of $E_a'(0^+,\lambda,t_M)$ using the following gradient (respectively): light-to-dark violet 320, 340, 380, 395 nm; light-to-dark blue 412, 443, 465, and 490 nm; light-to-dark green 510, 532, 555, and 560 nm; light-to-dark red 625, 665, 670, and 683 nm; and light and dark gray 710 and 780 nm.

5.6.3 Direct Normal Irradiance

Figure 59 shows the diurnal variation of direct-normal irradiance $E_n(0^+, \lambda, t_M)$ calculated using (6). Data are not perfectly symmetrical about the solar noon, most probably due to changes in aerosol loading over the course of the day. There is a "hump" in data measured at SZA larger than 80° at wavelengths larger than 600 nm. This feature is likely related to an incomplete correction of the system's cosine error. (At the time of this analysis, a detailed cosine correction of the instrument was not yet available; the cosine correction used was based on a generic function for microradiometers, which may not be appropriate for this particular instrument at long wavelengths.)

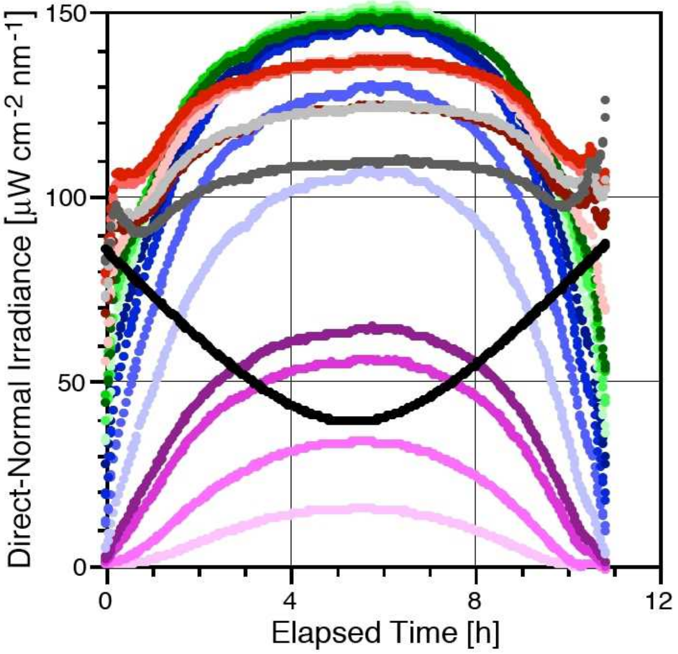

Fig. 59. Spectral direct-normal irradiance for 7 October 2008. The SZA is shown in black using the y-axis numerical values, but in degrees.

5.6.4 Global Irradiance

Figure 60 shows the diurnal variation of cosine-error corrected global irradiance, $E_d(0^+, \lambda, t)$, measured at times associated with points G_1, G_2, and G_3 (Fig. 54 defines the latter three points). The value $E_d(0^+, \lambda, t)$ was calculated from uncorrected global irradiance data $E'_d(0^+, \lambda, t)$ using the following formulation:

$$E_d(0^+, \lambda, t) = \Big[E'_d(0^+, \lambda, t) - c_b E_b(0^+, \lambda, t) + c_i E_b(0^+, \lambda, t)\Big] c_i^{-1}, \quad (10)$$

where the angular response error terms are from Sect. 5.6.1. Values of $E_b(0^+, \lambda, t)$ in (10) were interpolated from $E_b(0^+, \lambda, t_M)$ to the times associated with points G_i.

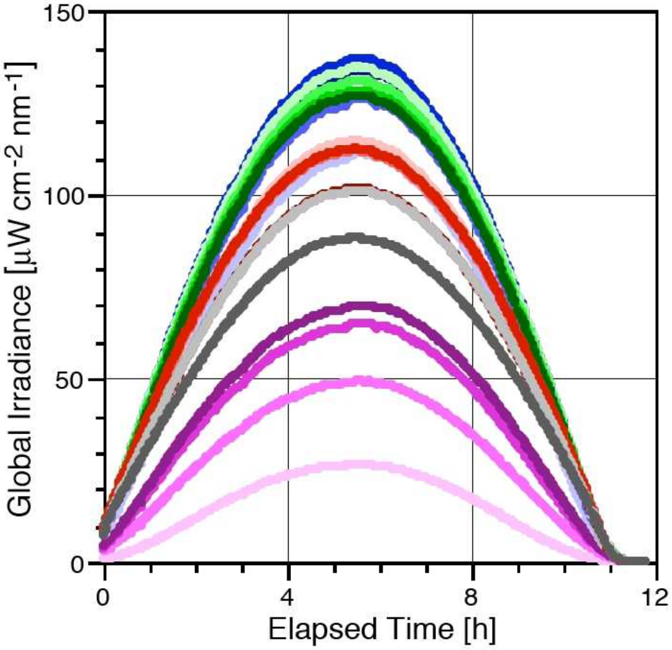

Fig. 60. Spectral global irradiance $E_d(0^+, \lambda, t)$ for 7 October 2008. A cosine-error correction was applied.

5.6.5 Langley Plots

The change of direct-normal irradiance with SZA is determined by the Beer–Lambert's law:

$$E_n(0^+, \lambda, t) = E_0(\lambda, t) \exp^{-\tau(\lambda) m(\theta)}, \quad (11)$$

where $E_0(\lambda, t)$ is the direct-normal irradiance outside Earth's atmosphere, $\tau(\lambda)$ is the spectral optical depths of all scatters and absorbers in the atmosphere, and $m(\theta)$ is the relative optical airmass, which is a function of SZA and can be approximated with:

$$m(\theta) = \left[\cos(\theta) + 0.50572\,(96.07995 - \theta)^{-1.6364}\right]^{-1}. \quad (12)$$

Taking the logarithm of (11) leads to:

$$\ln[E_n(0^+, \lambda, t)] = \ln[E_0(\lambda, t)] - \tau(\lambda) m(\theta). \quad (13)$$

If $\tau(\lambda)$ does not change over the course of the day, $\ln[E_n(0^+, \lambda, t)]$ becomes a linear function of $m(\theta)$. Plotting measured data of $\ln[E_n(0^+, \lambda, t)]$ versus $m(\theta)$ allows for the determination of $E_0(\lambda, t)$ by extrapolation to $m(\theta) = 0$, and to estimate $\tau(\lambda)$. The optical depth $\tau(\lambda)$ is the sum of the Rayleigh optical depth $\tau_R(\lambda)$, aerosol optical depth $\tau_A(\lambda)$, and the optical depth $\tau_X(\lambda)$ of other scatterers and absorbers. By calculating $\tau_R(\lambda)$ and $\tau_X(\lambda)$, the aerosol optical depth $\tau_A(\lambda)$ can be determined. Plots of $E_n(0^+, \lambda, t)$ versus $m(\theta)$ are known as Langley plots.

Langley plots from irradiance data collected with the BioSHADE accessory were used to determine the potential for deriving $E_0(\lambda, t)$ and $\tau_A(\lambda)$. A Langley plot for data measured on 7 October 2008 is presented in Fig. 61, which shows $\ln[E_n(0^+,\lambda,t)]$ varies fairly linearly with airmass $m(\theta)$ for $m(\theta) < 3$ (where θ is less than 70°) with similar values in the morning and afternoon, as expected. For an airmass between 3–8 (where θ is between 70° and 82°), measurements made in the afternoon are lower (measurements at 320 nm and 340 nm are below the detection limit). For even higher airmass values, the pattern reverses. These variations are likely caused by changes in aerosol loading throughout the day, but could also be caused by systematic instrument errors.

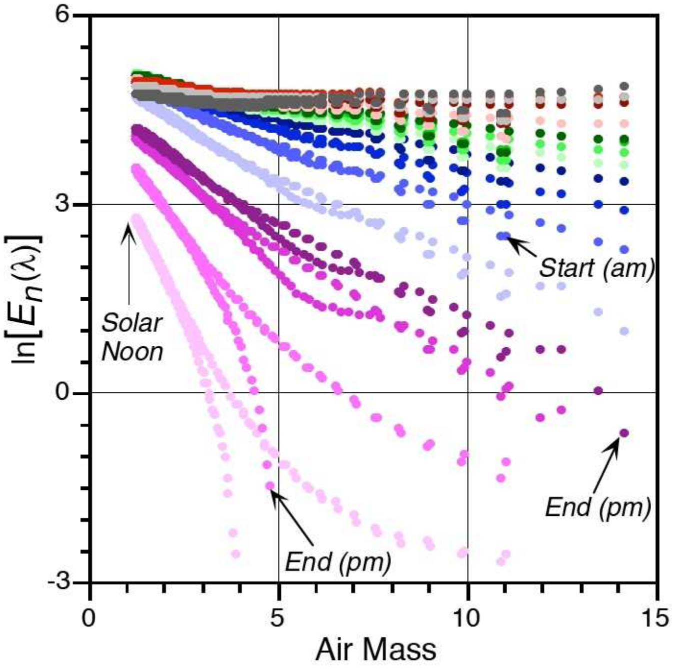

Fig. 61. A Langley plot for data measured on 7 October 2008 using the same spectral correspondence for the colored symbols that was established for Fig. 58.

5.7 Summary

Analysis of BioSHADE data has confirmed that the instrument meets its design specifications. The number of sample points recorded while the shadowband is completely blocking the Sun is sufficient for accurate retrievals of $E_a(0^+,\lambda,t_M)$. Furthermore, $E_p(0^+,\lambda,t_M)$ can be accurately determined by extrapolating measurements taken immediately before and after the times when the shadowband starts to cast a shadow of the Sun on the instrument's collector. Precise knowledge of $E_a(0^+,\lambda,t_M)$ and $E_p(0^+,\lambda,t_M)$ allows for the direct-horizontal and direct-normal irradiance to be calculated with confidence, and to construct Langley plots. The instrument size and recording speed also meet specifications.

The GPS unit provides UTC, longitude, and latitude every second. These parameters are fully integrated into the data stream of the microradiometer system and available for processing. This ensures that proper record traceability exists for sampling times and station position during data acquisition. Although not common, it is not unheard of for a research vessel to have GPS problems, so a redundant data stream can be very useful. The latter is particularly true for calibration and validation exercises wherein an important objective is to provide matchups between the *in situ* and remote sensing observations. In addition, many small vessels do not automatically record position as a function of time or have displays located where scientific work is being done, because of space and resource limitations.

The BioSHADE and BioGPS systems can be fully integrated with instrumentation based on the microradiometer architecture, wherein the two devices are operated over a single cable, linking radiometers, BioGPS, and the BioSHADE accessory. The latter ensures the accessory components and the radiometric sensors can be operated using standard cabling and deck box configurations.

Chapter 6

Scalable Hydro-optical Applications for Light-Limited Oceanography (SHALLO)

John H. Morrow
Biospherical Instruments, Inc.
San Diego, California

Stanford B. Hooker
NASA Goddard Space Flight Center
Greenbelt, Maryland

Germar Bernhard and Randall N. Lind
Biospherical Instruments, Inc.
San Diego, California

Abstract

Based on microradiometer detectors, a suite of instruments has been produced that are specifically designed to improve near-surface, near-shore, and above-water AOP measurements, particularly in light-limited environments. The hierarchical organization inherent in the use of clusters of microradiometers affords an unprecedented ease in interconnecting, modifying, or upgrading the instruments as scientific objectives or financial resources evolve. Purpose-built instruments have the potential to reduce instrument size, complexity, and costs while retaining the optimal field configuration for optical and ancillary sensors. This philosophy is made more powerful by establishing an outline of modular capabilities and a step-wise upgrade pathway for the instrument classes. Unlike legacy sensors, changing, replacing, or repairing a filter or filter-photodetector combination for a microradiometer sensor does not require disassembly of the entire electro-optics section of the instrument. The modularity of the design means it is not a significantly time-consuming and tedious procedure to upgrade a sensor. In addition, the added risk of unintended damage to associated components is minimized, as is the time required to test the subassemblies and recalibrate the sensor. The purpose of this chapter is to introduce a framework for the evolution and expansion of AOP microradiometer instruments into novel deployment opportunities, particularly in light-limited environments, while providing upgrade scenarios to match evolutions in resource allocations and science objectives.

6.1 Introduction

The development of AOP field instrumentation requires an optimization of a number of competing design elements. For commercial instruments, reducing instrument cost is always an issue, but it is not necessarily the most important design factor given that the ability for a sensor to fill multiple roles is essential in a multidisciplinary research environment. The requirement to reduce the impact of the instrument on the measurement itself drives a consistent need to reduce the size (and resulting perturbations) of the device, in particular for in-water sensors.

In contrast, and as part of next-generation planning for remote sensing platforms, there is increased interest in expanding the spectral resolution of the measurement beyond the visible domain most commonly measured by legacy instruments, into the UV and SWIR. This expansion requires the following enhancements with respect to prior designs already in use:

- Development of cosine collectors that adequately diffuse light across ever wider spectral bands (e.g., 305–1,670 nm);
- Low-noise electronics for detecting very low flux levels;
- Extreme out-of-band blocking, so small signals in the UV and SWIR can be measured accurately in the presence of much larger visible flux;
- Highly sensitive sensors with a very wide dynamic range, so there is no saturation within a greatly unbalanced spectrum or, in the case of radiance sen-

 a	• STAR sensors are the smallest sensors available (1.5 in OD). • Above- or in-water with up to 7 channels (305–1,670 nm). • Fully functional with XTRA and EPIC radiometers plus some EPIC devices (e.g., GPS). • Small size significantly reduces self-shading effect (if in water).
 b	• XTRA sensors provide wide spectral coverage (2.75 in OD). • Above- or in-water with up to 8–19 channels (305–1,670 nm). • Fully functional with STAR and *all* EPIC devices, i.e., pointing units, GPS, shadowband, and ancillary (meteorological) sensors. • Small size reduces self-shading effect (if in water).
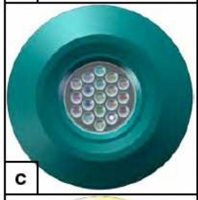 c	• OXR sensors are insulated and temperature stabilized (6 in OD). • 8–18 fixed-wavelength channels (305–1,670 nm) plus a hyperspectral spectrograph (245–785 nm or 310–1,100 nm). • Designed for *laboratory use only* (calibration transfer), but is also designed to be shipped to remote calibration facilities.
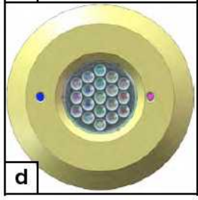 d	• EPIC sensors are insulated and temperature stabilized (6 in OD). • Above water 8–19 fixed-wavelength channels (305–1,670 nm). • Hyperspectral spectrograph (same as OXR) and video camera. • 7-position filter wheel permits hyperspectral polarimetry, Sun viewing, plus improved dark currents and stray-light correction.

Fig. 62. The four different microradiometer instrument classes as represented by a radiance instrument. The aperture ends are drawn to scale, but the colors are arbitrary.

sors viewing the surface of the water, no saturation while measuring sun glint; and

- Small sensor diameters to facilitate their use in a more diverse set of applications (e.g., robotic systems) and to minimize systematic errors (e.g., those caused by self-shading).

Temporal and thermal stability are important design elements that control not only data acquisition electronics, but material selection, component location, and conformal coating. Lastly, an outstanding instrument design will not acquire the best data if a deployment protocol that focuses on both the environment encountered in the field, and the data products that will be produced, is not rigorously applied in every campaign.

6.2 Classes

To address the objectives outlined above, four instrument classes have been established. A common feature of the classes is they all have state-of-the-art performance, because they are all based on microradiometer technology (Chap. 3). The four classes are as follows: a) Standardized Technologies for Applied Radiometry (STAR), b) Expandable Technologies for Radiometric Applications (XTRA), c) OSPREy Transfer Radiometer (OXR), and d) Enhanced Performance Instrument Class (EPIC). Figure 62 presents the four classes and summarizes their design features, which are presented in more detail below (Sect. 6.3).

Instruments within each class are available with radiance or irradiance front-end optics and each class is optimized for a specific measurement environment. Instruments within every class can be custom configured to meet the requirements for the measurement task to be performed. Several instruments can be networked together in a straightforward manner, thereby offering very flexible deployment options. Data from all instruments and ancillary sensors (e.g., pressure, temperature, shadowband, and GPS) are generally controlled by a single deck box and computer, resulting in a single, time-synchronized data stream.

6.3 Design

STAR radiometers are the smallest sensors available (1.5 in OD) and are ideally suited for applications where self-shading tends to degrade data quality or where small lightweight sensors are needed. Examples include in-water profiling of radiance and irradiance in shallow, optically complex waters or above-water measurements from an unmanned aerial vehicle (UAV). STAR sensors feature seven channels with user-selectable wavelengths, ranging from 305–1,640 nm.

XTRA radiometers provide a wide spectral coverage with up to 19 fixed-wavelength channels, which are selectable from the wavelength range of 305–1,640 nm. To accommodate the additional number of channels, the OD is 2.75 in, which is still small enough to limit self-shading effects in many water types to an acceptable level of correction. XTRA sensors are anticipated to be the *work horses* for most field campaigns and are compatible with STAR and all EPIC devices, including pointing units, GPS, shadowband accessories, and meteorological sensors.

OXR radiometers are specifically designed for high-accuracy transfers of radiometric scales between standards of spectral irradiance, such as 1,000 W tungsten-halogen lamps used by the National Institute of Standards and Technology (NIST) or other national and commercial laboratories. In addition to 8–18 fixed wavelength channels, these radiometers feature a hyperspectral spectrograph with a wavelength range of either 345–785 nm or 310–1,100 nm. The microradiometer data are used to keep the spectrograph calibrated, so the hyperspectral data can be used to accurately establish measurements between the fixed channels or at other bandwidths. The instruments are temperature stabilized and designed for laboratory use. For example, they are black anodized for minimal reflectivity, with the goal to reduce stray light in the laboratory. The OXR design is rugged enough for shipping to remote calibration facilities without the risk of affecting instrument sensitivity.

EPIC radiometers have a similar design as the OXR, but are optimized for outdoor (above-water) deployment. Like the OXR, they are temperature controlled, and feature 8–19 microradiometer channels and a spectrograph. In addition, radiance units have a filter-wheel assembly, placed in front of the optical fiber of the spectrograph. Although customized filter sets are possible, the seven-position filter wheel is typically equipped with the following: a) an opaque filter for accurate dark current measurements; b) a cut-on filter used for stray light correction; c) neutral density filters to expand the dynamic range of the spectrograph, and d) three polarization filters to determine the polarization state of both the sky and radiation emanating from a water surface.

EPIC radiometers will not saturate when pointed directly at the Sun (unless a customized filter set does not permit it), but are sensitive enough to measure low light levels. Examples include measurements of irradiance in the UV-B domain at low Sun angles, water-leaving radiance in the near infrared, and measurements of direct moon light. Pointing devices and motorized shadowbands are available as accessories for EPIC instruments. With these fully-integrated devices, the units can be used for Sun photometry or applications associated with SeaPRISM sensors (Hooker et al. 2000b and Zibordi et al. 2006). These applications allow, for example, the determination of aerosol optical depth as a function of wavelength and water-leaving radiance.

A video camera is integrated into EPIC radiance instruments and is used in lieu of a quadrant detector to point the system accurately at the center of the Sun. The camera can further provide a picture of the radiance field-of-view, so the presence of clouds across the solar disk or floating debris on the sea surface can be properly detected. Picture recognition algorithms, which are integral to the system control software, are used to flag data accordingly. When equipped with a shadowband, EPIC irradiance radiometers can alternatingly measure diffuse and global irradiance, from which the direct solar irradiance is determined.

6.4 Operation

The expandability of these instrument systems is unprecedented, because microradiometers are the modular building blocks for the sensors. In comparison to sensor systems produced in the not-too-distant past, it is significantly easier to make changes to microradiometer instruments as scientific objectives and financial resources evolve. This philosophy is made more powerful by establishing a scale of modular capabilities for the instrument classes. In the case of the STAR and XTRA sensors, five system configurations are envisioned (Fig. 63).

The simplest—or basic—system uses the minimum number of sensors and manual pointing to provide a low-cost starting point for above-water radiometry. The addition of a second sensor provides redundancy and simultaneous sampling, which yields enhanced quality assurance (QA) and data products. Automated pointing from the EPIC pan-tilt unit adds unattended sampling scenarios, which when combined with ancillary sensors like the shadowband, yield a variety of new data products. As the multiple sensor system is made more complete, redundancy minimizes risk and sampling scenarios, using synchronous and asynchronous protocols, further enhances data products and QA. Spectral diversity also can be optimized by using different spectral configurations in the multiple sensor systems, while remembering that common wavelengths will permit redundancy for the most important wavelengths and provide better QA opportunities.

The culmination of autonomous control is the inclusion of additional sensors, so the automated functions can be used safely on a moving platform, in this case a research vessel. The extra sensors also allow for improved QA, which results in better data products. A bow mounting system provides an easy mechanism to quickly remove the sensor suite in the event of severe weather (so it cannot be damaged), as well as the capability for quick and accurate reinstallation. Additional mounting options for tall (but accessible) superstructures or telescoping masts provide alternative solutions for measurements that are not contaminated by the presence of the sampling platform.

6.5 Testing and Advancements

The principal testing of the microradiometer design elements are presented in Chap. 3. The first complete system

	***Basic System*** • 7 or 8–19 Channels • One radiance sensor and one solar reference • Manual or fixed pointing	***Measurements, Data Products, and Mission Advantages*** • STAR (7 bands) or XTRA (8–19 bands) sensors (305–1,670nm) • Direct sea, sky, and reflectance plaque radiance measurements (the latter permit enhanced QA opportunity) • Tilt sensor in solar reference (GPS and shadowband optional)
	***Simultaneous System*** • One irradiance and two radiance sensors • Shadowband optional • Manual or fixed pointing	***All of the Above, and in Addition:*** • Sea and sky simultaneous sampling improves data products • GPS recommended for moving platforms (shadowband optional) • Some redundancy (radiance sensor loss permits *basic* sampling) • Enhanced QA and data products from synchronous sampling
	***Automated System*** • Synchronous and asynchronous sampling • Fixed platform (e.g., offshore tower) mounting	***All of the Above, and in Addition:*** • Unattended sampling scenarios (night darks), ancillary sensors recommended (hazards), and multiple protocols (viewing angles) • Shadowband recommended (improved cloud detection) • *Stowing* of radiance sensors significantly minimizes fouling
	***Multiple System*** • Up to 38 channels of radiance and irradiance • Fixed platform mounting • Permits full redundancy	***All of the Above, and in Addition:*** • Redundancy minimizes risk (data loss from sensor malfunction) or spectral diversity enhances data products • Maximum synchronous and asynchronous sampling scenarios • Ancillary sensors for detecting hazards (e.g., high wind and rain)
	***Moving Platform System*** • Designed for mostly unattended operations • Ancillary sensor package for hazards detection	***All of the first three Systems, and in Addition:*** • Additional detection scenarios for hazards (e.g., sea state) • Enhanced QA and QC functions (digital compass in GPS) • Bow mounting system permits easy removal (as well as, quick and accurate reinstallation) of sensors to prepare for severe weather

Fig. 63. Configuration examples of STAR and XTRA sensors showing the progression in capability and sophistication from a basic system to a moving platform system. The gold coloring denotes fully-integrated, automated components.

built from microradiometers was C-OPS, and Chap. 4 provides significant information regarding the performance of this new in-water profiling system. The capabilities of the shadowband and GPS accessories are presented in Chap. 5. Although the solar reference part of C-OPS represents an above-water capability, it does not include any radiance measurements.

The first microradiometer radiance sensor was developed as part of the OSPREy activity, and the first prototype radiance sensor was an OXR. The primary objective of the OSPREy project is to establish an above-water radiometer system as a lower-cost alternative to in-water buoys for the collection of sea-truth observations. The OSPREy system can also be used close to shore and ideally complements in-water AOP instruments, such as C-OPS (Fig. 3). Introductory information regarding OSPREy is provided in Sect. 1.1.2, and complete details are provided by Hooker et al. (2010), so only additional abbreviated summary information is provided here.

Building on the modular approach inspired by microradiometers, the OSPREy system uses temperature-controlled EPIC instruments equipped with radiance front ends that are installed on automated pointing devices (pan-tilt units) to measure the radiance emanating from the sea surface, as well as the Sun and sky. These systems are complemented by other EPIC irradiance instruments, which are outfitted with computer-controlled shadowbands to measure global and diffuse irradiance. Data collected by these instruments supports calculations of a large number of oceanic and atmospheric data products such as water-leaving radiance, aerosol optical depth, and the ratio of direct-to-global irradiance. Data collected in the NIR are particularly useful for interpreting the radiative environment in turbid coastal waters.

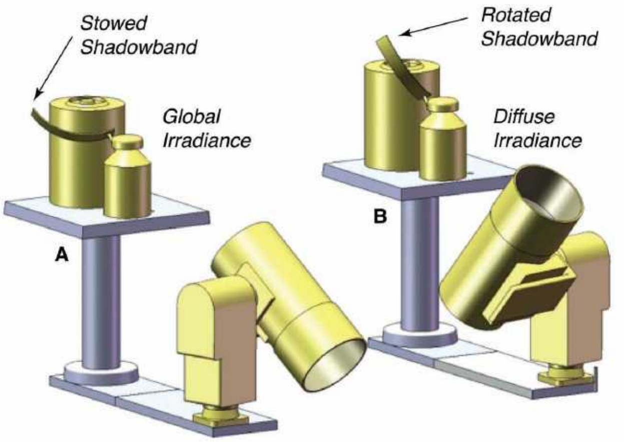

Fig. 64. The OSPREy system concept showing the two dyads of sensors (denoted A and B), which each contain one irradiance sensor (with shadow band attachments) and one radiance sensor. The pedestal mounting is for illustrative purposes, as are the pointing angles and shadowband positions.

A high level of redundancy is an important part of the OSPREy concept. Typically, a system is based on two duplicate radiometer sets, called *dyads* (Fig. 64 and also

 a	***Basic System*** • 7 or 8–19 Channels • Hydrobaric buoyancy control • Two-axis trim adjustment	***Measurements, Data Products, and Mission Advantages*** • Star (7 channels) or XTRA (8–19 channels) from 305–875 nm • In-water downward or upward irradiance and upwelled radiance • Two-axis tilt sensor in solar reference • Derivation of standard suite of ocean color data products
 b	***Extended System*** • BioSHADE shadowband with BioGPS accessory • Synchronous or asynchronous sampling	***All of the Above, and in Addition:*** • Extended atmospheric characterization (direct and diffuse solar irradiances can be computed) • Improved self-shading correction • Time and position of all sampling locations
 c	***Bidirectional System*** • Upward and downward irradiance sensors • Redundant derivation of standard data products	***All of the Above, and in Addition:*** • Direct measurement of the *Q*-factor for bidirectional effects • Enhanced data products from reflectance measurements • Improved data corrections plus more extensive QA and QC from alternative data products
 d	***Automated System*** • Automated and adaptive buoyancy control • Fail-safe *automatic return* to surface capability	***All of the Above, and in Addition:*** • Remote trimming of ascent and descent sampling options • Automated buoyancy control also permits enhanced one-person operation for manual deployment scenarios • Multiple buoyancy control options for fine-scale trim adjustment
 e	***Moving Platform System*** • Designed for unattended or attended operations • Research vessel or buoy sampling options	***All of the Above, and in Addition:*** • Embedded microcomputer deck box controller • Optional remote telemetry for onsite programming and enhanced QA and QC functions • Data collection scenarios using temporal schedules and events

Fig. 65. Configuration examples of STAR or XTRA sensors for in-water profiling observations showing the progression in capability and sophistication from a basic system to a moving platform system (a–e, respectively).

discernible in Fig. 3), which can be operated synchronously and asynchronously to enhance data quality and minimize data gaps. Note that the dyad concept is shown in Fig. 63d and represents an example of the upgrade pathways resident with all microradiometer instrument systems. All measurements are traceable to the irradiance scale maintained by NIST via an OXR and a portable light source for monitoring instrument calibration in the field at regular (e.g., monthly) intervals. Because the OSPREy system is installed above water, it is less affected by biofouling than a permanently installed in-water system.

OSPREy systems are modular and can be configured to meet different measurement tasks and funding constraints. The highest quality implementation of an OSPREy system uses sensor *triads*, wherein two irradiance sensors are used to ensure the highest quality cosine response across the full spectral range of 305–1,640 nm. The triad configuration will be deployed in a multidisciplinary role for satellite calibration and validation activities. The operational (dyad) system optimizes radiance capabilities with redundant synchronous or asynchronous capabilities. In addition to all of the standard system features, the maximum (triad) system adds a wider spectral coverage and maximum number of data products and redundancies.

The configuration options associated with OSPREy systems also make them useful for applications beyond AOP measurements. For example, a single radiance radiometer mounted on a pointing device can replace a SeaPRISM system and will provide significantly more spectral information, additional new data products, and higher quality data.

6.6 Future Designs

Originally envisioned for autonomous deployment on moorings and drifting buoy systems, the Compact Environmental Radiometer Buoyancy Enhancements for Rate-adjustable Underwater Sampling (CERBERUS) profiler is a three-sensor (E_d, E_u, and L_u) modification to the hydrobaric free-fall backplane currently in use with the SuBOPS and C-OPS instruments. It consists of a buoyant plastic backplane equipped with rigid foam flotation elements separating three 19-channel microradiometer sensors (Fig. 48). In addition to the innovations characteristic of the standard free-fall system (hydrobaric air bladders, adjustable flotation, plus pitch and roll control), CERBERUS features an automated bladder buoyancy system (rated to 25 m) that controls the rate of descent or ascent. Similar to the microradiometer optical instruments, the buoyancy system is controlled by an embedded microprocessor located in the deck box controller.

The modularity first established for above-water systems is also present for in-water instrumentation for which five configurations are envisioned (Fig. 65). The simplest—or basic—system uses a minimum number of XTRA sensors to provide a low-cost starting point for deriving the standard suite of ocean color data products. The addition of a BioSHADE and BioGPS provides atmospheric data products, improved self-shading correction, plus time and position of all sampling locations. The use of the three-sensor (CERBERUS) backplane permits the direct measurement of the Q-factor, enhanced data products, and improved QA and QC. Remote trimming of ascent and descent sampling options is achieved by adding an automated and adaptive buoyancy control module. The latter also permits enhanced one-person operation and a fail-safe automatic return to the surface capability, if the sea cable is severed. Although the backplane is automatically brought to the surface, recovery is not guaranteed, because it must still be located. Nonetheless, this is a far more desirable situation than having all the in-water components sink to the bottom (if the water depth is deep enough, this could lead to implosion of the sensor cylinders).

The culmination of autonomous control is to tether the in-water backplane to a moving platform, for example, a buoy. This system is designed for unattended or attended operations, which are controlled by an embedded microcomputer deck box controller. Optional remote telemetry can be used for onsite programming and enhanced QA and QC functions. The data collection scenarios are based on temporal schedules or specific events detected during normal operations.

6.7 Summary

Four radiometric instrument classes (STAR, XTRA, OXR, and EPIC) have recently been developed and introduced to the market to measure AOPs using both above- and in-water techniques. Each class is optimized for specific measurement tasks with an unprecedented degree of affordable expandability. STAR and XTRA sensors have a small diameter to minimize self-shading effects for in-water deployments and to fit them into novel platforms (e.g., UAVs). Temperature-stabilized OXR and EPIC radiometers excel in terms of measurement accuracy, spectral resolution, and built-in quality-control features. Instruments from all four classes can be networked together, resulting in very flexible deployment configurations. For example, above- and in-water sensors plus additional ancillary sensors, pointing devices, and shadowbands can be combined to support multidisciplinary missions such as satellite calibration and validation exercises, coastal monitoring, or UAV overflights.

Chapter 7

The Telescoping Mount for Advanced Solar Technologies (T-MAST)

Stanford B. Hooker
NASA Goddard Space Flight Center
Greenbelt, Maryland

Abstract

The solar reference data collected with an *in situ* AOP observation must be at the highest point possible on the measurement platform and free from obstructions and reflection sources. Although this is easy to state, it is not always a straightforward operation to implement. On many research vessels, the highest spaces are usually already occupied with the ship's equipment and such spaces are frequently inaccessible at sea (because of safety concerns). Consequently, AOP observations are frequently made with the solar reference located in a less than ideal location. A quantification of the consequences of improperly siting the solar reference are presented along with field evaluations of a new Telescoping Mount for Advanced Solar Technologies (T-MAST). Field trials show T-MAST is an excellent solution for this problem while providing access to the sensor(s) for cleaning, servicing, and dark current measurements.

7.1 Introduction

Whether made using above- or in-water light sensors, the most significant problem with making AOP measurements is minimizing the perturbations from the sampling platform the light sensors are deployed on or from. In the case of large platforms, the reflections from the structure above and below the water line brighten the ambient light field, whereas the shadow cast by the platform darkens it. The latter affects instruments that are deployed directly into the shadow, but also those in near proximity to it, because photons that would normally be scattered into the adjacent unshaded waters have been blocked by the structure causing the shadow. In all cases, corrections can be produced, but they require significant modeling efforts involving a large dynamic range in solar illumination, sky conditions, and viewing geometries, which is not practical unless a platform is used for extensive periods of time. The simplest expedient, therefore, is simply to avoid the perturbation areas by sampling outside them.

In the case of the sampling platform being a research vessel, the in-water problem is easily solved by floating the sampling system far away from the ship and collecting data as the profiling package falls freely through the water column (Fig. 66). Currently, there is no reliable mechanism for floating an above-water system away from a ship, so the measurements are usually made on the bow of the vessel, which is a point reliably far away from the superstructure with good fields of view of the water. In both cases, the solar reference measurement is made at the highest point possible free from obstructions and reflection sources. If properly implemented, this avoids the platform perturbations, but it does not deal with all the perturbations. The data collected by the free-fall profiler is also subjected to self-shading, the correction for which is based on the in-water properties, the size of the sensors, and the above-water solar illumination. Indeed, the absence of a self-shading problem with the above-water approach is one advantage for this type of measurement.

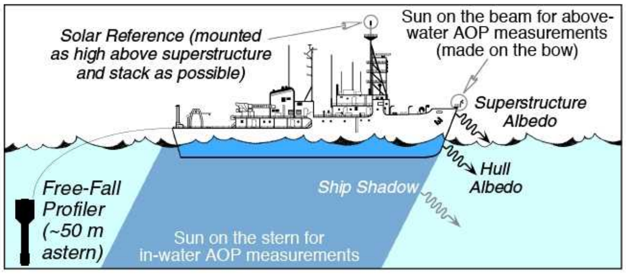

Fig. 66. A schematic representation of the platform perturbations associated with a ship and deployment locations for AOP measurements.

How far a free-fall profiler needs to be deployed away from a ship is a function of not only avoiding the light field perturbation, but also of incorporating the influence of the ambient currents, which can carry the instrumentation back into the perturbation field. A sensible compromise is to use a distance of approximately 50 m for a large ship and about 30 m for a smaller vessel. Kite-shaped profilers tend to *pop upwards* when they are hauled in, so the

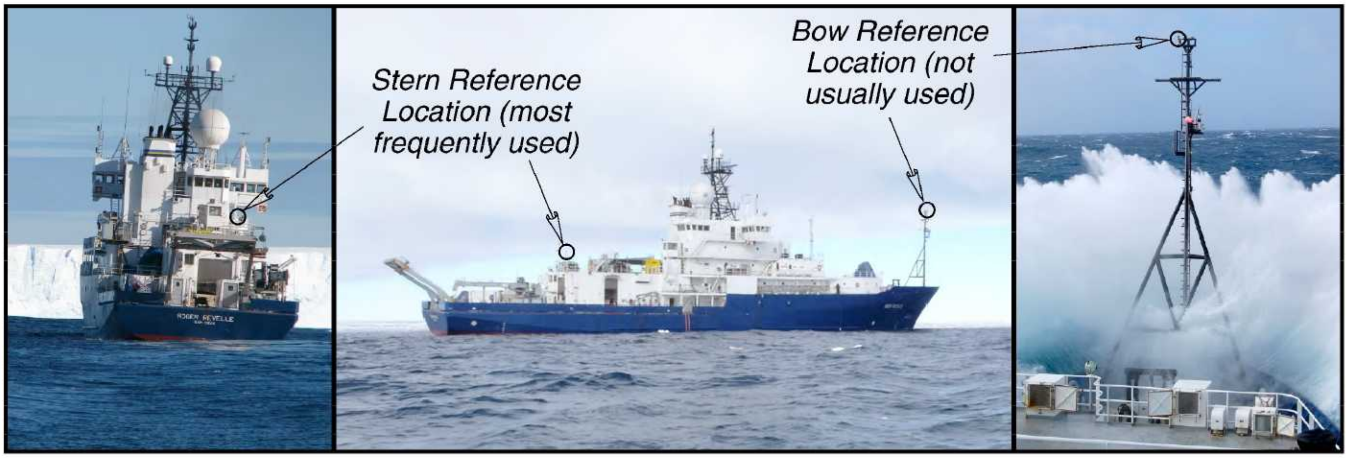

Fig. 67. Stern (left), side (middle) and bow (right) views of the R/V *Roger Revelle* showing a typical location for a solar reference towards the stern and the preferred (but more difficult) location on the bow. Although not as high as the tallest mast on the ship, the latter is substantially above and far away from the most substantial part of the superstructure, and provides significant shelter for the reference even in high sea states.

relative position of the profiler when it returns to the surface after being retrieved usually gives a good indication of local current effects. If the profiler returns not too far from where it was released, the distance from the ship need not be adjusted; if the profiler returns much closer to the ship, then a farther release distance is likely appropriate.

Very large, so-called *ocean-class*, vessels are needed for many types of oceanographic research. Arctic field campaigns, for example, require large icebreakers. A significant difficulty with icebreakers is the oversized box-shaped superstructure that is placed forward of the typical location in ocean-class research vessels. It is very difficult to measure the solar irradiance—which is a requirement for AOP measurements—on large vessels, because the light sensor needs to be far away from the light-field perturbations caused by the associated superstructure and the contamination caused by the ship's exhaust stack. Usually, this means the solar reference needs to be mounted on the highest point of the ship. Unfortunately, on many research vessels, the highest spaces are usually already occupied with the ship's equipment and such spaces are frequently inaccessible at sea (because of safety concerns).

The CVO participated in CLIVAR I6S to not only fill in the current undersampling of high latitudes, but also to understand what problems might be degrading AOP data and, hopefully, provide solutions. Although the R/V *Roger Revelle* provides many advantages for oceanic sampling, it is not very attractive for optical measurements: the highest point on top of the main mast is not readily available to scientists, and the bow mast cannot be accessed at sea. Consequently, a solar reference is usually mounted in a less than ideal location (Fig. 67).

The importance of properly siting a solar reference is quantified by comparing the bow and stern references on CLIVAR I6S. The bow sensor is assumed to provide the best data (i.e., the closest to truth), because it is mounted at the highest elevation and the farthest from superstructure perturbations, so the RPD (5) is computed as

$$\psi = 100\,\frac{E_d^S(0^+,\lambda) - E_d^B(0^+,\lambda)}{E_d^B(0^+,\lambda)}, \qquad (14)$$

where E_d^B and E_d^S are the global solar irradiances measured by the bow and stern sensors, respectively.

Figure 68 presents the RPD between the bow and stern solar references. If properly sited, two solar references should agree to within the calibration uncertainty (about 2.5%). The stern sensor exceeds this threshold about 49% of the time and has only a few examples wherein all the data agree with the bow sensor to within 2.5%. In many instances, the differences are quite large, worse than ±15%.

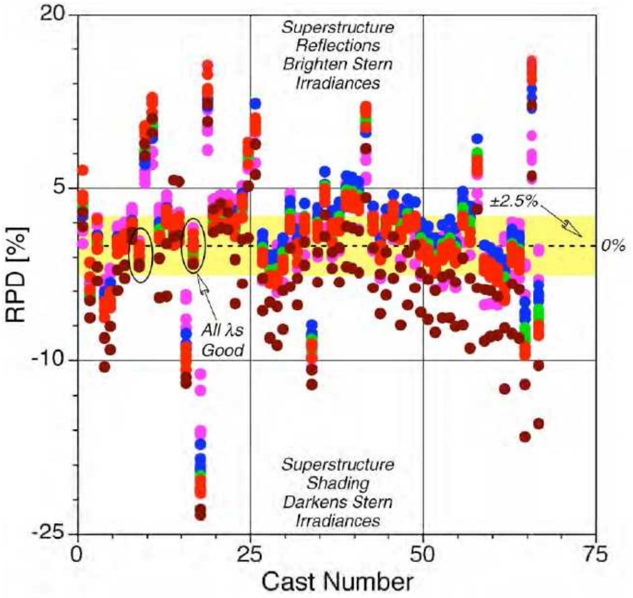

Fig. 68. The RPD between the bow and stern solar references on the R/V *Roger Revelle* (the former is the reference in the RPD calculations).

The most troubling aspect of the Fig. 68 results, however, is the introduction of a persistent bias as the ship steams farther towards the South Pole and the recurring overcast conditions lead to a steady worsening in negative RPD values. The occasional sunny stations show up as large positive excursions. This type of significant bias can have a seriously detrimental effect on data products that use the solar reference data for normalization, e.g., $R_{\mathrm{rs}}(\lambda)$ or $\left[L_W(\lambda)\right]_{\mathrm{N}}$.

7.2 Description

For ships that do not have or permit access to high superstructure locations free of significant perturbations, the only solution for the data bias problem is to either a) use contaminated data, or b) install a device that will elevate the solar sensor to a height were contamination is not possible. The latter is a potentially difficult requirement on a large vessel, because of the height of the superstructure. There are also the difficulties of wind loading, ice loading, ship motion, and the corrosive environment of conditions at sea. If a device is going to be practical, it needs to be easy to install and easy to take down—especially if foul weather is forecast.

The solution for the data bias problem presented here was to have a telescoping mast currently being used by the US military (Fig. 69) and have it modified for use on a ship. The masts are made by Floatograph Technologies (Silver Spring, Maryland), and are available in a wide variety of sizes. The masts are also offered in two different classes of ruggedness: heavy duty (steel) and light duty (aluminum). Installations to-date include 50 ft and 60 ft steel masts, and a 25 ft aluminum mast. The 50 ft and 25 ft masts were used on the Canadian Coast Guard Ship (CCGS) *Amundsen*, and the 60 ft and 25 ft masts were used on the United States Coast Guard Cutter (USCGC) *Healy*.

Fig. 69. A telescoping mast, with surveillance equipment on top, is mounted to the bumper of a humvee.

The installation of the telescoping masts on the CCGS *Amundsen* took place in 2009 and was in cooperation with the *Laboratoire d'Océanographie de Villefranche* (LOV) in France and the University of Laval in Canada as part of the Malina† field campaign to the Canadian waters of the Beaufort Sea. The installations on the USCGC *Healy* took place in 2010 as part of the Impacts of Climate on Ecosystems and Chemistry of the Arctic Pacific Environment (ICESCAPE‡) expedition to the U.S. waters of the Chukchi Sea.

For both the Malina and ICESCAPE campaigns, the EM25 telescoping mast was installed on a smaller vessel that was launched from the ice breaker (Fig. 70). The small boats deployed from the CCGS *Amundsen* and USCGC *Healy* were rather similar, and both could have the bow lowered for immediate access to the sea. The latter was useful for deploying free-fall optical sensors and was critical for finer-scale sampling, because the icebreakers and the large sampling systems deployed from them significantly mixes the upper portion of the water column to a depth of many meters. The small boat, in comparison, was allowed to drift into the areas to be sampled and minimally perturbed the near-surface layer.

Fig. 70. The EM25 telescoping mast extended on the small boat (port side, stern) launched from the CCGS *Amundsen* during C-OPS deployment operations. Note the red cable extending from the port bow and the white streak (top right corner) from the cable being hauled in.

Although a simpler mast arrangement could have been used with the small boats, the deployment and recovery scenarios for the smaller vessels on both icebreakers required a telescoping design to ensure the collapsed height

---

† Information about the Malina field campaign to the Canadian waters in the Beaufort Sea is available from the following Web site: `http://www.obs-vlfr.fr/Malina/`.

‡ Information about the ICESCAPE field campaign in 2010 to the U.S. waters in the Chukchi Sea is available from the following Web site: `http://www.espo.nasa.gov/icescape/`.

was below the height of the wheelhouse of the small boats being launched.

7.3 Design

The masts described here are models FM50, FM60, and EM25. The former two are heavy-duty steel masts and the latter is a light-duty aluminum mast. The FM masts are rated for 50 lb *payloads* on top of the mast, while the EM mast is rated for a 25 lb payload. All of the masts can be used in winds up to 60 mph and are equipped with *guy lines* to stabilize the upper parts of the mast against bending (Fig. 71). For the deployments described here, the guy lines were only used with the large masts, because the small masts were only extended for the short periods of time associated with the small boat operations.

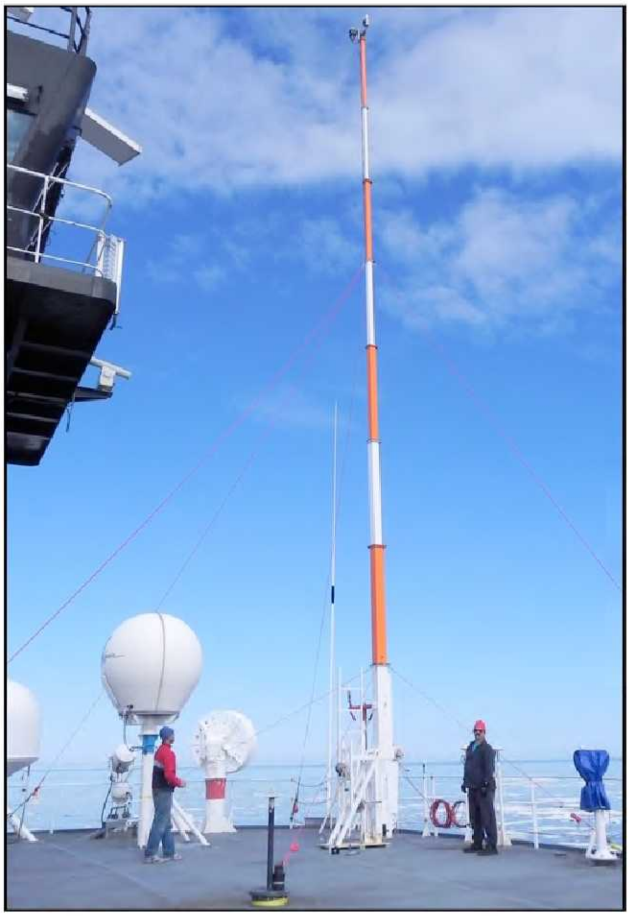

Fig. 71. The FM60 telescoping mast mounted on top of the USCGC *Healy* with Kevlar guy lines attached.

Another distinction of the large masts is they *break down* after being collapsed, so they lie horizontally and fit into a cradle. This places the entire mast at an accessible height, so the sensors mounted at the top can be cleaned or serviced. The latter also permits caps to be put on the radiometers, so dark measurements can be made. The FM60 has a partially detachable ladder as part of the base unit, so it is possible to access the payload when the mast is collapsed, without having to break it down into the horizontal resting position (Fig. 72).

Fig. 72. The FM60 telescoping mast collapsed, with the solar references being cleaned prior to the recording of dark measurements (caps on).

7.4 Modifications and Operation

Technical drawings of the FM50 and EM25 masts are presented in Figs. 73 and 74, respectively. The masts were used primarily as originally designed, but some modifications were made to accommodate their use in the marine environment:

- Some of the hardware was replaced with stainless steel (SS).
- The top stage had a 1 in national pipe tapered (NPT) coupler welded to it, so the standard 1 in NPT 316SS pipe used for mounting solar references in the field could be attached directly to the top of the mast.
- The winches were replaced with an SS marine compliant winch.
- The base of the small EM25 mast was modified, so it could be bolted against standard ship railing using mounting plates that would compress the mast against the railing.

The last item proved important for the small boat deployments during both Malina and ICESCAPE, because the

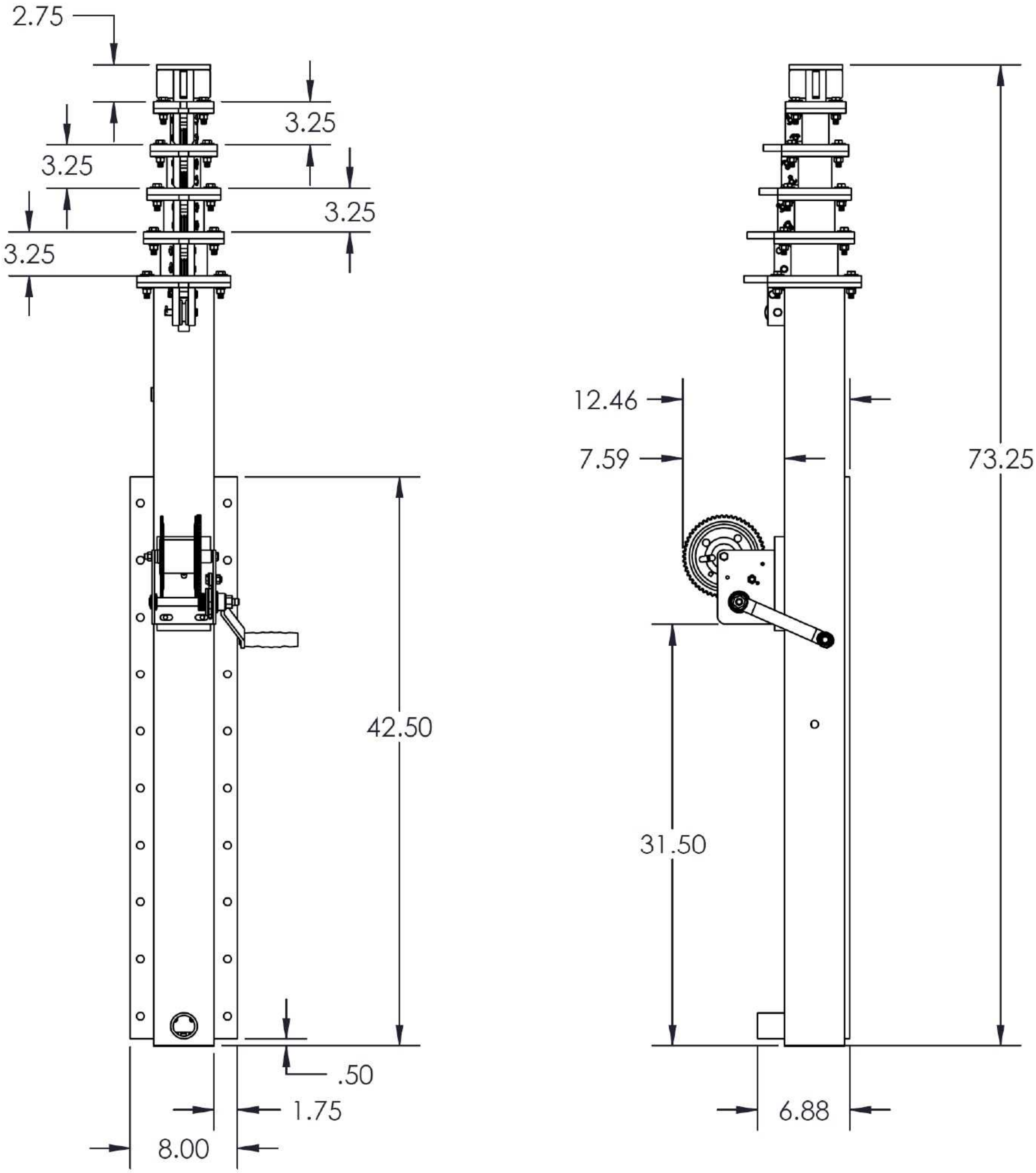

Fig. 73. A schematic of the EM25 mast showing it in the collapsed (stowed) configuration, which has an overall height of a little more than 6 ft, from two different angles. The small pipe pointing to the left and protruding from the bottom of the lowest stage associated with the telescoping mast unit (right schematic) is for pumping hot air into the mast in the event it gets frozen into place as a result of very cold and wet conditions. All dimensions are given in inches.

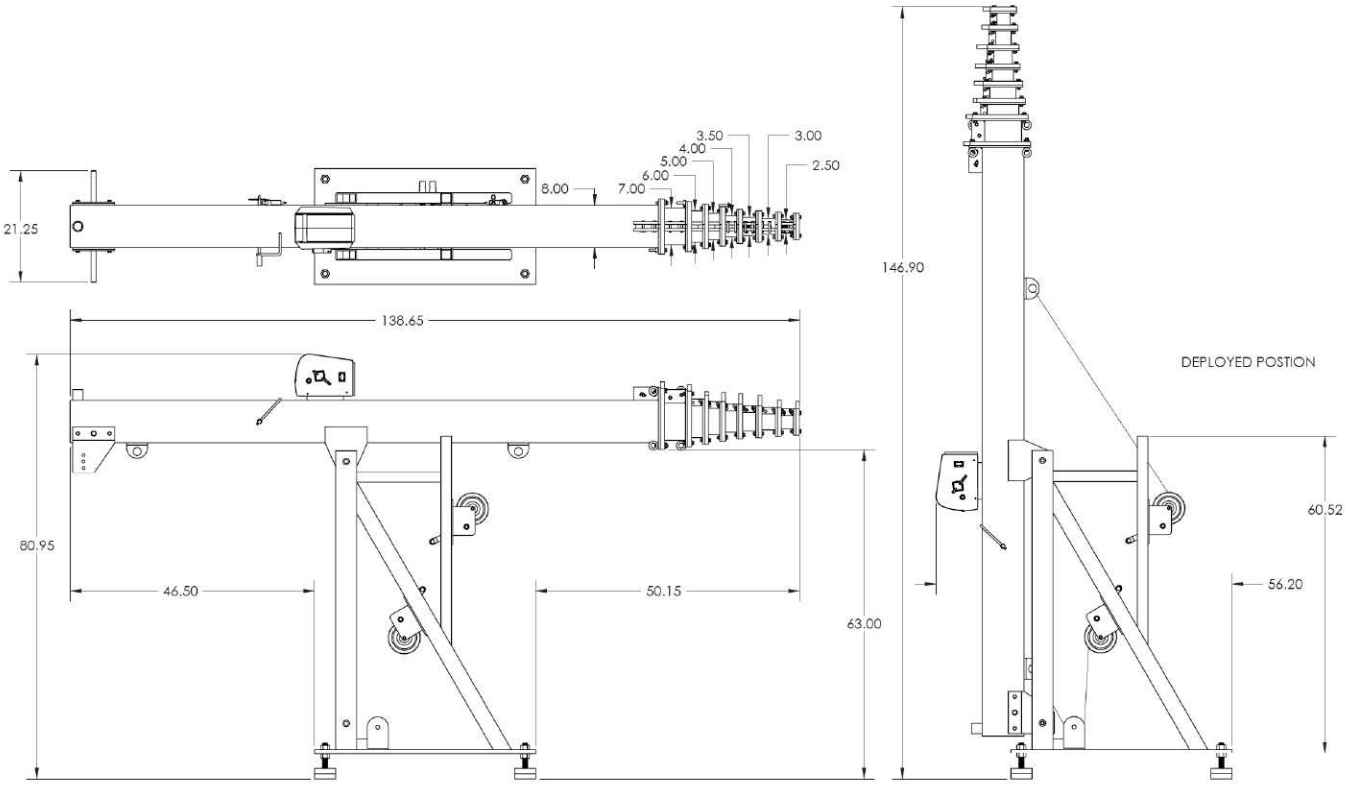

Fig. 74. A schematic of an FM50 mast (with an electronic winch for the extension and retraction functions) showing it in the stowed configuration (left) and the deployed, but collapsed, position (right). As with the EM25 mast, the small pipe pointing to the left and protruding from the bottom of the lowest stage associated with the telescoping mast unit (right schematic) is for pumping hot air into the mast in the event it gets frozen into place as a result of very cold and wet conditions. All dimensions are given in inches.

small boats involved could not be modified in any way without extensive recertification by the appropriate agencies.

The large masts have two extra hand-operated winches associated with the base unit to deploy or stow the collapsed mast into, or out of, the cradle. The primary difference between the FM50 and FM60 models is the addition of a ladder for the FM60; otherwise, the two masts are deployed and stowed in the same fashion. Once a mast is vertically oriented, it is raised and lowered with the hand-operated winch attached to the immovable lowest stage of mast. Cable guides are attached to the sides of the various telescoping stages to ensure the data telemetry cable is properly restrained.

7.5 Summary

At-sea deployments of the FM50, FM60, and EM25 masts during the Malina and ICESCAPE field campaigns established the robustness of the basic design. Throughout both campaigns, there was only one occasion when the combination of relative wind and ship headway was expected to produce winds in excess of the design limit, and the mast was lowered. There were no failures of any part of either system and all deployments resulted in the collection of excellent solar irradiance data. For the large icebreakers, vertical tilts on-station were almost always less than 2.5°, and for the small boats—which are livelier platforms—no solar irradiance data was outside the expected thresholds and all data were usable.

Chaffing of the cable from wind luffing was anticipated in the larger masts, which were left extended for significant periods of time. Split tubing with an inner diameter close to the outer diameter of the cable was used to protect the cable from rubbing against the cable guards mounted on each telescoping stage. In one instance, the tubing slipped below the cable guard and the outer braid of the cable was worn through over the course of many days of wear; the next layer of insulation was not degraded. This event showed the importance of properly applying chaffing protectors on the cabling.

Chapter 8

The Cable Hauler for Optical *In Situ* Technologies (C-HOIST)

Stanford B. Hooker
NASA Goddard Space Flight Center
Greenbelt, Maryland

John H. Morrow and Randall N. Lind
Biospherical Instruments, Inc.
San Diego, California

Abstract

Because of their large size and weight, IOP instruments are usually mounted inside a large metallic frame and require significant resources to deploy over the side of a ship, e.g., a hydraulic winch and an A-frame. In comparison, modern free-fall AOP profilers, like C-OPS, are sufficiently small in size and weight to be deployed by hand. For small boat operations, AOP instruments are easily accommodated, but IOP sensors usually are not. Most small boats are equipped with a davit for deploying small packages into the water, which, when combined with a COTS system used by the commercial fishing industry, provides a solution to the IOP instrument frame problem. The capabilities of this new deployment system, called the Cable Hauler for Optical *In Situ* Technologies (C-HOIST), is presented along with results from the field commissioning of the prototype. The significant advantages of C-HOIST are as follows: a) the power head uses 12 VDC power, which is available on most small boats; b) there is no need for hydraulics; c) the payload can be raised or lowered very slowly; and d) it can be used with standard synthetic line of any length—there is no need for an integral drum of cable.

8.1 Introduction

For most field campaigns, it is desirable to collect contemporaneous IOP measurements during, or in close temporal proximity to, AOP observations (many U.S. research vessels do not permit more than one *wire* over the side at once). For small-boat operations, like those described earlier during Malina and ICESCAPE (Sect. 7.2), the difficulty is in dealing with the large size and weight of IOP instruments in comparison to the smaller and lighter modern AOP profilers. This distinction is best summarized by the fact that IOP instruments usually require a winch and A-frame for deployment, whereas AOP instruments are routinely deployed by hand.

IOP sensors are usually mounted inside a large frame, and even if the frame is built from lightweight materials, the total weight of all the equipment needed for IOP observations can be on the order of 40 kg or more. It is not unusual for IOP systems to be so heavy—wheels are attached to the bottom of the frame to make it easier to move around on deck. Part of the reason for the large size and weight is the larger diversity in IOP variables (and, thus, instruments) than AOP light-field components, coupled with the desire to have more information about water column properties to interpret those variables, but there are also simply more components for each instrument (some, for example, require external pumps).

The net effect of the rather large and heavy instruments mounted inside a bulky frame is a requirement for some significant ship resources for safe deployment, that is, a hydraulic winch and an A-frame are needed. This is a rather difficult requirement for many small boats. The vessels launched from the icebreakers used during the Malina and ICESCAPE field campaigns, for example, did not have A-frames and they did not have hydraulic winches. Instead, they had small davits (or J-frames) and electrical winches with small-diameter stainless steel cables that were not very long in length (40 m or less).

The small-diameter cable is a concern, because it is hard to handle by hand, and many aspects of deploying or recovering a frame from a small boat require handling by the scientists or crew. A more desirable situation is to be able to use standard synthetic line with an outer diameter more in keeping with normal at-sea practices (e.g., 3/8 or 1/2 in). For a normal electromechanical winch, the larger the diameter of the line, however, the larger the size of the winch drum and, thus, the size of the winch. The amount of line that can be wound on the winch decreases as the line diameter increases, so a limiting size quickly emerges if the winch size is going to be kept small.

Adding to the difficulty of obtaining a small winch is the desire to run the winch on 12 VDC, because it is the most practical power source on small boats. There is also the problem of being able to lead the line from the winch through a pulley on the davit. In most situations for deploying with a davit, the davit is rotated to facilitate deploying and recovering the instrument package over the side of the boat. Any needed movement of the davit adds to the complexity of leading the line from the winch to the davit; therefore, a solution that easily accommodates this requirement is substantially more useful than one that does not.

8.2 Description

For small research vessels that do not have a winch and an A-frame that can lift and deploy a heavy instrument frame, but do have a davit (which is a common piece of equipment on small boats), the only practical solution is to either a) create two or more smaller subunits that can be deployed by hand, or b) bring a device that can fulfill the task. With the former, simultaneity of observations is lost, plus it is not easy to smoothly control the descent and ascent of the package by hand, except for very small instruments, so the vertical resolution of the sampling is not very uniform.

The solution adopted by the CVO was to work with BSI to modify an existing capability to solve the IOP deployment problem. The solution is based on what is called a *pot puller*, which is used by the commercial fishing industry for raising and lowering shrimp pots, or lobster and crab traps, over the side of small boats. Any of these can be quite heavy, so pot pullers with a 300 lb capacity are common.

Fishermen want to get their work done quickly, because every hour at sea is costly and reduces profitability, so pot pullers are designed to pull line in at a high velocity. Scientists making IOP measurements, on the other hand, prefer slower line speeds, so the vertical sampling resolution can be as high as possible—particularly in shallow, optically complex waters, like the coastal zone. Consequently, part of the design problem for using a commercial pot puller as the basis for C-HOIST was producing a speed control capability.

8.3 Design

The pot puller is a light-duty COTS model that is used extensively by commercial fisherman. It is equipped with a stainless steel self-grip sheave, 2.1 HP 12 VDC electric power head, 8 AWG wiring harness, 80 A circuit breaker, and has a 300 lb capacity. The gearbox assembly, which is part of the power head unit, is a *differential planetary* design that is an extremely strong and reliable unit. The gear ratio is 159:1, which means the motor turns 159 revolutions for every revolution of the sheave. The reduction unit is sealed with a life-time lubrication grease (a high pressure, EP-2 rated, lithium-based grease).

The motor assembly is O-ring sealed to prevent saltwater intrusion from spray or wash down after use at sea. Metal components are either stainless steel or powder coated for corrosion resistance. The electric motor draws 30–80 A during normal operations. If operated using a 90 A hr lead-acid (sealed) battery, approximately 25 casts lasting 6 min each can be performed before the battery needs recharging.

The sheave design eliminates the need to thread the line through complicated idler wheels and pulleys. The line is simply laid into the sheave and around the idler wheels. A light downward pull seats the line between the rubber lined sheave, which grips the line for both paying out and hauling in line. The sheave line capacity is 0.25–0.75 in. Because the line is not wound onto a drum by the power head, the line can be as long or as short as desired. There is no line length limit, and the pot puller will pull line as long as the power source is available. For the ICESCAPE campaign, the pot puller was wired into the small boat 12 VDC power system.

To provide a range of slower deployment options, the STP-2100 was mated to a deck box control unit built by BSI. The principal purpose of the deck box was to provide a speed control capability and modular power connection, that is, power from the small boat was the input to the deck box and the output was the regulated power for the pot puller. For making IOP casts, slow ascents and slow descents are equally important. In the Arctic, melt water and riverine sources can produce a thin surface layer of water with significantly different optical properties than the water below. Consequently, there was also the need to be able to sample the near surface layer(s) very slowly and then to speed up to save time.

The variable speed control of the deck box was based on a regenerative DC-to-DC drive. Most nonregenerative variable-speed DC drives control current flow to a motor in only one direction. The direction of the current flow is the same direction as motor rotation (if a motor is reversible, there are two control options). Regenerative drives can also provide motor torque in the opposite direction of motor rotation. This allows a regenerative drive to reverse motor direction without contacts or switches to control an overhauling load, and to decelerate a load faster than it would take to coast to a lower speed.

The specific regenerative drive used with C-HOIST accepts an input voltage of 10–32 VDC, provides speed regulation to within 1%, and has a maximum (peak) armature current of 120 A (250 A). The electronic control board is sufficiently compact, about $7 \times 5\,\mathrm{in}^2$, to fit inside the same small waterproof case used by BSI for their standard instrument deck boxes. Speed adjustment for paying out or hauling in line is set using a potentiometer, which is manipulated using a knob mounted on the top of the deck box.

There are three other switches on the deck box, which provide the rest of the operational controls:

- The *Hoist Enable* switch turns the power to the power head on and off.
- The *Brake* switch enables motor torque to keep the sheave stationery.
- The *Direction* switch toggles the direction the motor is turning.

The power head is connected to the davit with a swivel, so the direction for paying out or hauling in line is arbitrary and is set by the orientation of the entire assembly on the davit. Consequently, direction control simply reverses whatever is the present setting (which can be initially set or changed before line is threaded through the sheave by rotating the entire pot puller).

8.4 Operation

A picture of the prototype C-HOIST unit being used during an ICESCAPE station is shown in Fig. 75. The pot puller is hanging immediately below the end of the curved davit. The large silver disc is the self-grip sheave. To the left of the sheave is the black power head, and below the sheave are the two black idler wheels. The line attached to the IOP frame threads to the left of the idler wheel immediately below the sheave, around the sheave, and then to the right of the idler wheel below and to the left of the sheave. Not shown in the picture is the person operating the deck box to control the ascent and descent of the frame.

Fig. 75. The prototype C-HOIST unit being used during the ICESCAPE campaign from the davit on the small boat launched from the icebreaker USCGC *Healy.*

8.5 Testing

The C-HOIST power head is a COTS device for light-duty commercial crab fishing, but the motor drive and deck box are assembled by BSI. The 80 A system is rated for 300 lb dead-weight lifting. The revised cruise schedule for the ICESCAPE field campaign did not permit extensive testing or local field deployment of the prototype. In-house testing consisted of attaching the power head to an overhead steel beam and testing the main functions when powered by a 12 VDC lead-acid marine battery. This testing included retention of a large (100 kg) weight in both unpowered and dynamic hold (*brake*) states, very slow and maximum retrieve speed testing with a large (100 kg) weight, and idle testing with the deck box power turned on for hours. The temperature of the drive controller and head was monitored during all testing, and overheating was never observed under any conditions.

Field commissioning of the prototype C-HOIST during the ICESCAPE cruise consisted of more than 30 profiles of the NASA IOP frame in a variety of sea states. Unfortunately, the prototype suffered an unknown failure during the recovery of the frame on cast number 33, under light-to-moderate conditions. Disassembly of the power head aboard ship did not reveal the cause of failure and field testing was terminated.

A post-mortem conducted by BSI on the deck box confirmed it was functioning correctly and had no fault conditions. The power head was returned to the manufacturer where no mechanical or motor failure was discerned. Given the information available, the most likely candidate for the field failure is the system circuit breaker, which consisted of two 40 A thermal breakers operating in parallel. The breakers are of the type featuring automatic reset and no trip indicator. The circuit breakers have been respecified for single 80 A operation with trip indication and manual reset.

8.6 Summary

The C-HOIST device is a COTS electrical fishing winch with custom speed and direction control that can be operated from a small davit to aid deployment and retrieval of lightweight (less than 100 kg) instrument packages from almost any size boat. The system is designed to be transportable, and can be operated from any 12 VDC source with sufficiently high current capacity, including a single marine battery. The sheave on C-HOIST is designed to accept line or cable diameters up to 0.5 in, but unlike a winch, the line or cable used with C-HOIST is not spooled on the assembly, and any convenient length can be used (assuming appropriate caution is used when the remaining line on deck is reduced to a short length). The system requires two operators; one to operate the power head controls attached to the deck box, and one to control and feed the line out to the instrument package.

ACKNOWLEDGMENTS

The success of the data acquisition and data processing capabilities presented here would not have been possible without funding support from the NASA OBB Program Office. The microradiometer, aggregator, and associated systems were developed by Biospherical Instruments, Inc., with funding from the NASA SBIR Program under contract NNG06CA03C entitled "*In Situ* Radiometers: Smaller, Faster, and Scalable to Hyperspectral." The preparation of the manuscript and its final level of completeness benefitted significantly from the technical editing expertise of Elaine Firestone whose attentiveness to detail, and good cheer, are greatly appreciated.

GLOSSARY

3GμR	Three-Gain Microradiometer
A/D	Analog-to-Digital
ADC	Analog-to-Digital Converter
AERONET	Aerosol Robotic Network
AOI	Angle of Incidence
AOPs	Apparent Optical Properties
ASCII	American Standard Code for Information Interchange
AWG	American Wire Gauge
BATS	Bermuda Atlantic Time Series
BioGPS	Biospherical Global Positioning System
BioOPS	Biospherical Optical Profiling System
BioPRO	Biospherical Profiler
BioSHADE	Biospherical Shadowband Accessory for Diffuse Irradiance
BioSOPE	Biogeochemistry and Optics South Pacific Experiment
BioSORS	Biospherical Surface Ocean Reflectance System
BOUSSOLE	*Bouée pour l'acquisition de Séries Optiques à Long Terme* (literally translated from French as the "buoy for the acquisition of a long-term optical series.")
CCGS	Canadian Coast Guard Ship
CCW	Counterclockwise
CDR	Climate-quality Data Record
CERBERUS	Compact Environmental Radiometer Buoyancy Enhancements for Rate-Adjusted Underwater Sampling
C-HOIST	Cable Hauler for Optical *In Situ* Technologies
C-OPS	Compact-Optical Profiling System
COTS	Commercial Off-The-Shelf
CSTARS	Center For Southeastern Tropical Advanced Remote Sensing
CVO	Calibration and Validation Office
CW	Clockwise
DARR-94	The first SeaWiFS Data Analysis Round Robin
DARR-00	The second SeaWiFS Data Analysis Round Robin
EOS	Earth Observing System
EPIC	Enhanced Performance Instrument Class
FAFOV	Full-Angle Field of View
FEL	Not an acronym, but a lamp designator.
FPA	Filter-Photodetector Assemblies
FOV	Field of View
FWHM	Full Width at Half Maximum
GPS	Global Positioning System
GSFC	Goddard Space Flight Center
HD	Housing Diameter
ICESCAPE	Impacts of Climate on Ecosystems and Chemistry of the Arctic Pacific Environment
IOPs	Inherent Optical Properties
IR	Infrared
LCD	Liquid Crystal Display
LED	Light Emitting Diode
LoCNESS	Low-Cost NASA Environmental Sampling System
LOV	*Laboratoire d'Océanographie de Villefranche*
MERIS	Medium Resolution Imaging Spectrometer
microSAS	micro-Surface Acquisition System
microSD	Microsecure Digital (card)
microNESS	micro-NASA Environmental Sampling System
miniNESS	miniature NASA Environmental Sampling System
MMS	Multiple Microradiometer System
MOBY	Marine Optical Buoy
MODIS	Moderate Resolution Imaging Spectroradiometer
MODIS-A	Moderate Resolution Imaging Spectroradiometer-Aqua
MODIS-T	Moderate Resolution Imaging Spectroradiometer-Terra
NASA	National Aeronautics and Space Administration
NEI	Noise Equivalent Irradiance
NER	Noise Equivalent Radiance
NIR	Near Infrared
NIST	National Institute of Standards and Technology
NMEA	National Marine Electronics Association
NPT	National Pipe Tapered
OBB	Ocean Biology and Biogeochemistry
OCTS	Ocean Color and Temperature Scanner
OSPREy	Optical Sensors for Planetary Radiant Energy
OXR	OSPREy Transfer Radiometer
PAR	Photosynthetically Available Radiation
PCA	Printed Circuit Assembly
PE	Polyethylene
PGA	Programmable Gate Array
POLDER	Polarization and Directionality of the Earth's Reflectance
PP	Polypropylene
PRR	Profiling Reflectance Radiometer
psia	Pressure per Square Inch Absolute
PU	Polyurethane
PURLS	Portable Universal Radiometer Light Source
QA	Quality Assurance
RPD	Relative Percent Difference
RSMAS	Rosenstiel School of Marine and Atmospheric Science
RTD	Resistance Temperature Detector
R/V	Research Vessel

SAS	Surface Acquisition System
SBIR	Small Business Innovation Research
SeaBASS	SeaWiFS Bio-optical Archive and Storage System
SeaFALLS	SeaWiFS Free-Falling Advanced Light Level Sensors
SeaPRISM	SeaWiFS Photometer Revision for Incident-Surface Measurements
SeaSAS	SeaWiFS Surface Acquisition System
SeaWiFS	Sea-viewing Wide Field-of-view Sensor
SHALLO	Scalable Hydro-optical Applications for Light-Limited Oceanography
SIRREX	SeaWiFS Intercalibration Round-Robin Experiment
SPI	Serial Peripheral Interface
SPMR	SeaWiFS Profiling Multichannel Radiometer
SQM	SeaWiFS Quality Monitor
SS	Stainless Steel
STAR	Standardized Technologies for Applied Radimetry
SuBOPS	Submersible Biospherical Optical Profiling System
SUnSAS	SeaWiFS Underway Surface Acquisition System
SWIR	Short-Wave Infrared
SZA	Solar Zenith Angle
T-MAST	Telescoping Mount for Advanced Solar Technologies
UAV	Unmanned Aerial Vehicle
UPD	Unbiased Percent Difference
USB	Universal Serial Bus
USCGC	United States Coast Guard Cutter
UTC	Universal Time Coordinated
UV	Ultraviolet
XTRA	Expandable Technologies for Radiometric Applications

SYMBOLS

C_a	Chlorophyll a concentration.
$c_b(\lambda)$	The angular response error of the solar reference.
$C_c(\lambda)$	The spectral calibration coefficient.
$c_d(\lambda)$	The angular response error of the solar reference when measuring global irradiance.
$c_i(\lambda)$	The angular response error of the solar reference when exposed to isotropic radiation.
d	The distance between the lamp and the diffuser faceplate.
$\bar{D}(\lambda)$	The average bias or dark voltage.
$E(\lambda)$	Spectral irradiance.
$E(z,\lambda)$	Spectral irradiance at a depth z.
$E(0^+,\lambda)$	The in-air spectral irradiance just above the sea surface.
$E(0^-,\lambda)$	The in-water spectral irradiance at null depth ($z = 0^-$).
$E_0(\lambda)$	The direct-normal spectral irradiance outside the Earth's atmosphere (irradiance on a plane perpendicular to the detector–Sun direction).
$E_a(0^+,\lambda)$	The spectral irradiance at the solar reference when the centers of the solar disk, shadowband, and diffuser are aligned and direct sunlight is completely occluded (at time t_v).
$E_b(0^+,\lambda)$	The direct-horizontal spectral irradiance (irradiance on a horizontal plane from direct solar illumination).
$E_{\mathrm{cal}}(\lambda,t_i)$	The spectral calibrated irradiance.
$E_d(z,\lambda)$	The in-water spectral downward irradiance profile.
$E_d(0^+,\lambda)$	The spectral global solar irradiance (from the Sun and sky on a horizontal plane).
$E_d^B(0^+,\lambda)$	The global solar irradiance measured by a bow sensor.
$E_d^S(0^+,\lambda)$	The global solar irradiance measured by a stern sensor.
$E_i(0^+\lambda)$	The spectral diffuse (sky) irradiance (irradiance from the sky on a horizontal plane).
$E_k(0^+,\lambda)$	The hypothetical spectral irradiance at the solar reference for the segment of the sky that is shaded by the shadowband when the band is at time t_v and the shadowband is at angle v.
$E_n(0^+,\lambda)$	The direct-normal spectral irradiance (irradiance on a plane perpendicular to the detector–Sun direction).
$E_p(0^+,\lambda)$	The spectral irradiance at the solar reference at time t_v when the band is at shadowband angle v and not blocking direct sunlight.
$E'_{p_B}(0^+,\lambda)$	An extrapolated spectral irradiance (at the solar reference) at time t_M using an interval denoted B.
$E'_{p_E}(0^+,\lambda)$	An extrapolated spectral irradiance (at the solar reference) at time t_M using an interval denoted E.
E_s	A solar reference sensor.
$I_f(\lambda)$	The spectral immersion factor.
$K(\lambda)$	The spectral diffuse attenuation coefficient.
$K_d(\lambda)$	The spectral diffuse attenuation coefficient computed from $E_d(z,\lambda)$.
$L_i(0^+,\lambda)$	The spectral indirect (or sky) radiance reaching the sea surface.
$L_p(0^+,\lambda)$	The radiance of the plaque.
$L_T(0^+,\lambda)$	The (total) radiance above the sea surface.
$L_u(\lambda)$	The upwelled spectral radiance.
$L_u(z,\lambda)$	The upwelled spectral radiance at depth z.
$L_W(\lambda)$	The spectral radiance leaving the sea surface from below (the water-leaving radiance).
$\hat{L}_W(\lambda)$	The spectral water-leaving radiance derived from an above-water sampling method.
$\tilde{L}_W(\lambda)$	The spectral water-leaving radiance derived from an in-water sampling method.
$[L_W(\lambda)]_{\mathrm{N}}$	The spectral normalized water-leaving radiance.
M	The point (in time) when the centers of the Sun, shadowband, and collector are all aligned.
$m(\theta)$	The relative optical airmass.
N_P	The number of photodetectors.
$n_w(\lambda)$	The spectral refractive index of water, which is also a function of S and T.
$\mathfrak{P}$	The in-water radiometric quantities in physical units (L_u, E_d, or E_u).
P_e	The packing efficiency of microradiometers into a cylinder.
$\mathfrak{P}(z,\lambda,t_0)$	A radiometric parameter (L_u, E_d, or E_u) as it would have been recorded at all depths z at the same time t_0.
$\mathfrak{P}(0^-,\lambda)$	A subsurface radiometric quantity (L_u, E_d, or E_u) at null depth $z = 0^-$.
Q_n	Nadir-viewing measurements.

R_d	Radius of the diffuser.
R_{rs}	Remote sensing reflectance.
$\Re$	The effects of reflection and refraction.
$\Re_0$	The $\Re$ term evaluated at nadir, i.e., $\theta' = 0$
S	Salinity.
t	Time.
T	Water temperature.
t_0	A reference time (generally chosen to coincide with the start of a measurement sequence).
t_i	A specific time.
$T_s(\lambda)$	The spectral transmittance of the water surface to downward irradiance.
t_υ	The time when the shadowband is at angle υ.
$V(\lambda, t_i)$	Spectral digitized voltages (in counts).
W	Wind speed.
x	The horizontal axis (abscissa).
X	An arbitrary reference measurement.
Y	An arbitrary measurement to be investigated.
z	The vertical (depth) coordinate, where the depth is the height of water above the cosine collectors.
z_c	The critical depth.
θ	Solar zenith angle.
θ'	The above-water viewing angle (ϑ) refracted by the air–sea interface.
ϑ	The radiometer pointing angle with respect to the vertical axis, z.
ϑ'	The angle ϑ measured with respect to the zenith.
λ	Wavelength.
ρ	The surface reflectance factor.
$\tau(\lambda)$	The spectral optical depths of all scatters and absorbers in the atmosphere.
$\tau_A(\lambda)$	The aerosol optical depth.
$\tau_R(\lambda)$	The Rayleigh optical depth.
$\tau_X(\lambda)$	Other scatters and absorbers at optical depth.
ϕ	The solar azimuth angle.
φ	The perturbations (or tilts) in vertical alignment, which can change the pointing angles.
ϕ'	An angle away from the Sun (here either 90° or 135°).
ϕ^-	An angle 90° counterclockwise away from the Sun.
ϕ^+	An angle 90° clockwise away from the Sun.
ψ	The RPD value.

REFERENCES

Antoine, D., F. d'Ortenzio, S.B. Hooker, G. Bécu, B. Gentili, D. Tailliez, and A.J. Scott, 2008: Assessment of uncertainty in the ocean reflectance determined by three satellite ocean color sensors (MERIS, SeaWiFS and MODIS-A) at an offshore site in the Mediterranean Sea (BOUSSOLE project). *J. Geophys. Res.,* **113,** C07013, doi:10.1029/2007JC004472, 2008.

Austin, R.W., 1974: "The Remote Sensing of Spectral Radiance from Below the Ocean Surface." In: *Optical Aspects of Oceanography,* N.G. Jerlov and E.S. Nielsen, Eds., Academic Press, London, 317–344.

Bailey, S.W., S.B. Hooker, D. Antoine, B.A. Franz, P.J. Werdell, 2008: Sources and assumptions for the vicarious calibration of ocean color satellite observations. *Appl. Opt.,* **47,** 2,035–2,045.

Booth, C.R., T. Mestechkina, and J.H. Morrow, 1994: Errors in the reporting of solar spectral irradiance using moderate bandwidth radiometers: an experimental investigation. *SPIE Ocean Optics XII,* **2258,** 654–662.

Carder, K.L., and R.G. Steward, 1985: A remote sensing reflectance model of a red tide dinoflagellate off West Florida. *Limnol. Oceanogr.,* **30,** 286–298.

Clark, D., H.R. Gordon, K.J. Voss, Y. Ge, W. Broenkow, and C. Trees, 1997: Validation of atmospheric correction over the oceans. *J. Geophys. Res.,* **102,** 17,209–17,217.

Claustre, H., A. Sciandra, and D. Vaulot, 2008: Introduction to the special section bio-optical and biogeochemical conditions in the South East Pacific in late 2004: The BIOSOPE program. *Biogeosci.,* **5,** 679–691.

Doyle, P.J., S.B. Hooker, G. Zibordi, and D. van der Linde, 2003: Validation of an In-Water, Tower-Shading Correction Scheme. *NASA Tech. Memo. 2003–206892, Vol. 25,* S.B. Hooker and E.R. Firestone, Eds., NASA Goddard Space Flight Center, Greenbelt, Maryland, 32 pp.

Fougnie, B., R. Frouin, P. Lecomte, and P-Y. Deschamp, 1999: Reduction of skylight reflection effects in the above-water measurement of diffuse marine reflectance. *Appl. Opt.,* **38,** 3,844–3,856.

Gordon, H.R., and D.K. Clark, 1981: Clear water radiances for atmospheric correction of coastal zone color scanner imagery. *Appl. Opt.,* **20,** 4,175–4,180.

——, and K. Ding, 1992: Self-shading of in-water optical instruments. *Limnol. Oceanogr.,* **37,** 491–500.

Holben, B.N., T.F. Eck, I. Slutsker, D. Tanré, J.P. Buis, A. Setzer, E. Vermote, J.A. Reagan, Y.J. Kaufman, T. Nakajima, F. Lavenu, I. Jankowiak, and A. Smirnov, 1998: AERONET—A federated instrument network and data archive for aerosol characterization. *Remote Sens. Environ.,* **66,** 1–16.

Hooker, S.B., 2000: "Stability Monitoring of Field Radiometers Using Portable Sources." In: G.S. Fargion and J.L. Mueller, Ocean Optics Protocols for Satellite Ocean Color Sensor Validation, Revision 2. *NASA Tech. Memo. 2000–209966,* NASA Goddard Space Flight Center, Greenbelt, Maryland, 57–64.

——, 2002: "Stability Monitoring of Field Radiometers Using Portable Sources." In: Mueller, J.L., and 39 Co-authors, Ocean Optics Protocols for Satellite Ocean Color Sensor Validation, Revision 3, Volume 1, J.L. Mueller and G.S. Fargion, Eds., *NASA Tech. Memo. 2002–210004/Rev3/Vol1,* NASA Goddard Space Flight Center, Greenbelt, Maryland, 91–99.

——, and W.E. Esaias, 1993: An overview of the SeaWiFS project. *Eos, Trans., Amer. Geophys. Union,* **74,** 241–246.

——, and J. Aiken, 1998: Calibration evaluation and radiometric testing of field radiometers with the SeaWiFS Quality Monitor (SQM). *J. Atmos. Oceanic Tech.,* **15,** 995–1,007.

——, G. Zibordi, G. Lazin, and S. McLean, 1999: The SeaBOARR-98 Field Campaign. *NASA Tech. Memo. 1999–206892, Vol. 3,* S.B. Hooker and E.R. Firestone, Eds., NASA Goddard Space Flight Center, Greenbelt, Maryland, 40 pp.

——, and G. Lazin, 2000: The SeaBOARR-99 Field Campaign. *NASA Tech. Memo. 2000–206892, Vol. 8,* S.B. Hooker and E.R. Firestone, Eds., NASA Goddard Space Flight Center, 46 pp.

——, and S. Maritorena, 2000: An evaluation of oceanographic radiometers and deployment methodologies. *J. Atmos. Oceanic Technol.,* **17,** 811–830.

——, and C.R. McClain, 2000: The calibration and validation of SeaWiFS data. *Prog. Oceanogr.,* **45,** 427–465.

——, and A. Morel, 2003: Platform and environmental effects on above- and in-water determinations of water-leaving radiances. *J. Atmos. Ocean. Technol.,* **20,** 187–205.

——, and G. Zibordi, 2005: Platform perturbations in above-water radiometry. *Appl. Opt.,* **44,** 553–567.

——, H. Claustre, J. Ras, L. Van Heukelem, J-F. Berthon, C. Targa, D. van der Linde, R. Barlow, and H. Sessions, 2000a: The First SeaWiFS HPLC Analysis Round-Robin Experiment (SeaHARRE-1). *NASA Tech. Memo. 2000–206892, Vol. 14,* S.B. Hooker and E.R. Firestone, Eds., NASA Goddard Space Flight Center, Greenbelt, Maryland, 42 pp.

——, G. Zibordi, J-F. Berthon, S.W. Bailey, and C.M. Pietras, 2000b: The SeaWiFS Photometer Revision for Incident Surface Measurement (SeaPRISM) Field Commissioning. *NASA Tech. Memo. 2000–206892, Vol. 13,* S.B. Hooker and E.R. Firestone, Eds., NASA Goddard Space Flight Center, Greenbelt, Maryland, 24 pp.

——, ——, ——, D. D'Alimonte, S. Maritorena, S. McLean, and J. Sildam, 2001: Results of the Second SeaWiFS Data Analysis Round Robin, March 2000 (DARR-00). *NASA Tech. Memo. 2001–206892, Vol. 15,* S.B. Hooker and E.R. Firestone, Eds., NASA Goddard Space Flight Center, Greenbelt, Maryland, 71 pp.

——, S. McLean, J. Sherman, M. Small, G. Lazin, G. Zibordi, and J.W. Brown, 2002a: The Seventh SeaWiFS Intercalibration Round-Robin Experiment (SIRREX-7), March 1999. *NASA Tech. Memo. 2002–206892, Vol. 17,* S.B. Hooker and E.R. Firestone, Eds., NASA Goddard Space Flight Center, Greenbelt, Maryland, 69 pp.

——, G. Lazin, G. Zibordi, and S. McLean. 2002b. An evaluation of above- and in-water methods for determining water-leaving radiances. *J. Atmos. Oceanic Technol.,* **19,** 486–515.

——, G. Zibordi, J-F. Berthon, D. D'Alimonte, D. van der Linde, and J.W. Brown, 2003: Tower-Perturbation Measurements in Above-Water Radiometry. *NASA Tech. Memo. 2003–206892, Vol. 23,* S.B. Hooker and E.R. Firestone, Eds., NASA Goddard Space Flight Center, Greenbelt, Maryland, 35 pp.

——, ——, ——, and J.W. Brown, 2004: Above-water radiometry in shallow, coastal waters. *Appl. Opt.,* **43,** 4,254–4,268.

——, L. Van Heukelem, C.S. Thomas, H. Claustre, J. Ras, L. Schlüter, J. Perl, C. Trees, V. Stuart, E. Head, R. Barlow, H. Sessions, L. Clementson, J. Fishwick, C. Llewellyn, and J. Aiken, 2005: The Second SeaWiFS HPLC Analysis Round-Robin Experiment (SeaHARRE-2). *NASA Tech. Memo. 2005–212785,* NASA Goddard Space Flight Center, Greenbelt, Maryland, 112 pp.

——, ——, ——, ——, ——, ——, L. Clementson, D. Van der Linde, E. Eker-Develi, J-F. Berthon, R. Barlow, H. Sessions, J. Perl, and C. Trees, 2009: The Third SeaWiFS HPLC Analysis Round-Robin Experiment (SeaHARRE-3). *NASA Tech. Memo. 2009,* NASA Goddard Space Flight Center, Greenbelt, Maryland, 97 pp.

——, G. Bernhard, J.H. Morrow, C.R. Booth, T. Cromer, R.N. Lind, and V. Quang, 2010: Optical Sensors for Planetary Radiant Energy (OSPREy): Calibration and Validation of Current and Next-Generation NASA Missions. *NASA Tech. Memo.,* NASA Goddard Space Flight Center, Greenbelt, Maryland, (in prep.).

Johnson, B.C., S.S. Bruce, E.A. Early, J.M. Houston, T.R. O'Brian, A. Thompson, S.B. Hooker, and J.L. Mueller, 1996: The Fourth SeaWiFS Intercalibration Round-Robin Experiment (SIRREX-4), May 1995. *NASA Tech. Memo. 104566, Vol. 37,* S.B. Hooker and E.R. Firestone, Eds., NASA Goddard Space Flight Center, Greenbelt, Maryland, 65 pp.

——, F. Sakuma, J.J. Butler, S.F. Biggar, J.W. Cooper, J. Ishida, and K. Suzuki, 1997: Radiometric Measurement Comparison Using the Ocean Color Temperature Scanner (OCTS) Visible and Near Infrared Integrating Sphere. *J. Res. NIST,* **102,** 627–646.

——, P-S. Shaw, S.B. Hooker, and D. Lynch, 1998: Radiometric and engineering performance of the SeaWiFS Quality Monitor (SQM): A portable light source for field radiometers. *J. Atmos. Oceanic Tech.,* **15,** 1,008–1,022.

——, H.W. Yoon, S.S. Bruce, P-S. Shaw, A. Thompson, S.B. Hooker, R.E. Eplee, Jr., R.A. Barnes, S. Maritorena, and J.L. Mueller, 1999: The Fifth SeaWiFS Intercalibration Round-Robin Experiment (SIRREX-5), July 1996. *NASA Tech. Memo. 1999–206892, Vol. 7,* S.B. Hooker and E.R. Firestone, Eds., NASA Goddard Space Flight Center, 75 pp.

McClain, C.R., W.E. Esaias, W. Barnes, B. Guenther, D. Endres, S.B. Hooker, G. Mitchell, and R. Barnes, 1992: Calibration and Validation Plan for SeaWiFS. *NASA Tech. Memo. 104566, Vol. 3,* S.B. Hooker and E.R. Firestone, Eds., NASA Goddard Space Flight Center, Greenbelt, Maryland, 41 pp.

——, G.C. Feldman, and S.B. Hooker, 2004: An overview of the SeaWiFS project and strategies for producing a climate research quality global ocean bio-optical time series. *Deep Sea Res. II,* **51,** 5–42.

Mobley, C.D., 1999: Estimation of the remote-sensing reflectance from above-surface measurements. *Appl. Opt.,* **38,** 7,442–7,455.

Morel, A., and L. Prieur, 1977: Analysis of variations in ocean color. *Limnol. Oceanogr.,* **22,** 709–722.

——, and B. Gentili, 1996: Diffuse reflectance of oceanic waters, III. Implication of bidirectionality for the remote sensing problem. *Appl. Opt.,* **35,** 4,850–4,862.

——, and J.L. Mueller, 2002: "Normalized Water-Leaving Radiance and Remote Sensing Reflectance: Bidirectional Reflectance and Other Factors." In: J.L. Mueller and G.S. Fargion, Ocean Optics Protocols for Satellite Ocean Color Sensor Validation, Revision 3, Volume 2. *NASA Tech. Memo. 2002–210004/Rev3–Vol2,* NASA Goddard Space Flight Center, Greenbelt, Maryland, 183–210.

Morrow, J.H., M.S. Duhig, C.R. Booth, 1994: Design and evaluation of a cosine collector for a SeaWiFS-compatible marine reflectance radiometer. *SPIE Ocean Optics XII,* **2258,** 879–886.

——, M. Duhig, and C.R. Booth, 1994: Design and Evaluation of a cosine collector for a SeaWiFS-compatible Marine Reflectance Radiometer. *SPIE Ocean Optics XII,* **2258,** 879–886.

Mueller, J.L., 1993: The First SeaWiFS Intercalibration Round-Robin Experiment, SIRREX-1, July 1992. *NASA Tech. Memo. 104566, Vol. 14,* S.B. Hooker and E.R. Firestone, Eds., NASA Goddard Space Flight Center, Greenbelt, Maryland, 60 pp.

——, 1995: "Comparison of Irradiance Immersion Coefficients for Several Marine Environmental Radiometers (MERs)." In: Mueller, J.L., R.S. Fraser, S.F. Biggar, K.J. Thome, P.N. Slater, A.W. Holmes, R.A. Barnes, C.T. Weir, D.A. Siegel, D.W. Menzies, A.F. Michaels, and G. Podesta: Case Studies for SeaWiFS Calibration and Validation, Part 3. *NASA Tech. Memo. 104566, Vol. 27,* S.B. Hooker, E.R. Firestone, and J.G. Acker, Eds., NASA Goddard Space Flight Center, Greenbelt, Maryland, 46 pp.

——, 2000: "Overview of Measurement and Data Analysis Protocols" In: G.S. Fargion and J.L. Mueller, Ocean Optics Protocols for Satellite Ocean Color Sensor Validation, Revision 2. *NASA Tech. Memo. 2000–209966,* NASA Goddard Space Flight Center, Greenbelt, Maryland, 87–97.

——, 2002: "Overview of Measurement and Data Analysis Protocols." In: J.L. Mueller and G.S. Fargion, Ocean Optics Protocols for Satellite Ocean Color Sensor Validation, Revision 3, Volume 1. *NASA Tech. Memo. 2002–210004/Rev3–Vol1,* NASA Goddard Space Flight Center, Greenbelt, Maryland, 123–137.

——, 2003: "Overview of Measurement and Data Analysis Methods." In: J.L. Mueller and 17 Coauthors, Ocean Optics Protocols for Satellite Ocean Color Sensor Validation, Revision 4, Volume III: Radiometric Measurements and Data Analysis Protocols. *NASA Tech. Memo. 2003–211621/Rev4–Vol.III,* NASA Goddard Space Flight Center, Greenbelt, Maryland, 1–6.

——, and R.W. Austin, 1992: Ocean Optics Protocols for SeaWiFS Validation. *NASA Tech. Memo. 104566, Vol. 5,* S.B. Hooker and E.R. Firestone, Eds., NASA Goddard Space Flight Center, Greenbelt, Maryland, 43 pp.

——, B.C. Johnson, C.L. Cromer, J.W. Cooper, J.T. McLean, S.B. Hooker, and T.L. Westphal, 1994: The Second SeaWiFS Intercalibration Round-Robin Experiment, SIRREX-2, June 1993. *NASA Tech. Memo. 104566, Vol. 16,* S.B. Hooker and E.R. Firestone, Eds., NASA Goddard Space Flight Center, Greenbelt, Maryland, 121 pp.

——, and R.W. Austin, 1995: Ocean Optics Protocols for SeaWiFS Validation, Revision 1. *NASA Tech. Memo. 104566, Vol. 25,* S.B. Hooker, E.R. Firestone, and J.G. Acker, Eds., NASA Goddard Space Flight Center, Greenbelt, Maryland, 66 pp.

——, B.C. Johnson, C.L. Cromer, S.B. Hooker, J.T. McLean, and S.F. Biggar, 1996: The Third SeaWiFS Intercalibration Round-Robin Experiment (SIRREX-3), 19–30 September 1994. *NASA Tech. Memo. 104566, Vol. 34,* S.B. Hooker, E.R. Firestone, and J.G. Acker, Eds., NASA Goddard Space Flight Center, Greenbelt, Maryland, 78 pp.

——, and A. Morel, 2003: "Fundamental Definitions, Relationships and Conventions." In: J.L. Mueller and 4 Coauthors, Ocean Optics Protocols for Satellite Ocean Color Sensor Validation, Revision 4, Volume I: Radiometric Measurements and Data Analysis Protocols. *NASA Tech. Memo. 2003–211621/Rev4–Vol.I,* NASA Goddard Space Flight Center, Greenbelt, Maryland, 11–30.

O'Reilly, J.E., S. Maritorena, B.G. Mitchell, D.A. Siegel, K.L. Carder, S.A. Garver, M. Kahru, and C. McClain, 1998: Ocean color chlorophyll algorithms for SeaWiFS. *J. Geophys. Res.,* **103,** 24,937–24,953.

——, and 24 Coauthors, 2000: SeaWiFS Postlaunch Calibration and Validation Analyses, Part 3. *NASA Tech. Memo. 2000–206892, Vol. 11,* S.B. Hooker and E.R. Firestone, Eds., NASA Goddard Space Flight Center, 49 pp. 1,907–1,925.

Riley, T., and S. Bailey, 1998: The Sixth SeaWiFS/SIMBIOS Intercalibration Round-Robin Experiment (SIRREX-6) August–December 1997. *NASA Tech. Memo. 1998–206878,* NASA Goddard Space Flight Center, Greenbelt, Maryland, 26 pp.

Siegel, D.A., M.C. O'Brien, J.C. Sorensen, D. Konnoff, E.A. Brody, J.L. Mueller, C.O. Davis, W.J. Rhea, and S.B. Hooker, 1995: Results of the SeaWiFS Data Analysis Round-Robin (DARR), July 1994. *NASA Tech. Memo. 104566, Vol. 26,* S.B. Hooker and E.R. Firestone, Eds., NASA Goddard Space Flight Center, Greenbelt, Maryland, 58 pp.

Smith, R.C., and K.S. Baker, 1984: The analysis of ocean optical data. *Ocean Optics VII,* M. Blizard, Ed., *SPIE,* **478,** 119–126.

Toole, D.A., D.A. Siegel, D.W. Menzies, M.J. Neumann, and R.C. Smith, 2000: Remote sensing reflectance determinations in the coastal ocean environment—impact of instrumental characteristics and environmental variability. *Appl. Opt.,* **39,** 456–469.

Zibordi, G., J.P. Doyle, and S.B. Hooker, 1999: Offshore tower shading effects on in-water optical measurements. *J. Atmos. Oceanic Tech.,* **16,** 1,767–1,779.

——, D. D'Alimonte, D. van der Linde, J-F. Berthon, S.B. Hooker, J.L. Mueller, G. Lazin, and S. McLean, 2002: The Eighth SeaWiFS Intercalibration Round-Robin Experiment (SIRREX-8), September–December 2001. *NASA Tech. Memo. 2002–206892, Vol. 20,* S.B. Hooker and E.R. Firestone, Eds., NASA Goddard Space Flight Center, Greenbelt, Maryland, 39 pp.

——, F. Mélin, S.B. Hooker, D. D'Alimonte, and B. Holben, 2004: An autonomous above-water system for the validation of ocean color radiance data. *Trans. IEEE Trans. Geosci. Remote Sensing.,* **42,** 401–415.

——, B. Holben, S.B. Hooker, F. Mélin, J-F. Berthon, I. Slutsker, D. Giles, D. Vandemark, H. Feng, K. Rutledge, G. Schuster, and A. Al Mandoos, 2006: A Network for Standardized Ocean Color Validation Measurements. *Eos, Trans. Amer. Geophys. Union*, **84,** 293, 297.

REPORT DOCUMENTATION PAGE	*Form Approved* *OMB No. 0704-0188*

1. REPORT DATE *(DD-MM-YYYY)* 31-12-2010	**2. REPORT TYPE** Technical Memorandum	**3. DATES COVERED** *(From - To)*

4. TITLE AND SUBTITLE

Advances in Measuring the Apparent Optical Properties (AOPs) of Optically Complex Waters

5a. CONTRACT NUMBER

5b. GRANT NUMBER

NNX09AN94G

5c. PROGRAM ELEMENT NUMBER

6. AUTHOR(S)

John H. Morrow, Stanford B. Hooker, Charles R. Booth, Germar Bernhard, Randall N. Lind, and James W. Brown

5d. PROJECT NUMBER

5e. TASK NUMBER

5f. WORK UNIT NUMBER

7. PERFORMING ORGANIZATION NAME(S) AND ADDRESS(ES)

NASA Calibration and Validation Office (CVO)
BWtech, 1450 S. Rolling Rd., Suite 4.001
Halethorpe, MD 21227

8. PERFORMING ORGANIZATION REPORT NUMBER

9. SPONSORING/MONITORING AGENCY NAME(S) AND ADDRESS(ES)

National Aeronautics and Space Administration
Washington, DC 20546-0001

10. SPONSORING/MONITOR'S ACRONYM(S)

11. SPONSORING/MONITORING REPORT NUMBER

TM-2010-215856

12. DISTRIBUTION/AVAILABILITY STATEMENT

Unclassified-Unlimited, Subject Category: 25, 48
Report available from the NASA Center for Aerospace Information, 7115 Standard Drive, Hanover, MD 21076. (443)757-5802

13. SUPPLEMENTARY NOTES

John H. Morrow, Charles R. Booth, Germar Bernhard, and Randall N. Lind; Biospherical Instruments Inc., San Diego, CA; and James W. Brown: CSTARS University of Miami, Miami, FL

14. ABSTRACT

This report documents new technology used to measure the apparent optical properties (AOPs) of optically complex waters. The principal objective is to be prepared for the launch of next-generation ocean color satellites with the most capable commercial off-the-shelf (COTS) instrumentation. An enhanced COTS radiometer was the starting point for designing and testing the new sensors. The follow-on steps were to apply the lessons learned towards a new in-water profiler based on a kite-shaped backplane for mounting the light sensors. The next level of sophistication involved evaluating new radiometers emerging from a development activity based on so-called microradiometers. The exploitation of microradiometers resulted in an in-water profiling system, which includes a sensor networking capability to control ancillary sensors like a shadowband or global positioning system (GPS) device. A principal advantage of microradiometers is their flexibility in producing, interconnecting, and maintaining instruments. The full problem set for collecting sea-truth data—whether in coastal waters or the open ocean—involves other aspects of data collection that were improved for instruments measuring both AOPs and inherent optical properties (IOPs), if the uncertainty budget is to be minimized. New capabilities associated with deploying solar references were developed as well as a compact solution for recovering in-water instrument systems from small boats.

15. SUBJECT TERMS

SeaWiFS, apparent optical properties, AOP, light sensor, radiometer, microradiometer, solar reference, optically complex water

16. SECURITY CLASSIFICATION OF:			**17. LIMITATION OF ABSTRACT**	**18. NUMBER OF PAGES**	**19b. NAME OF RESPONSIBLE PERSON**
a. REPORT	**b. ABSTRACT**	**c. THIS PAGE**			Stanford B. Hooker
Unclassified	Unclassified	Unclassified	Unclassified	80	**19b. TELEPHONE NUMBER** ***(Include area code)*** (410) 533-6451

Standard Form 298 (Rev. 8-98)
Prescribed by ANSI Std. Z39-18